Electrohydrodynamic and Thermocapillary Instability of Thin Liquid Films

by

Hadi Nazaripoor

A thesis submitted in partial fulfillment of the requirements for the degree of

Doctor of Philosophy

Department of Mechanical Engineering
University of Alberta

Abstract

Electrically induced instability of thin liquid films is a contactless pattern transfer method, often called electrohydrodynamic (EHD) lithography, which has gained extensive attention due to its ability in creation of novel micro- and nano-sized structures. The need for powerful microprocessors and cheaper electronic memory has accelerated the research effort on finding novel, fast and inexpensive techniques for creation of nano-sized features. An electrostatic model is developed called an ionic liquid (IL) model which consider a finite diffuse electric layer with comparable thickness to the film. This overcomes the shortcoming of assuming very large and small electric diffuse layer inherent in the perfect dielectric (PD) and leaky dielectric (LD) models respectively. The process of pattern formation is then numerically simulated by solving the nonlinear thin film equation using finite difference for the spatial domain and an adaptive time step solver for time.

In single layer film, the total number of pillars formed (raised columnar structures called pillars) in $1\mu\text{m}^2$ area of the domain in IL film is almost 5 times more than similar PD film for the conditions simulated. Replacing the flat electrode with the patterned one is found to result in more compact and well-ordered structures particularly when an electrode with square block protrusions is used. Structure size in PD films is reduced by a factor of four when it is replaced with IL films which results in nano-sized features with well-ordered pattern over the domain.

In bilayer systems, an extensive numerical study is carried out to generate a map based on electric permittivity ratio of layers and the initial mean thickness of the lower layer. This map is used to predict the formation of various structures on PD-PD bilayers interface and provides a baseline for unstable IL-PD bilayers. The use of an IL layer is found to reduce the size of the structures, but results in polydispersed and disordered pillars spread over the domain. The numerical predictions follow similar trend of experimental observation in literature [1].

To improve the electrically assisted patterning process and create smaller sized features with the higher active surface area, the combined thermocapillary (TC) and EHD instability of liquid nanofilms is considered using both linear stability and nonlinear analysis. The number density of pillars formed in $1\mu\text{m}^2$ area is significantly increased compared to the EHD base-case and nano-sized pillars are created due to the TC effects. Relative interface area increases of up to 18% due to this pattern miniaturization are realized. It is also found that increase in the thermal conductivity ratio of layers changes the mechanism of pattern formation resulting in nonuniform and randomly distributed micro pillars being generated.

Keywords: Thin films, electrohydrodynamic, electrokinetic, thermocapillary, Marangoni, perfect dielectric, ionic liquids, instability, dynamics, numerical simulation, micro and nano patterning

Preface

This thesis is original work by Hadi Nazaripoor. Some parts of this research chapter 1 and 2 and 3 and 4 and 5 and 6 of this thesis have been published or presented as:

1. Hadi Nazaripoor, Charles R. Koch, and Subir Bhattacharjee. Electrical perturbations of ultrathin bilayers: Role of ionic conductive layer. Langmuir, 30(49) : 14734−14744, 2014. PMID: 25419880. (Ref. [2])

2. Hadi Nazaripoor, Charles R. Koch, Mohtada Sadrzadeh, and Subir Bhattacharjee. Electrohydrodynamic patterning of ultra-thin ionic liquid films. Soft Matter, 11:2193−2202, 2015. (Ref. [3])

3. Hadi Nazaripoor, Charles R. Koch, Mohtada Sadrzadeh, and Subir Bhattacharjee. Compact micro/nano electrohydrodynamic patterning: Using a thin conductive film and a patterned template. Soft Matter, 12:1074−1084, 2016. (Ref. [4])

4. Hadi Nazaripoor, Charles R. Koch, Mohtada Sadrzadeh, and Subir Bhattacharjee. Thermo-electrohydrodynamic patterning in nanofilms. Langmuir, 32(23):5776−5786, 2016. (Ref. [5])

5. Hadi Nazaripoor, Charles R. Koch, and Subir Bhattacharjee. Dynam-

ics of thin liquid bilayers subjected to an external electric field. In Proceedings of ASME. 46545, volume 7, pages 62−69, November 2014. DOI:10.1115/IMECE2014-37302. (Ref. [6])

6. Hadi Nazaripoor, Charles R Koch, Mohtada Sadrzadeh. Electrostatic model for electric-field-induced instabilities of thin ionic liquid films. Presented in 64th Canadian Society of Chemical Engineering Conference, 19-22 October 2014, Niagara Falls, ON, Canada.

7. Hadi Nazaripoor, Behnam Khorshidi, Charles R. Koch, Mohtada Sadrzadeh, Interface morphology of thin films: electrohydrodynamic vs electrokinetic model, Accepted in 24th International Congress of Theoretical and Applied Mechanics ICTAM 2016, August 21-26, 2016

To my father, mother and my wife
With love and eternal appreciation

Acknowledgements

I am eternally grateful and thankful to God, the Almighty Who continues to bless my life.

It has been an unforgettable experience and I like to thank a number of people for making four years of my life such an amazing time. Foremost, I would like to express my sincere gratitude to my supervisors Dr. Charles R. (Bob) Koch and Dr. Mohtada Sadrzadeh for their continuous support, patience and guidance and for providing me with a rich and rewarding academic experience. Bob and Mohtada have been more than supervisors for me, it was an honor to work with them and it is a pleasure to be friends with them. I have also been lucky to work with Dr. Subir Bhattacharjee and I would also like to thank him for his wisdom, and knowledge. His knowledge, experience and industrial point of view has been an invaluable help in my PhD thesis project as well as in developing my independent thinking and problem solving skills.

Thanks to my friends and lab mates for their support, friendship and help. I thank Behnam Khorshidi for the brainstorming discussions on different aspects of my research. I acknowledge the help from my friends Mehdi Rezaisary, Behnam Sadri, Babak Vajdihokmabad, Mica Yousuf, Arnab Atta, Ehsan Shahidi,Jannat Fatema, Ishita Biswas, Babak Soltania, Amir Hossein Mahdavi, Rouholluh Shokri in Advanced Water Research lab and Colloids and Complex Fluids Lab at university of Alberta. I would like to express my thanks to Josie Nebo and Ni Yang for their support and lab assistance.

A greatest thank you to my Mom and Dad for their love and sacrifice. No words can fully express my gratitude to my parents-in-law and my brothers Mehdi and Morteza. They have supported me in any and every possible way throughout my education. Many thanks to my grand-moms whom I am grateful for their assistance. Your prayer for me is what sustains me thus far.

I would like to sincerely thank my beloved wife, Fatemeh Kiakojori for her love, understanding and support, and for being with me through ups and downs. Also special thanks goes to my lovely son KIAN. I feel lucky to have such lovely companions to spend the rest of my life with.

Contents

List of Tables

List of Figures

Nomenclature

A	Hamaker constant
Bi	Biot number
c_p	Heat capacity
d_i	Electrodes distance, i = 1; 2
D	Diffusion coefficient
e	Electron charge magnitude
$\vec{f}_e$	External body force
F_E	Electrostatic force
F_{os}	Osmotic force
h	Interface height
h_c	Convective heat transfer coefficient
h_0	Initial mean film thickness
$\bar{I}$	Identity tensor
k_B	Boltzmann constant
k_i	Thermal conductivity of layers, i=1 and 2
k_r	Thermal conductivity ratio
l_0	Born repulsion cut off distance
L	Domain length
L_s	Scaling factor for length

m	mobility of charges/ions
M	Molarity
$\bar{M}$	Modified Marangoni number
$\vec{n}$	Normal vector to the interface
$n_{\pm}$	Number concentration of ions/charges, positive or negative
n_{∞}	Bulk number concentration of ions/charges
N_A	Avogadro number
N_x	Number of grid points in x direction
N_y	Number of grid points in y direction
P	Pressure
P_{os}	Osmotic pressure
$R_{\pm}$	Production rate of species due to chemical reactions
$\vec{t_i}$	Tangential vector to the interface, i=1 and 2
T	Temperature
T_g	Glass transition temperature
T_{room}	Room temperature
T_s	Scaling factor for time
$\vec{u}_i$	Velocity vector for film and bounding layer, i=1 and 2
$\vec{u}_{relative}$	Relative velocity
x	x direction in Cartesian coordinate
y	y direction in Cartesian coordinate
z	z direction in Cartesian coordinate

Greek Letters

ϵ	Amplitude for growth of instabilities

ε_i	Electric permittivity of film and bounding layer, i=1 and 2
ε_r	Electric permittivity ratio of layers
ε_0	Free space electric permittivity
ϕ	Conjoining/disjoining pressure
ϕ_{Br}	Born repulsion pressure
ϕ_{EL}	Electrostatic pressure
Φ_s	Scaling factor for conjoining pressure
ϕ_T	Thermocapillary pressure
ϕ_{vdW}	van der Waals pressure
γ	Relative interfacial tension between film and bounding layer
Γ	Threshold value of numerical convergence
κ	Inverse of Debye length
$\kappa^{\star}$	Wave number for growth of instabilities
κ^{*}	Mean interfacial curvature of the film interface
λ_{max}	Maximum wavelength for growth of instabilities
λ	Wavelength for growth of instabilities
μ	Dynamic viscosity
ν	Kinematic viscosity
ρ	Density
ρ_f	Free charge density
ψ_i	Electric potential within the layers, i=1 and 2
ψ_r	Reference electric potential
ψ_l	Electric potential of the lower electrode
ψ_s	Interface electric potential

ψ_{up}	Electric potential of the upper electrode
Ψ	Nondimensional electric potential
α	Surface tension gradient with respect to temperature
Δt	Time step
ΔT	Temperature difference
σ	Conductivity
σ_{lv}	Liquid-vapor interfacial tension
σ_{sl}	Solid-liquid interfacial tension
σ_{sv}	Solid-vapor interfacial tension
τ_c	Charge relaxation time
τ_p	Process time
θ	Contact angle

Subscript

0	Initial condition
C	Cold
H	Hot
L	Lower electrode
t	Time
U	Upper electrode
x	x direction
y	y direction

Abbreviations

DAE	Differential algebraic equation
DL	Double layer

EHD	Electrohydrodynamic
EHL	Electrohydrodynamic lithography
FD	Finite difference
IL	Ionic liquid
LD	Leaky dielectric
PB	Poisson-Boltzmann
PD	Perfect dielectric

Chapter 1

Introduction [†]

1.1 Thin Liquid Film Dynamics

Thin liquid films and surfaces are pervasive entities present and commonly used in our daily life. They are present as decorative coatings to improve the aesthetical values of the product or protective coatings to improve the insulation or conduction of surfaces [7], an intervening media in liquid-liquid emulsions [8, 9] and occurs as a lubricant in the cornea of the eye [10]. Thin films have been used in a cooling technique for thermal management of semiconductors in space and earth applications [11].

In the technological processes where the stability of thin films is important, numerous theoretical and experimental studies have been conducted to understand the factors that lead to the rupture of the film [7–10, 12–20]. Thin film instability can be triggered either naturally (i.e. intermolecular forces) [16, 21, 22] or by externally applied forces (i.e. mechanical, thermal and electric forces) [8, 20, 23–30] . These perturbations can lead to a diverse range of dynamics ranging from stable films to ruptured films showing dry spots /or holes. This behavior is attributed to the intermolecular interactions which are typically not significant in bulk fluid dynamics [13]. Thin films are unstable when the wave length of fluctuations is larger than a critical value [12].

Films with thicknesses of 100 nm or less are called ultra-thin films and can be either stable or unstable depending on the sign of second derivative of interaction potential with respect to film thickness [12]. Natural intermolecular interactions (apolar [12, 15, 31], and polar [16] interactions) determine the

---

[†] Parts of this chapter is based on Refs. [2–6]

initial state of a thin film. The type and magnitude of these interactions depend on properties of system materials [32, 33].

1.2 Technological applications

1.2.1 Coatings

A variety of techniques have been used to cover the substrate or object surface either to decorate or protect it. To mention a few, vapor deposition (chemical or physical), chemical and electromechanical techniques, spraying, spin coating, dip coating and thin film coating are used in different applications, ranging from the food processing, pharmaceutical and chemical industry, printing and textile industry to the automotive industry. To have a homogeneous coated layer, dewetting behavior (i.e. dynamic, stability and drainage) of thin liquid film lying on the substrate as shown in figure 1.1 must to be understood.

Surface energy of the liquid film, the bounding fluid and the substrate (i.e. surface chemistry), initial film thickness, temperature gradient in the system are the main factors effecting the wettability of a liquid film lying on a substrate [16, 32, 34–36]. The dewetting process, includes the following major sequences: (a) growth of initial perturbations and their amplification, (b) drainage or rupture of liquid film, (c) formation of holes and growth in their size, (d) formation of a polygon network of straight liquid strings (also called rims), (e) lastly decay and break up in rims resulting in droplets formation (due to Rayleigh instability). In films with nanometer thickness, spinodal dewetting [22] is the main mechanism due to the long range intermolecular forces (van der Waals forces [32]) leading to the spontaneous rupture of film. In thicker films, heterogeneous nucleation due to the surface heterogeneity and/or homogeneous nucleation derived by thermal noise are responsible for the dewetting [36].

As noted above, the surface chemistry is the key factor in spreading or dewetting process. Dewetting is a dynamic process which starts with a non-equilibrium thin film. At equilibrium, a droplet on a homogeneous substrate forms a spherical cap with the contact angle of θ at the three phases contact line. The intermolecular interactions between two interfaces of liquid-vapor and solid-liquid are neglected in Young's definition.

The van der Waals interaction is the summation of Keeson, Debye and London dispersion forces [32, 33]. This interaction is defined as $\phi_{vdW} = A/6\pi h^3$

for the film lying on a substrate and bounded with another other layer. A is the effective *Hamaker* constants for the system which depends on the materials used for substrate and fluid layers [32, 33]. For instance, for three layered systems it is defined as: $A_{213} = (\sqrt{A_{33}} - \sqrt{A_{11}})(\sqrt{A_{22}} - \sqrt{A_{11}})$ where subscripts 1,2 and 3 denote substrate, liquid film and bounding fluid, respectively. Liquid films with a negative effective *Hamaker* constant, remain stable and do not dewet the substrate. The other relatively short range interaction (a few Angstroms distance) is steric repulsion that should be included in analysis.

In order to investigate the dynamic of dewetting process and film rupture, the "thin film" equation thickness is much smaller than the wavelength of the fluctuations, long-wave approximation is used to simplify the governing equations (mass and momentum conservations). It is also assumed that the liquid film is charge-neutralized and double layer (charge diffuse layer) forces are negligible.

$$h_t + A^{'}(h^{-1}h_x)_x + S(hh^3h_{xxx})_x = 0 \tag{1.1}$$

where, h is the interface height and $A^{'} = \frac{A}{6\pi h_0 \rho \vartheta^2}$ and $S = \frac{h_0 \sigma}{3\rho\vartheta^2}$ are dimensionless *Hamaker* constant and interfacial tension, respectively.

To get the smooth thin liquid coated film, all the interfacial defects in coating, like effects of surface tension, viscosity, drying, non-Newtonian rheology and Marangoni flows (effect of temperature gradient) [37–42] should be uniformed before coated liquid dries. Another source of defects in liquid thin film coating is the accumulated electrostatic charges on the webs, rollers, etc. The accumulated charges may cause technical defects like spark ignition and attract dust particles which deteriorate the level of coatings which are in addition to the electrohydrodynamic (EHD) induced instabilities in coated film [43]. This shows the importance of understanding the dynamics and dewetting process of thin coated liquid film in the coating industry.

1.2.2 Emulsions and foams

Thin liquid films are present as an intervening media, which separates the dispersed phase, in gas-liquid in food foams or in liquid-liquid (water-in-oil or oil-in-water) emulsions (see figure 1.2) [8, 44].

Instability and drainage of thin liquid film results in coalescence of gas bubbles and oil (or water) droplets leading to larger size bubbles and droplets. The coalescence of bubbles and/or droplets makes the emulsion and foam to be unstable and called demulsification. In time, the average size of bubbles and droplets increases as the foams and emulsions are inherently unstable. In food and pharmaceutical industry which requires the stable emulsions and foams, surfactants are used as emulsifiers [45]. However, in the oil industry, several techniques are used like chemical demulsifier, filtration, electrostatic demulsification and heat treatment to enhance the separation of water-in-oil emulsions [8].

Understanding the interaction between soft materials such as drops/ bubbles and liquid films require knowledge of the relation between shape change and their corresponding interaction strength. In soft bodies interactions, there are number of distinguishing properties like interfacial deformations and forces which are absent in solid body interactions [46]. The important factors in drainage dynamics are: inertial separation, inertia of the drop/bubble, viscosity of fluids, surface tensions, hydrodynamic behavior of thin film, and type of surface forces (i.e. intermolecular forces) [8, 46].

First part of coalescence process is when the thin liquid film is still thick enough to just consider the hydrodynamic interactions and employ Reynolds lubrication theory. At this stage the intermolecular forces such as van der Waal force and electrostatic forces are also not considered [46, 47]. When the film thickness is in the range that the intermolecular forces have dominant role they will affect the variation of thin film shape [9, 48, 49]. The gravity effects can be neglected in the dynamics behavior when the intervening film thickness is in micro-/nanometer range. To mathematically model the droplet deformation in an equilibrium condition, augmented Young-Laplace equation [46] which is based on the minimization of the isothermal Helmholtz surface energy of the system is used. To find the hydrodynamic and drainage of thin film, StokesReynolds hydrodynamics approach has been used (similar to eqn. 1.1 but in cylindrical coordinate). Since thinning process and the drainage is a time dependent process, the aim is to find the time rate of change of the drops/ bubbles shapes and the film configurations. One of the challenges in the quantitative analysis of these systems is having length scales in many orders of magnitudes from submicron to milimetter. For instance, drops/ bubbles have typically size of millimeter while the film has nanometer thickness and the interaction between them causes a deformation in the order of tens or hundreds of micrometer. Moreover, governing equations (i.e. conservation of mass, momentum, stress balance and kinematic boundary condition at film interface) in thin film studies are highly non-linear also there are stable/unstable conditions and transient behavior of deformable drop/bubble or thin film which is reported in experimental results [46].

1.2.3 Lithography (micro- and nano-patterning)

Decreasing the feature size on integrated circuits by the fabrication of nano-sized patterns is a significant challenge to the semiconductor industry [50]. The need for powerful microprocessors and cheaper electronic memories has accelerated the research efforts on finding novel, fast and inexpensive techniques for creation of nano-sized features. In addition to conventional lithographic techniques (based on the use of electrons, photons or ions) which are commonly used in semiconductor industry, other techniques like nanoimprinting [51, 52] and soft lithography [53], have recently gained attention due to their ability in creation of nano-sized structures. Other alternatives are contactless pattern transfer methods which are based on self-organization [54–57] and surface instabilities [58, 59]. In the surface instabilities category, for ultra-thin (thickness less than 100 nm) liquid/molten polymer films, surface instability and subsequent drainage and pattern evolution determine the size and shape of the surface features. Interface instability can be triggered using external forces (mechanical, thermal and electrical) [23, 60–63] as well as intermolecular interactions (van der Waals and polar interactions) [54].

Electrically induced instability of thin liquid films is a contactless pattern transfer method which has gained extensive attention due to its ability in creation of novel micro- and nano-sized structures ranging from bifocal microlens arrays [64], micro and nano channels, [65] and biomimetic mushroom-shaped microfibers[66] to high-aspect-ratio micropillar arrays [67]. In this process, a thin spin coated and baked film is confined with upper electrode (see figure 1.3). The thin film is heated to above its glass transition temperature and the resulting molten polymer film is subjected to transverse electric field (normal to the interface). Depending on the applied voltage and viscosity of liquid film the patterning process may take from two hours to two days. At the end, the system is cooled down to room temperature to freeze (solidify) the formed pattern on the film.

There has been many efforts to reduce the structure sizes from micron to submicron level over the past decade [59]. However, fabrication of ordered nano-sized features has been challenging in large domain area (i.e. cm^2 sized domain) [1, 68]. The main focus of this thesis is the application of electrically induced instabilities of nanofilms, thin liquid film with thickness less than 200 nm, for the creation of compact and well ordered submicron sized patterns.

The polymer film in EHD patterning process is typically assumed to behave like a perfect dielectric (PD) with no free charges, or leaky dielectric (LD) with infinitesimal amount of charges. However, when the thickness of film is in range of sub-micron level (nanofilms), the diffuse layer of charges are comparable to the film thickness. Additionally, ionic conductive materials with finite diffuse layer thickness, also called Double layer (DL), has been recently used in EHD patterning of nanofilms to avoid electric breakdown in air [1] due to high applied electric field. This provided motivation for this work to investigate the EHD patterning using a new electrostatic model which consider the finite diffuse layer of charges or ions in film. This overcomes the shortcoming of assuming very large and small electric diffuse layer inherent in the PD and LD models respectively.

The isothermal assumption is often used in the theoretical models used for EHD patterning process. In this thesis, this constraint is removed and the thin film equation is re-derived considering energy balance in addition to mass and momentum conservation equations. Then the effects of thermocapillary force are investigated.

1.3 Scope and objectives

The main objectives of this thesis that define the scope of the work are:

- Development of a comprehensive electrostatic model for electrohydrodynamic patterning of thin liquid film with finite charges/ions diffuse layer,
- Characterizing different morphological behaviors in bilayers with relative electric permittivity of layers and initial layer thicknesses,
- Investigation of the effect the electrostatic heterogeneity on creation of ordered patterns,
- Investigation of the thermocapillary effect on the non-isothermal electrohydrodynamic patterning process of thin liquid films.

1.4 Thesis organization

In Chapter 1 the potential technological applications related to this research project are briefly introduced along with their background theories. The research objectives and the scope of the work and the organization of the thesis and the contributions are described.

In Chapter 2, a detailed literature review for electrically and thermally induced patterning is provided with a focus on identifying the limitations in the theoretical models presented in the literature.

In Chapter 3, the mathematical model describing the dynamics, spatiotemporal evolution of thin liquid film are presented. This includes, the hydrodynamic governing equations, intermolecular interactions, external forces applied to the film interface and assumptions used to derive the thin film equation. Next, the modeling approach and the numerical scheme used to solve the nonlinear thin film equation are discussed. The grid dependency and the accuracy and consistency of results are detailed and compared with literature results including experiments. This chapter is based on Ref. [2–6].

Chapter 4 is divided into two sections of EHD patterning of nanofilms using ionic liquid electrostatic model in (i) a homogeneous electric field (flat electrode) and (ii) a heterogeneous electric field (electrode with strip and square block protrusions). The dynamics and morphological evolution of film interface are discussed and compared with the base-case PD model results. In the second part, the need for using patterned electrode to apply heterogeneous electric filed is discussed. Then the influence of electrostatic heterogeneity on the electric-field-induced destabilization of thin IL and PD films are presented. This chapter is based on Ref. [3, 4].

In Chapter 5, a numerical investigation is performed to investigate the morphological behavior of bilayers with an electric permittivity ratio of less than one ($\varepsilon_r < 1$). The morphology of film and its drainage time under the effects of filling ratio and electric permittivity ratio are studied. Finally, the perfect dielectric (PD) upper layer is replaced with IL layer to investigate spatiotemporal behavior of the bilayer. For the IL layer, a more comprehensive electrostatic model based on the coupled nonlinear Poisson-Boltzmann and Laplace equations is used to obtain the electric potential distribution within layers and consequently the electrostatic pressure acting on the interface in the bilayer. This chapter is based on Ref. [2].

In Chapter 6, the combined thermo-electrohydrodynamic instability of thin liquid film is investigated. Modified Marangoni number and thermal conductivity ratio, on the growth rate and characteristic wave length of instabilities are first investigated using LS analysis. Then the modified non-linear thin film equation presented in Chapter 3 is numerically solved. The thermocapillary (TC) and electrohydrodynamic (EHD) base cases are investigated and compared. Finally results are expanded to the combined TC-EHD patterning. This chapter is based on Ref. [5].

In Chapter 7, the main concluding remarks of the analytical and numerical studies of this thesis are explained and the main contributions of this work are highlighted. Finally, an overview of possible future steps and directions of this work and and research contributions are listed.

1.5 Thesis Contributions

The polymer film in EHD patterning process is typically assumed to behave like a perfect dielectric (PD) or leaky dielectric (LD). In chapter 3, a more comprehensive electrostatic model (ionic liquid (IL) model, eqns. 3.19 and 3.21) is developed for a finite electric diffuse layer which overcomes the shortcoming of assuming very large and small electric diffuse layer inherent in the PD and LD models respectively. The diffuse layer thickness form, even with having infinitesimal of charges, in nanofilms is comparable with the film thickness which confirms the need for using IL model in EHD patterning process of nanofilms. To create well ordered structures a patterned electrode is used to create heterogeneous electric field on the film interface. Effects of protrusions height, their center to center distance are documented for the creation of compact and well ordered structures. Moreover, in the theoretical models for the EHD patterning, it is assumed that the liquid film is isothermal over the patterning process. However, experiments showed that the thermal gradient induced instabilities in nanofilms results in pillar formation. The thermal terms are introduced and the themo-electrohydrodynamic instabilities in thin liquid films to assist the EHD patterning process are simulated and documented. This provides a novel pathway for the creation of nano-sized pillars.

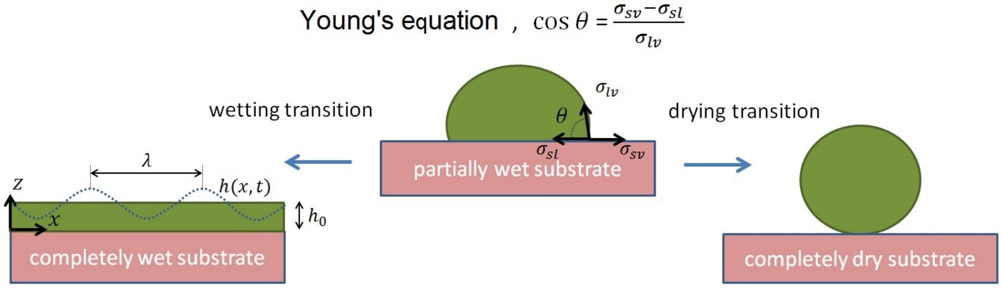

Figure 1.1: Sketch of a dewetting process, a liquid film dewets into one drop at top of a solid substrate. In the Young's equation, θ is an equilibrium contact angle, σ_{sv}, σ_{sl} and σ_{lv} are solid/vapor, solid/liquid and liquid/vapor interfacial free energies. Initial wetting, $\theta = 0$, partial wetting by $0 < \theta < \pi$, and nonwetting by $\theta = \pi$.

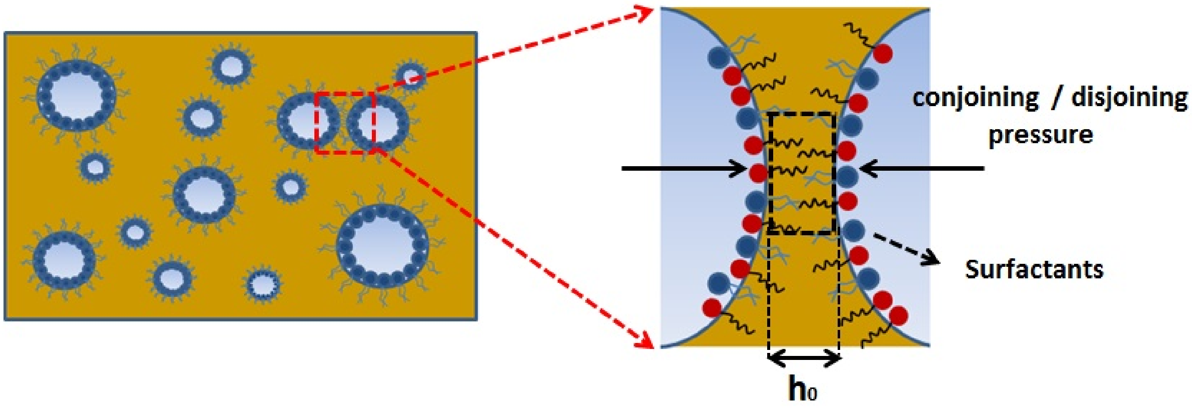

Figure 1.2: Schematic view of thin film entrapped between two droplets. h_0 is the film thickness.

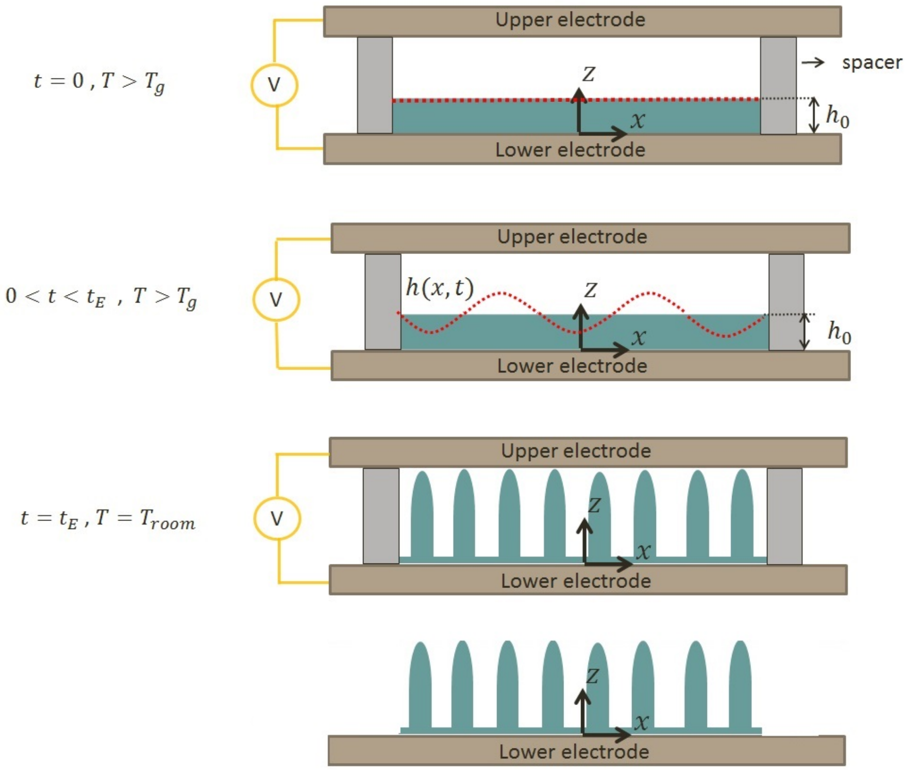

Figure 1.3: Schematic view of thin film sandwiched between two electrodes. h_0 is the film thickness, T_g is the polymer film glass transition temperature, t_E is the time which voltage is applied to the system .

Chapter 2

Literature review [†]

2.1 Electrohydrodynamic instability

Numerous studies have been conducted on electrohydrodynamic (EHD) since initial exploration in 17th century [69] where a conical shape is formed on a sessile drop after placing a charged rod close to the top [70–74]. Early studies focused on either perfect conductor (PC) liquids like water and mercury or perfect dielectrics (PD) like benzene. Deformation and the bursting of fluid drops in presence of electric field is experimentally examined [72] resulting the understanding the role of conductivity in behavior of an isolated emulsion drop in an electric field [71]. This resulted in the theory of leaky dielectric (LD) or poorly conducting materials. EHD flow is still being intensively studied due to its numerous industrial applications such as de-emulsification [8], microfluidics [75], lab on a chip [76, 77] and lithography [23, 59].

In macroscopic systems where the influence of gravity is important, to generate the milimeter sizes of humps at the interface thousands of volts is needed to deform the interface between either non-conducting fluids like oils and air or conducting ones like water, alcohol and mercury. The need for high applied voltage and small deformation results makes these systems impractical. However, the produced features had certain patterns and could be used as a possible technique in pattern creation.

In 1999, micro-sized pillar arrays created on a molten polymer film confined between two conductive substrates [78] without any external electric field application. The patterns are induced by an internal electric field due to entrapped charges in the molten polymer and the substrates. In this experiment, a polymer film spin coated onto a conductive substrate (i.e. electrode) and

---

[†] Parts of this chapter is based on Refs. [2–6]

another flat and patterned substrate placed at the top using non-conductive spacers. The system is heated up to the glass transition of polymer and after a while system is cooled down to the room temperature. The scanning electron microscope (SEM) and atomic-force microscopy (AFM) images of the interface revealed the micro pillar arrays formation on the film.

A year later, similar steps demonstrated pillars formation in a molten polymer film exposed to an external electric field [23]. These findings have attracted many researchers because of the potential applications in making micron and submicron structures on wide range of materials which could be faster and cheaper than other conventional techniques that need exposure, development and etching stages. The pattern formation process is called EHD patterning as it is based on the existence of an electric field either internally or externally and resulting fluid flow in the liquid film.

In electrohydrodynamic lithography (EHL), a molten thin polymer film which is heated to above its glass transition is subjected to an electric field to destabilize the film to create well-controlled micro- and nano-patterns. The film patterning process relies on the EHD flow in the polymer film so this process will be modeled and simulated. The EHD patterning process starts with an initially flat (thermal motion is neglected) liquid thin film that is confined between two electrodes (the initial thin film height is denoted h_0 in figure 2.1). The liquid film is bounded with either air or another polymer film to fill the gap between electrodes. Applying a transverse electric field induces the electric pressure (Maxwell stress [79]) at the film interface that perturbs the pressure balance and enhances the most unstable wavelength of growing instabilities on the film interface. The pattern formation process may take from an hour to a week depending the viscosity of polymer film and the applied voltage [23, 80]. Finally the formed patterns can be frozen by cooling the system to the room temperature.

2.1.1 Theoretical studies

The disparity of electrical properties of the film and the bounding fluid (the material which fills the gap between the film and the upper electrode), results in a different electric field in each layer. As a consequence, a net electrostatic force acts on the interface due to the Maxwell stress. In the EHD patterning process, thicker regions of film are subjected to higher electrostatic force compared to thinner regions, thus the electrostatic pressure increases the instabilities. In contrast, capillary pressure tend to damp the instabilities. When the electrostatic pressure overcomes this damping pressure, instabilities grow and pillars (raised columnar structures) form on the interface with the characteristic wave length of λ.

Using a simple analysis by comparing the order of magnitude of electrostatic pressure and capillary pressure gives the relation between influential parameters such as applied voltage V, interfacial tension γ, electrodes distance D, film thickness H and the characteristic wave length as follow:

$$\varepsilon_0\varepsilon(\frac{V}{D})^2 \propto \gamma\frac{H}{\lambda^2} \implies \lambda \propto \frac{\gamma^{1/2}H^{3/2}}{V^{-1}}$$

It can be seen that in this relation λ is independent of polymer film viscosity (viscosity ratio of layers in case of bilayer and trilayer systems). However, it is shown that the molecular weight of polymers which changes the molten polymer viscosity significantly affects the patterning time scale.

Linear stability analysis

The formation of structure and their periodicity has been explained using Linear stability (LS) analysis [23, 81]. The LS analysis has been extensively used as the common approach in the investigation of thin liquid film dynamics and it's rupture [13, 17, 21, 31]. In this regard, the thin film equation has been used with addition of electrostatic force acting on the film interface as an external body force. The dominant wavelength for growth of instabilities (λ) which characterizes the center-to-center distance of pillars in a hexagonal pattern is predicted by LS analysis [23, 59, 82]. The LS analysis shows that the lateral size of pillars decreases by increasing the applied voltage (V), mean initial film thickness (h_0), electric permittivity of film (ε) and its conductivity (σ). Depending on the relative dielectric constant of the film and the bounding layer (other than air) and their thickness ratios, either pillar or holes can be formed in the EHD patterning process [83].

Thermodynamic analysis

Another approach is to consider the patterning process from thermodynamic point of view. Electrohydrodynamic (EHD) pattern formation is an energy driven process [84] where the dynamics of structures (i.e. pillars, holes and bicontinuous patterns formation) form to minimize the main energy component, the electrostatic energy. From a thermodynamic point of view, the film evolves to lower the free energy of system [82, 84] such that at steady state the lowest interfacial energy determines the final structure.

The thermodynamic description of pattern formation has been found by deriving the thin film equation to find the total and individual energies present in the system integrating into the system energy ($E_t = E_{elec} + E_{vdW} + E_{surf}$) using the Lyapunov function. In which, E_{elec} is the energy associated with the electrostatic pressure, E_{vdW} stands for the van der Waals pressures and E_{surf} is for the the surface tension or capillary pressure present in the EHD patterning system. It is shown that, pillars and holes can be formed at either short time as they have the fastest growth rate or at long time as the formed pillars (holes) coalesce and reform into an isolated pillar (hole) due to the thermodynamic preference [84]. From the energy aspect, the dynamics and evolution of patterns are mainly cased by the minimization of electrostatic energy, but the shape of the pattern at the final steady state is typically selected to have the minimum interfacial energy. Comparing the thermodynamic approach and the kinematic one assists in determining of a critical filing ratio (ratio of film thickness to the electrodes distance) at which the pillar formation is the favored low energy state or the hole formation.

Non-linear analysis

Various numerical techniques are used to track free interfaces like volume of fluid (VOF) [85] and marker-and-cell [86]. Commercial package of COMSOL Multiphysics has phase field and level set methods which have been used recently to numerically simulate the multiphase system (film and the bounding) in the EHD patterning [65, 87–89]. All these methods consider the full NavierStokes (NS) equations to track the interface. These techniques are applied as a versatile tools to visualize the transient evolution of thin liquid film subject to a transverse electric field. However, the computational cost and approximate tracking of the interface location are disadvantages of these types of non-linear studies.

Another approach in tracking the interface height is using so called *thin film* equation which is based on the Reynolds lubrication approximation [17, 90]. In this approach the interface height is directly tracked using the kinematic boundary condition which is commonly used to correlate the deformable interfaces height to the velocity field. Since height of film and its deformations are much smaller than either film's lateral dimension or the characteristic wavelength for growth of instabilities, the Reynolds lubrication approximation is used to simplify the governing equations and the corresponding boundary conditions.

2.1.2 Electrical heterogeneities

In early efforts using EHD pattering, ideally flat mask or electrode has been used to create multidomain features and is found as a cost-effective and convenient way to produce small features since there was no need for expensive steps like using patterned mask, exposure of beam and lights and using toxic chemicals. However, pattern formation relies on the periodic and/or self-assembly interface instabilities leading to pattern generation based on the the natural tendency of system as explained above. The spatial ordering in large domain area is main limitation in this technique as the hexagonally ordered pillars typically extend less than 40 periods [91]. In addition, in some cases pillars are randomly distributed over the patterning area and less likely had circular cross-section. To overcome this challenge, a patterned electrode is used in which electrode have strip like or block shape protrusions (see figure 2.2) [68, 82].

Reducing the electrodes distance increases the electric field exposed to the polymer film and consequently increases net electrostatic force acting on the interface. When the polymer film behaves like an insulators (perfect dielectric), the electric field is given by:

$$E_p = (\frac{V}{\varepsilon_p D + (1 - \varepsilon_p) H})^2$$

Hence, thin film experiences higher electrostatic force under the protrusions and this pushes the interface toward the upper electrode more than the surrounding regions. In general, the electrical heterogeneity, results in non-uniform electrostatic force application on the film and results in formation of wide variety of structures with change in the protrusions height, width, center-to-center distance and their periodicity [68, 82]. Adjusting the width and height of protrusions are found challenging to fabricate desired pattern without also creating secondary pattern formation.

The electrical heterogeneity also has been combined with the chemical heterogeneity of the lower substrate [92, 93]. This chemical heterogeneity (unevenly distributed intermolecular forces like van der Waals and spreading) can be due to an uneven oxide layer, cavities and contamination. Also, substrate can be deliberately tailored to use short range forces in the self-organized patterning as used for nano- and micropatterns generation in ultra-thin films [94].

2.1.3 Electrical properties of liquid film

Electrostatic force is the main driving force in the EHD patterning process. Depending on the electrical properties of a polymer film different theoretical models have been used to predict the structure sizes. The majority of experimental and theoretical studies are performed considering the liquid thin film layers to be either perfect dielectrics (PD) [23, 82, 93, 95, 96], with no free charge, or leaky dielectrics (LD) [95, 97–100], with infinitesimal amount of charges. In ideal PD materials, the conductivity is zero so when a potential difference is applied across the PD material, the electric field and potential drop depend on the electric permittivity or polarization of film in the presence of electric field. In LD materials, charges move and accumulate on the interface when an electric field is applied. When the charge relaxation time (the time required for movement of charges in response to electric field) is larger than growth rate of instabilities, LD films can be modeled by PD theory. When charges migrate and accumulate at interface before pattern formation occurs, then the charge conservation equation must be solved simultaneously with the fluid flow equations. The presence of free charges at the interface results in a significant increase in electrostatic force and consequently it decreases the structure length scale [100].

The PD and LD models predictions match with some experimental results but not for all experiments [81, 95]. The reduction in structure size has been challenging and different methods have been examined to overcome this limitation. When the gap between the polymer film and the upper electrode is filled with other polymer layers, this results in more complex features such as cage-like [101], hierarchical [102], core-shell and embedded [103] structures. The size and shape of these structures is directly related to the relative electric permittivity ratio of layers (ε_r) that defines the strength and direction of electrostatic force acting on the interface. Using the LD material for both film and the bounding layer, the theoretical model predicts 50 times decrease in the period [104]. Based on the LS analysis, the center to center distance of pillars, λ, can be reduced with an increase in the applied voltage. However, experimental results did not match with the theoritical predictions based on the PD and LD models and the electric breakdown of either polymer film or the air are reported as the possible reason for this discrepancy [95].

Applying sufficiently strong DC electric field to the thin liquid film or pendant drop can destabilize the air-liquid interface leading to a conical shape formation, referred to as a DC Taylor cone [105–108]. Subsequently, drop is emitted from the cone's tip due to the jet breaking. Such EHD cone-jetting phenomena, known as electrospraying, has been used extensively as a popular technique of electrospray mass spectrometry [109, 110].

In the context of EHD patterning, the DC Taylor cone formation has just been reported in the bifocal microlens fabrication using EHD reflowing of pre-patterned polymer films [111], where the steady state pattern formation is achieved using critical electric field intensity. The Taylor cone shape is observed when the electric field intensity slightly exceeds the critical value of 10 MV/m resulting in switching from ordinary single-focus microlens to the bifocal ones. In contrast with the electrospraying in EHD patterning a finite mass is exposed to the electric field and the creeping flow (high viscosity and low velocity) hinders the tip streaming and drop emissions.

Electric breakdown of a polymer film and the bounding fluid at high electric field strength is a limiting factor in the EHD patterning especially, when fabrication of nano-sized features is needed [1]. A significant discrepancy between theoretical predictions and experimental results (for both PDs and LDs) can also be attributed to this breakdown [1, 95, 112]. Employing ionic conductive polymers or simply ionic liquid (IL) films as a bounding fluid enhances the electrostatic pressure acting on the interface while preventing electric breakdown [1]. It is shown that in polymer-ionic liquid bilayer system, the maximum wavelength (λ) can be decreased into submicron level with an increase in applied voltage and/or decrease of polymer film thickness. However, it must be noted that thinner films have higher tendency of dielectric breakdown mainly when the film thickness is less than 50 nm [1].

Ionic conductive materials can be polymerized ionic liquids, ionic salt like materials (high temperature or low temperature), and aqueous or non-aqueous electrolytes [1, 32, 113–116]. To mathematically model the ions distribution within the IL film the Poisson-Nernst-Planck (PNP) model has been used [1, 114, 116]. When the process time is much smaller than the free charges/ions relaxation time the PNP equation can be simplified to the Poisson Boltzmann equation which relates the electric potential to the charges distribution across the film [1, 116].

Free ions present in ILs move easily and form a diffuse layer called a double layer (DL) adjacent to the charged surfaces. In the PD and LD models, it is assumed that the thickness of the DL is very large and small, respectively.

Initially, to bridge the gap between these two limiting cases, an electrokinetic model was developed for drop deformation in an electric field [117, 118]. Recently an electrokinetic model has also been developed to study EHD patterning and LS analysis is used to investigate the dynamics of polymer films [116]. These electrokinetic models apply the linearized Debye Huckel approximation [33] to study the stability of IL films.

2.2 Thermocapillary instabilities

In thin liquid films resting on a solid substrate, variation of temperature along the interface results in surface tension nonuniformity which breaks the mechanical equilibrium. The resulting interfacial shear stress leads to a convective motion of fluid. Viscosity and mass continuity carry this interfacial motion to the bulk. Along the interface, viscosity tends to stabilize this perturbation. Generally, the instability in liquid films due to interfacial tension inhemogenities is known as Marangoni instability [119] and if the interfacial tension inhemogenity is caused by a thermal gradient at the interface, it is called Thermocapillary (TC) instability.

In 1900, B′enard experimentally observed the self-organized cellular convective structures on the heated liquid layers. Two main instability modes can be generated in TC: the short-wavelength (SW) mode in thick films which results in cellular convection patterns or so called B′enard convection cells. In this case, the interface is not deformed as the film is much thicker than the characteristic wave length. The other mode is the long-wavelength (LW) occurs in thinner and more viscous films and results in the interface deformation [120, 121]. Dynamics, instability and evolution of heated thin liquid films have be previously investigated using linear and nonlinear stability analysis [90, 122–126].

Acoustic phonos (AP) model [25] and TC flow model [61] are two mechanisms have been proposed to describe nanofilm instability induced by temperature gradient. The AP model is based on the radiation pressure induced by low frequency acoustic phonons and is based on material properties of the nanofilm. Previous experimental studies have shown that the long wave instability presented in TC model is the primary reason for the formation of nanopillar arrays [61, 62].

In the EHD patterning, the thin liquid film is typically assumed to be isothermal during its evolution process. LS analysis shows that, lowering the interfacial tension leads to smaller structures. Since increased temperature reduces the interfacial tension (in commonly used materials in the EHD) combining the TC effect with the EHD process is predicted to result in the formation of smaller sized features. A theoretical analysis of the simultaneous effect of temperature gradient and the EHD in the patterning of both Newtonian and viscoelastic films shows that for 1-D films, the LS analysis predicts creation of smaller structures when EHD and thermal forces are combined [127]. In [127], they examined and compared their results for both LD and PD electrostatic models. For both PD and LD films a decrease in solvent viscosity and Deborah numbers increases the growth rate and consequently results in smaller λ_{max}. They have also shown a similar rate of patterning using nonlinear analysis for a Newtonian film, which deviates from the linear predictions when the interface height reaches 90% of the gap distance. The dynamics and mechanism of pattern formation in combined TC-EHD assisted patterning of nanofilms using a 3-D nonlinear formulation have not been analyzed so far and are described in Chapter 6.

2.3 Summary

The reduction of the structure size from micron to submicron level using EHD instability is found to be challenging due to electric breakdown in either polymer film or the bounding layer. Both PD and LD models failed to predict the experimental observations when a high electric field applied to the system mainly when the film thickness is less than 100 nm. Presence of finite amount of charges or using ionic conductive materials that results in having finite electric diffuse layer which is comparable to the film thickness is another limitation of the electrostatic models which have been used in the EHD patterning simulation and analysis. Therefore, a more comprehensive electrostatic model is needed to overcome these shortfalls. Introducing a bounding layer instead of air can result in the creation of more complex and even smaller features. In this study, the EHD patterning of both single layer and bilayer films can examined. Another goal of this study is to investigate how to create smaller sized pillar arrays (compact features) by integrating the EHD patterning process with the TC model in a long-wave limit formulation. The effects of Marangoni number and thermal conductivity ratio of layers on the time evolution, the shape and the size of structures are investigated using analytical LS analysis and nonlinear numerical simulation.

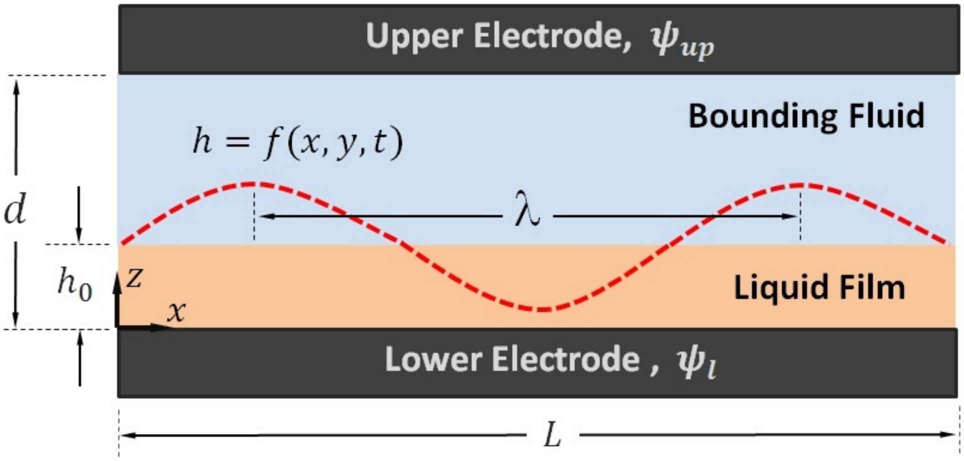

Figure 2.1: Schematic view of the thin film sandwiched between electrodes. $h = f(x, y, t)$ is the film height described by the function with the lateral coordinates and time. λ is the maximum growing wavelength.

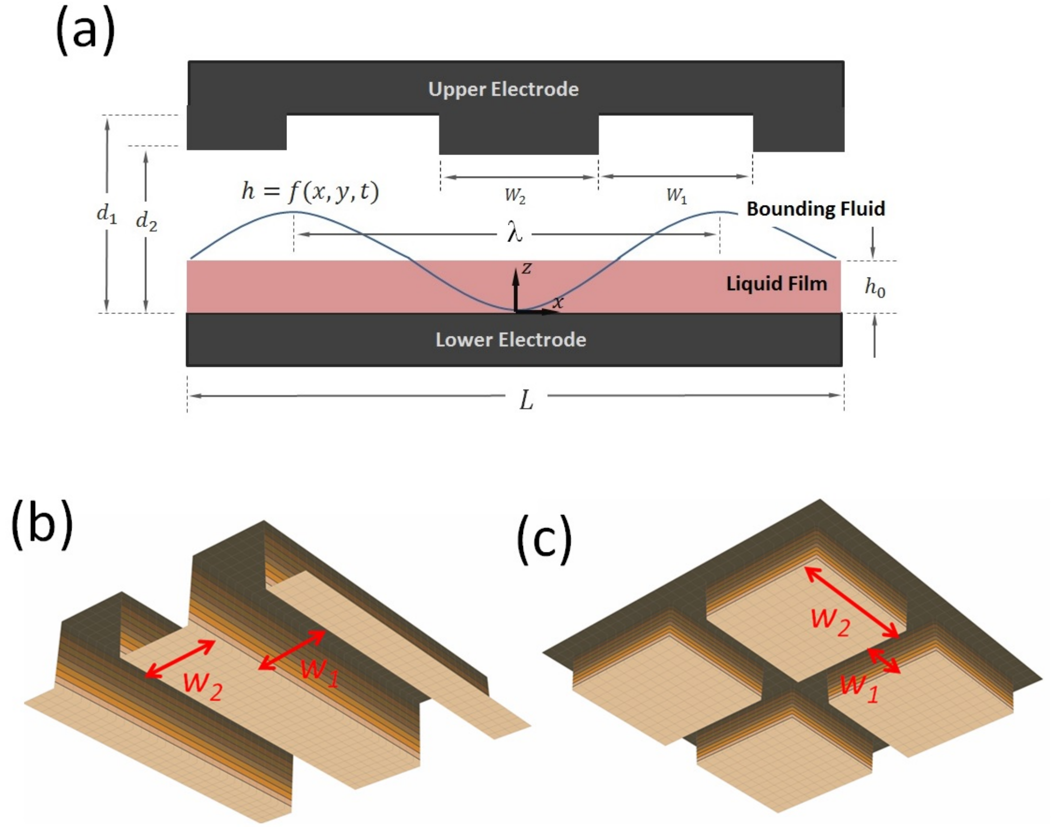

Figure 2.2: 2-D Schematic representation of (a) thin liquid film sandwiched between two electrodes and 3-D schematic of upper electrode with (b) strip-like (c) square block protrusions.

Chapter 3

Theory and Numerical Formulation [†]

In this chapter, the governing equations responsible for the interface dynamic along with the corresponding boundary conditions will, first, be discussed in details. This includes: hydrodynamic, electrostatic, thermocapillary and intermolecular sections. Then the numerical method used to track the interface height over the evolution time is presented in detail.

3.1 Mathematical model

Interface instability can be triggered using external forces [23, 60–63] (mechanical, thermal and electrical) as well as intermolecular interactions (van der Waals and polar interactions) [54]. Development of these instabilities at the liquid film interface gives rise to the film disruption and/or pattern formation on the film interface, which is of interest in numerous applications.

Determining drainage time (i.e. time when film's rupture occurs) and different morphological structures of the film interface requires insight into the dynamics and morphological evolution of the film. From bulk fluid dynamics, interfacial tension and viscosity are known as damping factors for fluctuations on the free surfaces. Small scale systems also have intermolecular forces which depend on material properties of the films and substrate, and these forces play a dominant role in creation and enlarging instability of thin films [32, 33]. In what follows the governing equations describes the hydrodynamic of interface under influence of external and intermolecular forces will be discussed.

[†] Parts of this chapter is based on Refs. [2–6]

3.1.1 Governing equations

A schematic of the thin film sandwiched between electrodes is shown in figure 3.1. Thin liquid film is uniformly heated from below and cooled from top. Thin film evolution is described using creeping flow equations ($Re \ll 1$, due to small film thickness). To capture the effects of thermocapillary, energy balance is also considered. The equations are:

$$\nabla.\vec{u}_i = 0 \tag{3.1}$$

$$\rho_i(\frac{\partial \vec{u}_i}{\partial t} + (\vec{u}_i.\nabla\vec{u}_i)) = -\nabla P_i + \nabla.[\mu_i(\nabla\vec{u}_i + (\nabla\vec{u}_i)^T)] + \vec{f}_e \tag{3.2}$$

$$\rho_i c_{p_i}(\frac{\partial T_i}{\partial t} + \vec{u}_i.\nabla T_i) = k_i \nabla^2 T \tag{3.3}$$

Subscript i denotes the fluid phase (film and bounding layer). Thin film is considered to be a Newtonian, incompressible fluid with a constant electric permittivity. It is assumed that the film thickness is sufficiently thick over the evolution time that the continuum assumption remains valid. Gravity effects is disregarded as the film thickness, h, is less than 200 nm. It is assumed that energy dissipation due to viscous forces is negligible in the energy balance. The hydrodynamic and thermal boundary conditions are given at the wall and the interface.

On the walls the boundary conditions are:

$$\vec{u}_1 = 0 \;\; ; \;\; T_1 = T_H \quad at \;\; z = 0$$

$$\vec{u}_2 = 0 \;\; ; \;\; T_2 = T_C \quad at \;\; z = d$$

At the interface ($z = h(x, y, t)$) the boundary conditions are:

$$\vec{u}_{relative} = 0$$

$$T_1 = T_2$$

$$\text{thermal conduction:} \qquad \vec{n}.k_1\nabla T = \vec{n}.k_2\nabla T$$

$$\text{thermal convection:} \quad \vec{n}.k_1\nabla T + h_c(T_1(z = h) - T_C) = 0$$

and stress balances (normal and tangential)

$$\vec{n}.\bar{\sigma}_1.\vec{n} - \vec{n}.\bar{\sigma}_2.\vec{n} = \kappa^{\star}\gamma + \vec{f}_e.\vec{n}$$

$$\vec{t}_i.\bar{\sigma}_1.\vec{n} - \vec{t}_i.\bar{\sigma}_2.\vec{n} = (\nabla\gamma + \vec{f}_e).\vec{t}_i$$

The stress tensor is defined as $\bar{\sigma} = -P\bar{I} + \mu_i(\nabla\vec{u}_i + (\nabla\vec{u}_i)^T)$ in which μ_i is the dynamic viscosity. The external body force is defined as a gradient of a potential, $\vec{f_e} = -\nabla\phi$, and term ϕ is called conjoining pressure. The normal and tangent vectors of the interface are $\vec{n}$ and $\vec{t_i}$, respectively and $\kappa^\star$ is the mean interfacial curvature of the film interface [128].The surface tension, γ, is approximated to have linear [90] dependence to temperature ($\gamma = \gamma_0 - \alpha(T - T_0)$ with $\alpha > 0$) in which α (N/mK) is surface tension gradient and T_0 is the reference temperature. Finally, to relate the interface height to interfacial velocity components, a kinematic boundary condition is [15]:

$$w = \frac{\partial h}{\partial t} + u\frac{\partial h}{\partial x} + v\frac{\partial h}{\partial y} \quad at \quad z = h(x, y, t) \tag{3.4}$$

In the EHD (TC) pattern evolution process, the electric field (temperature gradient) destabilizes the interface of the liquid film and bounding fluid, leading to the evolution of interface with the height of $h = f(x, y, t)$. The wavelengths of the growing instabilities, λ, are much larger than the initial film thickness (at initial stages), so a "long-wave approximation" [17, 123] is used to simplify the governing equations. The polymer film (lower layer) is assumed to be more viscous compared to its bounding layer ($\mu_2/\mu_1 \ll 1$). Hence, the dynamic of upper layer is decoupled from thin film which reduces the computational effort in tracking interface height. Applying these assumptions to the governing equations and the aforementioned boundary conditions result in the following "thin film" equation [17] in the long-wave limit form:

$$\begin{split} 3\mu h_t + \left\{h^3[\gamma(h_{xx} + h_{yy}) - \phi]_x - h^2(\phi_T)_x\right\}_x \\ + \left\{h^3[\gamma(h_{xx} + h_{yy}) - \phi]_y - h^2(\phi_T)_y\right\}_y = 0 \end{split} \tag{3.5}$$

In eqn. 3.5, the term $3\mu h_t$, accounts for the viscous damping force and the term $\gamma(h_{xx} + h_{yy})$ stands for the surface tension force which also damps the fluctuations by minimizing the interface area of the film leading to minimum free energy of system [32].

3.1.2 Interaction potentials

Conjoining pressure, ϕ, (force acting on the film interface per unit area) is defined as the gradient of excess intermolecular interactions, $\phi = \nabla(\triangle G)$. In EHD, the electric field induces a pressure at the film interface which is added to the natural interactions to generate excess intermolecular interactions. The conjoining pressure, ϕ, is a summation of these interaction potentials: van der Waals, electrostatic and Born repulsive interaction potentials and is given as:

$$\phi = \phi_{vdW} + \phi_{Br} + \phi_{EL} \tag{3.6}$$

The van der Waals interaction is the summation of Keeson, Debye and London dispersion forces [32, 33]. This interaction is defined as $\phi_{vdW_L} = A_L/6\pi h^3$ and $\phi_{vdW_U} = -A_U/6\pi(d-h)^3$ for the lower and upper electrodes, respectively. A_L and A_U are effective *Hamaker* constants for the electrodes which depend on the materials used for electrodes and fluid layers [32, 33]. For instance, for three layered systems it is defined: $A_{213} = (\sqrt{A_{33}} - \sqrt{A_{11}})(\sqrt{A_{22}} - \sqrt{A_{11}})$ in which 1,2 and 3 denote substrate, liquid film and bounding fluid.

The van der Waals interaction are singular as $h \to 0$ and $h \to d$. To avoid nonphysical penetration of liquid to solid phase, in case of film rupture and touching, a cutoff distance, l_0, is defined for which a short range repulsive force, called Born repulsion, acts on the film interface [22, 31, 82, 93]. This is used to maintain a minimum equilibrium liquid thickness on both electrodes and is defined as $\phi_{Br_L} = -8B_L/h^9$ and $\phi_{Br_U} = 8B_U/(d-h)^9$ for the lower and upper electrodes, respectively. Coefficients, B_L and B_U are found by setting the net conjoining pressure equal to zero at $h = l_0$ and $h = d - l_0$ for lower and upper surfaces.

The most significant component of the conjoining pressure is the electrostatic pressure developed due to Maxwell stress [79],

$$\phi_{EL} = \frac{1}{2}\varepsilon_0[\varepsilon_1(\frac{\partial \psi_1}{\partial z}|_{z=h})^2 - \varepsilon_2(\frac{\partial \psi_2}{\partial z}|_{z=h})^2] \tag{3.7}$$

where ε_1 (ε_2) is the relative electric permittivity of lower (top) layer and ε_0 is free space electric permittivity and ψ is the electric potential.

3.1.3 Electrostatic models

To solve the thin film dynamics it is necessary to have an electrostatic model which describes the electric potential distribution within layers to ϕ_{EL} acting on the interface. The polymer film is typically assumed to behave like a PD or LD. However, assuming the very large and small electric diffuse layer inherent in the PD and LD models are not valid for the nanofilms as the formed diffuse layer (even small) is comparable with the film thickness over the evolution process. In IL films, it is assumed that the diffuse layer has comparable thickness to the film thickness. The electrostatic model will be developed for different cases of PD-PD, PD-IL and IL-PD systems.

Throughout this study, it is assumed that electric breakdown does not occur during the EHD patterning process. Using electrolytes, a particular case of ILs, free ions have the ability to migrate or redistribute within the liquid and accumulate on the charged surfaces forming a DL. More details about DL and its regions are presented in literature[129, 130]. The ion conservation equation for the dynamic of free ions in the electrolytes, based on the number concentration of the free monovalent ions (n_+ and n_-), is:

$$\frac{\partial n_\pm}{\partial t} = -\nabla.(\mp e m_\pm n_\pm \nabla\psi - m_\pm k_B T \nabla n_\pm) + R_\pm \tag{3.8}$$

The left hand side of this equation represents the accumulation rate. The first term on the right hand side is the net flux due to migration and diffusion, respectively. Ions migration is induced by electric potential gradient, $\nabla\psi$ and the diffusion is the result of concentration gradient $\nabla n_\pm$. The last term, $R_\pm$ is the production rate of species due to chemical reactions which is set to zero in this study. $m_\pm$ is the mobility and $e = 1.602 \times 10^{-19}$ (C) is the elementary charge. The Boltzmann constant, $k_B = 1.3806488 \times 10^{-23}$ (m^2kg/s^2K) and T (K) is temperature. Using definitions for free charge density $\rho_f = e(n_+ - n_-)$, conductivity $\sigma = e(m_+n_+ + m_-n_-)$ and mobility $m = D/k_BT$ (D is diffusion coefficient), the ion conservation equation is:

$$\frac{\partial \rho_f}{\partial t} = -\nabla.(\sigma\nabla\psi - D\nabla\rho_f) \tag{3.9}$$

This equation is then scaled using nondimensional terms ($\rho_f^* = \frac{\rho_f}{\epsilon_0\psi_0/h_0^2}$, $\psi^* = \frac{\psi}{\psi_0}$, $l^* = \frac{l}{h_0}$ and $t^* = \frac{\epsilon_0\psi_0^2}{\mu h_0^2}t$) resulting in:

$$\frac{\tau_c}{\tau_p}\frac{\partial \rho_f^*}{\partial t^*} = -\nabla.\left(\nabla\psi^* - (\epsilon_0 D/\sigma h_0^2)\nabla\rho_f^*\right) \tag{3.10}$$

where, $\tau_p = \mu h_0/\epsilon_0\epsilon_1\psi_0^2$ is the process time and $\tau_c = \epsilon_0\epsilon_1/\sigma$ is the charge relaxation time [97]. In this study based on the parameters used for simulations, τ_p and τ_c vary between $2.35 - 5.85$ (s) and $8.92\times10^{-11} - 1.05\times10^{-7}$ (s), respectively. When the process time is much larger than the charge relaxation time ($\tau_p \gg \tau_c$), the dynamics of free ions (charges) becomes insignificant [99, 116] and left-hand side of eqns. 3.9 and 3.10 becomes zero. In that case the ion conservation equation (eqn. 3.9) can be simplified to the Poisson equation

[33].

$$\nabla^2\psi = -\frac{\rho_f}{\epsilon\epsilon_0} \tag{3.11}$$

where,

$$\rho_f = 2en_\infty \sinh\left(\frac{e}{k_BT}(\psi - \psi_{ref})\right) \tag{3.12}$$

and n_∞ and ψ_{ref} are bulk ion number concentration and reference potential, respectively. When the bounding media is air or any PD media, $\rho_f = 0$, eqn. 3.11 reduces to Laplace equation. Bulk ion number concentration depends on the molarity of electrolyte which is defined as $n_\infty = 1000N_AM$ where M is the electrolyte molar concentration (mol/L) and $N_A = 6.022 \times 10^{23} mol^{-1}$ is Avogadro number. In eqn. 3.12 the term k_BT represents thermal motion while the term $e(\psi - \psi_{ref})$ is the electrostatic contribution caused by the deviation from electroneutrality condition (ψ_{ref}), respectively. The electrostatics governing equations in the long-wave limit [17] for PD layer is

$$\frac{d^2\psi}{dz^2} = 0 \tag{3.13}$$

and for IL layer are

$$\frac{d^2\psi}{dz^2} = \frac{2en_\infty}{\epsilon\epsilon_0} \sinh\left(\frac{e}{K_BT}(\psi_1 - \psi_{ref})\right) \tag{3.14a}$$

$$\int_0^h \rho_f dz = \int_0^h \sinh\left(\frac{e}{K_BT}(\psi - \psi_{ref})\right) dz = 0 \tag{3.14b}$$

Eqn. 3.14b represents conservation of ions within the IL film and is used to find the reference potential, ψ_{ref}. The boundary conditions for eqns. 3.13, 3.14a and 3.14b are the applied potential or grounded on the electrodes and the electric potential and displacement continuity ($\psi_1 = \psi_2$ and $\varepsilon_1 \frac{\partial \psi_1}{\partial z} = \varepsilon_2 \frac{\partial \psi_2}{\partial z}$) at the interface.

PD film bounded with PD layer:

The derivation of the PD-PD systems is well known and Laplace equation governs the electric potential distributions within the layers and resulting electrostatic pressure is given by, [82]:

$$\phi_{EL} = -\frac{1}{2}\varepsilon_1\varepsilon_0(\frac{\varepsilon_1}{\varepsilon_2} - 1)[\frac{\psi_{up}}{h(1 - \frac{\varepsilon_1}{\varepsilon_2}) + \frac{\varepsilon_1}{\varepsilon_2}d}]^2 \tag{3.15}$$

where, ψ_{up} is the applied potential to the upper electrode.

IL film bounded with PD layer:

In this study, first, the Debye Hückel approximation [33, 116] is used to linearize the Poisson equation transforming eqns. 3.14a and 3.14b to:

$$\frac{d^2\psi_1}{dz^2} = \kappa^2(\psi_1 - \psi_{ref}) \tag{3.16a}$$

$$\int_0^h \rho_f dz = \int_0^h (\psi_1 - \psi_{ref}) dz = 0 \tag{3.16b}$$

where $\kappa = (\frac{2000\, e^2 N_A M}{\varepsilon_1 \varepsilon_0 k_B T})^{1/2}$ is the inverse of Debye length. Solving eqns. 3.13, 3.16a and 3.16b results in the electric potential distribution within PD and IL layers as follow:

$$\psi_2 = \left(\frac{z-d}{h-d}\right)\psi_s \tag{3.17}$$

$$\psi_1 = (\psi_s - \psi_l)\left[\frac{\cosh(\kappa h) + 1}{2\sinh(\kappa h)}\right]\sinh(\kappa z) \\ -(\frac{\psi_s - \psi_l}{2})\cosh(\kappa z) + \frac{\psi_s + \psi_l}{2} \tag{3.18}$$

where, ψ_s is the interface potential and is determined by the following equation:

$$\psi_s = \frac{\psi_l(1 + \cosh(\kappa h))}{1 + \cosh(\kappa h) + \frac{2\varepsilon_2}{\varepsilon_1 \kappa (d-h)} \sinh(\kappa h)} \tag{3.19}$$

In ionic liquids, an additional force exists between charged surfaces (film interface and lower electrode) due to overlapping of DLs, called the osmotic force and defined as $F_{os} = -dP_{os}/dz$ [33, 131]. The osmotic pressure, P_{os} has a hydrostatic origin and can be found from the momentum balance in transverse direction (z). At equilibrium, and assuming that the radii of curvature of the interface is small compared with the IL film thickness ($\kappa^{\star} h \ll 1$), this force is balanced with electrostatic force, $F_E = -\rho_{(z)}(d\psi/dz)$, which results in [132]:

$$P_{os} - \frac{1}{2}\varepsilon_1\varepsilon_0(\frac{d\psi_1}{dz})^2 = P_c = constant \tag{3.20}$$

Thus at a given IL film thickness there is always a constant difference between osmotic pressure and electrostatic pressure in eqn. 3.20. The term P_c can be found from a stress balance at film interface [116]. Substituting ψ_1 and ψ_2 from eqns. 3.17 and 3.18 into eqn. 3.7 then using relation for ψ_s in eqn. 3.19 results in the following electrostatic pressure for a PD-IL system,

$$\phi_{EL} = \frac{1}{2}\varepsilon_2\varepsilon_0(\frac{\varepsilon_2}{\varepsilon_1} - 1)[\frac{\psi_s}{d-h}]^2 \tag{3.21}$$

PD film bounded with IL layer:

For the case of PD film bounded with IL layer, the complex case of nonlinear Poission-Boltzmann equation (eqn. 3.14a) is considered for the IL layer. To analytically solve the governing equations, the nondimensional electric potential and length are defined as: $\Psi = e\bar{z}\psi/k_BT$ and $Z = z/(d-h)$, respectively. The nondimensional Laplace and nonlinear Poisson-Boltzmann equations in the long wave limit are:

$$\frac{d^2\Psi_1}{dZ^2} = 0 \tag{3.22}$$

$$\frac{d^2\Psi_2}{dZ^2} = (\kappa(d-h))^2 \sinh(\Psi_i - \Psi_{ref}) \tag{3.23}$$

The boundary conditions are: the applied potential on the upper electrode, grounded for the lower electrode. These are solved to find electric potential distribution across the PD layer, $0 \leq Z \leq \frac{h}{d-h}$

$$\Psi_1 = (\frac{d-h}{h})\Psi_s Z \tag{3.24}$$

and the IL layer, $\frac{h}{d-h} \leq Z \leq \frac{d}{d-h}$

$$\Psi_2 = \Psi_{up} + 2Ln[\frac{1 - exp(\kappa(d-h)(\frac{h}{(d-h)} - Z))\ tanh\{\frac{(\Psi_{up}-\Psi_s)}{4}\}}{1 + exp(\kappa(d-h)(\frac{h}{(d-h)} - Z))\ tanh\{\frac{(\Psi_{up}-\Psi_s)}{4}\}}] \tag{3.25}$$

where $\kappa = (\frac{\varepsilon_2\varepsilon_0 k_BT}{2e^2z^2n_\infty})^{1/2}$ is the inverse of Debye length [33]. The nondimensional interface electric potential, Ψ_s, can be found by solving the following nonlinear equation,

$$\Psi_s - \frac{2\varepsilon_2\kappa h}{\varepsilon_1}\sinh(\frac{(\Psi_{up} - \Psi_s)}{2}) = 0 \tag{3.26}$$

Using the electric potential distribution obtained from eqs (3.24) and (3.25) and combining with the electrostatic pressure in eqn. 3.7 results in a conjoining pressure acting on the IL-PD bilayer interface of:

$$\phi_{EL} = -\frac{1}{2}\varepsilon_1\varepsilon_0(\frac{\varepsilon_1}{\varepsilon_2} - 1)(\frac{\psi_s}{h})^2 \tag{3.27}$$

3.1.4 Thermocapillary

Heating the thin liquid film results in an interfacial tension gradient along the interface. The thermocapillary effect is included in “thin film” equation using an extra term of ϕ_T. To find the thermocapillary term, first the temperature distribution in each layer is found for two cases of thermal conduction and convection boundary condition at the interface. For the case of thermal conduction in the thin film and the bounding layer as a dominant mode of heat transfer, the temperature distribution is given by,

$$T_1 = T_H - [\frac{\Delta T}{h - k_r(h-d)}]z \quad at \quad 0 \leqslant z \leqslant h \tag{3.28}$$

$$T_2 = T_C + [\frac{\Delta T k_r}{h - k_r(h-d)}](d-z) \quad at \quad h \leqslant z \leqslant d \tag{3.29}$$

and resulting thermal pressure as,

$$\phi_T = \frac{3\alpha\Delta T}{2}\left[\frac{k_r d}{(1-k_r)[h(1-k_r)+k_r d]}\right] \tag{3.30}$$

Where, $k_r = k_1/k_2$ is the relative thermal conductivity of layers and temperature difference is $\Delta T = T_H - T_C$. For the case of thermal convection as a boundary condition at the interface, Newtons law of cooling is applied and the bounding layer is assumed to be a thermal reservoir at temperature T_C. The temperature distribution in the film is found as,

$$T_1 = T_H - [\frac{(\frac{h_c}{k_1})\Delta T}{1+(\frac{h_c}{k_1})h}]z \quad at \quad 0 \leqslant z \leqslant h \tag{3.31}$$

$$T_2 = T_C \quad at \quad h \leqslant z \leqslant d \tag{3.32}$$

and resulting thermal pressure as,

$$\phi_T = \frac{3\alpha\Delta T}{2}\left[\frac{1}{1+(\frac{h_c}{k_1})h}\right] \tag{3.33}$$

However, the convective mode of heat transfer between film interface and the bounding layer is negligible (Biot number, $Bi = \frac{h_c h}{k_1} \ll 0.1$) as the film thickness in the EHD pattering process is in micron and submicron ranges. So it is neglected.

Finally, the developed electrostatic pressure (eqn. 3.21) and thermocapillary pressure term (eqn. 3.31) along with van der Waals, ϕ_{vdW} and Born repulsion, ϕ_{Br} pressures are substituted into the thin film equation (eqn. 3.5) to find the dynamics and spatiotemporal evolution of a thin IL film subjected to a transverse electric field and/or thermal gradient.

3.1.5 Linear stability analysis

Initially, the investigation of nanofilm dynamics uses LS analysis. This analytical technique is used to predict the characteristic wavelength for growth of instabilities. In EHD patterning process it is shown that the center to center distance of pillars (raised columnar structure) are characterized with λ_{max} resulting from LS analysis [23]. The interface height, h, in eqn. 3.5 is replaced with a small sinusoidal perturbation of the interface about its initial value, $h = h_0 + \epsilon \exp(\kappa^*(x+y)i + st)$. In this relation, κ^* is the wave number, s is the growth coefficient and ϵ is the small amplitude of sinusoidal perturbation. After substituting h in eqn. 3.5 with this relation and eliminating the nonlinear terms, the following dispersion relation is found:

$$s = -\frac{{h_0}^2 {\kappa^*}^2}{\mu}\left[\frac{h_0\gamma}{3}{\kappa^*}^2 + \frac{h_0}{3}\frac{\partial\phi_{EL}}{\partial h}|_{h_0} + \frac{\partial\phi_T}{\partial h}|_{h_0}\right] \tag{3.34}$$

Over time, the perturbations are amplified if $s > 0$. Since both $\frac{\partial\phi_{EL}}{\partial h} < 0$ and $\frac{\partial\phi_T}{\partial h} < 0$, all modes with $\kappa^* < {\kappa^*}_c$ are unstable.

$${\kappa^*}_c = \sqrt{\frac{\frac{h_0}{3}\frac{\partial\phi_{EL}}{\partial h}|_{h_0} + \frac{\partial\phi_T}{\partial h}|_{h_0}}{-\frac{h_0\gamma}{3}}}$$

The dominant wave number, ${\kappa^*}_{max}$, corresponding to the fastest growing wave will eventually dominate and is given by:

$${\kappa^*}_{max} = \sqrt{\frac{\frac{h_0}{3}\frac{\partial\phi_{EL}}{\partial h}|_{h_0} + \frac{\partial\phi_T}{\partial h}|_{h_0}}{\frac{-2h_0\gamma}{3}}} \tag{3.35}$$

The maximum wavelength for growth of instabilities is defined as $\lambda_{max} = 2\pi/{\kappa^*}_{max}$. In the case of isothermal liquid film the term, $\frac{\partial\phi_T}{\partial h}|_{h_0}$, cancels out in κ_{max} relation [23, 82]. The lateral size of patterning (center to center distance of pillars) is analytically predicted by the maximum wavelength of λ_{max} using LS analysis.

3.1.6 Scaling of thin film equation

To find the dynamics and morphology of interface, the thin film equation is first nondimensionalized using following scaling factors:

$$\begin{aligned} L_s &= (\gamma\epsilon_2^2 h_0^3/0.5\epsilon_0\epsilon_1(\epsilon_1-\epsilon_2){\psi_{up}}^2)^{\frac{1}{2}} \\ T_s &= 3\mu\gamma\epsilon_2^2 h_0^3/[0.5\epsilon_0\epsilon_1(\epsilon_1-\epsilon_2){\psi_{up}}^2] \\ \Phi_s &= 0.5\epsilon_0\epsilon_1(\epsilon_1-\epsilon_2){\psi_{up}}^2/(\epsilon_2^2 h_0^2) \end{aligned} \tag{3.36}$$

where, L_s is used for spatial coordinates ($X = x/L_s, Y = y/L_s$), T_s for time ($T = t/T_s$) and Φ_S for conjoining pressure ($\Phi = \phi/\Phi_s$). In order to compare the results at the same physical domain, the length and time scaling factors are chosen based on isothermal EHD case and kept constant unless otherwise indicated. The interface height is scaled with the initial mean film thickness ($H = h/h_0$). The resulting nondimensionalized thin film equation is:

$$\begin{aligned} &H_T + [H^3([H_{XX} + H_{YY}] - \Phi)_X - H^2(\Phi_T)_X]_X \\ &\qquad + [H^3([H_{XX} + H_{YY}] - \Phi)_Y - H^2(\Phi_T)_Y]_Y = 0 \end{aligned} \tag{3.37}$$

where term Φ_T is given by,

$$\Phi_T = \frac{\bar{M} k_r d}{(1 - k_r)[h(1 - k_r) + k_r d]} \tag{3.38}$$

In the scaled form of thermal pressure, Φ_T, term $\bar{M} = \frac{3\alpha\nabla T}{2h_0\Phi_s}$ is called modified Marangoni number which is the ratio of the interfacial force gradient to electrostatic force. With no applied electric field ($\psi_{up} = 0$), the van der Waals forces and thermocapillary forces are dominant in isothermal and heated nanofilms, respectively. The following scalings based on the LS analysis (details found in [122, 123]) for the base-case are used,

$$\begin{aligned} L_s &= {h_0}^2/(2\pi\gamma/A_L)^{\frac{1}{2}} \\ T_s &= {A_L}^2/(12\pi^2\mu\gamma {h_0}^5) \\ \Phi_s &= 2\pi {h_0}^3/A_L \end{aligned} \tag{3.39}$$

The nondimensionalized thin film equation (eqn. 3.37) is solved numerically to find the spatiotemporal behavior of heated thin liquid film interface under the application of a transverse electric field. Details of the numerical method is presented next.

3.2 Numerical modeling

To obtain transient behavior of liquid-liquid interface, the thin film equation (eqn. 3.5) is scaled using scaling factors in (3.36) and (3.39) and solved numerically.

$$\begin{aligned} &H_T + \left\{H^3[\gamma(H_{XX} + H_{YY}) - \Phi]_X - H^2(\Phi_T)_X\right\}_X \\ &\qquad + \left\{H^3[\gamma(H_{XX} + H_{YY}) - \Phi]_Y - H^2(\Phi_T)_Y\right\}_Y = 0 \end{aligned} \tag{3.40}$$

Thin film equation (eqn. 3.40) is an 4^{th} order nonlinear partial differential equation (PDE). First, spatial derivatives are discretized using finite difference to convert the PDE to a differential algebraic equation (DAE) in time. Differential algebraic solver (DASSL) with an adaptive time stepping is then used for the DAE system [133]. In following subsections the details regarding the numerical modeling and solution are described[134]. In all the simulation, a domain with length of $L > \lambda_{max}$ (obtained from LS analysis) or larger is chosen and it is sufficient to see the growth of instabilities when periodic boundary conditions are chosen, otherwise fluctuations will damp out over the time [31].

3.2.1 Finite difference

The general form of thin film equation is given in eqn. 3.37 which includes derivatives with respect to X and Y. Here, the discretization of X derivatives will be explained while for the Y direction the same terminology will be used.

$$\frac{\partial}{\partial X}\left[H^3\frac{\partial}{\partial X}\left\{\frac{\partial^2 H}{\partial X^2}+\frac{\partial^2 H}{\partial Y^2}-\Phi\right\}-H^2\frac{\partial}{\partial X}\left\{\Phi_T\right\}\right]=\frac{\partial}{\partial X}\left[\Pi\right] \tag{3.41}$$

Central difference is used for the outer most derivative which results in:

$$\frac{\partial}{\partial X}\left[\Pi\right]_{(i,j)}\simeq\frac{1}{2\Delta}\left[\left(\Pi\right)_{(i+1,j)}-\left(\Pi\right)_{(i-1,j)}\right]+O(\Delta^2) \tag{3.42}$$

where $\Delta = X_{(i+1,j)} - X_{(i,j)}$ is the spacing between grid points in the uniform Cartesian discretization.

$$\begin{aligned}\left(\Pi\right)_{(i+1,j)} &= {H_{(i+1,j)}}^3\left(\frac{\partial}{\partial X}\Psi\right)_{(i+1,j)}-{H_{(i+1,j)}}^2\left(\frac{\partial}{\partial X}\Phi_T\right)_{(i+1,j)}\\ \left(\Pi\right)_{(i-1,j)} &= {H_{(i-1,j)}}^3\left(\frac{\partial}{\partial X}\Psi\right)_{(i-1,j)}-{H_{(i-1,j)}}^2\left(\frac{\partial}{\partial X}\Phi_T\right)_{(i-1,j)}\end{aligned} \tag{3.43}$$

Where

$$\Psi=\frac{\partial^2 H}{\partial X^2}+\frac{\partial^2 H}{\partial Y^2}-\Phi$$

is defined to simplify the notations. For the next derivative, the backward difference is used:

$$\begin{aligned}
\Big(\frac{\partial}{\partial X}\Psi\Big)_{(i+1,j)} &\simeq \frac{1}{\Delta}\Big(\Psi_{(i+1,j)} - \Psi_{(i,j)}\Big)\\
\Big(\frac{\partial}{\partial X}\Psi\Big)_{(i-1,j)} &\simeq \frac{1}{\Delta}\Big(\Psi_{(i-1,j)} - \Psi_{(i-2,j)}\Big)\\
\Big(\frac{\partial}{\partial X}\Phi_T\Big)_{(i+1,j)} &\simeq \frac{1}{\Delta}\Big(\Phi_{T(i+1,j)} - \Phi_{T(i,j)}\Big)\\
\Big(\frac{\partial}{\partial X}\Phi_T\Big)_{(i-1,j)} &\simeq \frac{1}{\Delta}\Big(\Phi_{T(i-1,j)} - \Phi_{T(i-2,j)}\Big)
\end{aligned} \tag{3.44}$$

Substituting the definitions in 3.44 into 3.42 results in:

$$\begin{aligned}
&\frac{\partial}{\partial X}\Big[\Pi\Big]_{(i,j)} \simeq\\
&\qquad \frac{1}{2\Delta}\Bigg[{H_{(i+1,j)}}^3\frac{1}{\Delta}\Big(\Psi_{(i+1,j)} - \Psi_{(i,j)}\Big) - {H_{(i+1,j)}}^2\frac{1}{\Delta}\Big(\Phi_{T(i+1,j)} - \Phi_{T(i,j)}\Big)\\
&\quad -{H_{(i-1,j)}}^3\frac{1}{\Delta}\Big(\Psi_{(i-1,j)} - \Psi_{(i-2,j)}\Big) + {H_{(i-1,j)}}^2\frac{1}{\Delta}\Big(\Phi_{T(i-1,j)} - \Phi_{T(i-2,j)}\Big)\Bigg]
\end{aligned} \tag{3.45}$$

For the second derivatives ($\frac{\partial^2 H}{\partial X^2}$ and $\frac{\partial^2 H}{\partial Y^2}$) presented using Ψ, a three points central difference is used as:

$$\begin{aligned}
\Psi_{(i,j)} &\simeq \frac{1}{\Delta^2}\Bigg[H_{(i+1,j)} + H_{(i-1,j)} + H_{(i,j+1)} + H_{(i,j-1)} - 4H_{(i,j)}\Bigg] - \Phi_{(i,j)}\\
\Psi_{(i+1,j)} &\simeq \frac{1}{\Delta^2}\Big[H_{(i+2,j)} + H_{(i,j)} + H_{(i+1,j+1)} + H_{(i+1,j-1)} - 4H_{(i+1,j)}\Big] - \Phi_{(i+1,j)}\\
\Psi_{(i-1,j)} &\simeq \frac{1}{\Delta^2}\Big[H_{(i,j)} + H_{(i-2,j)} + H_{(i-1,j+1)} + H_{(i-1,j-1)} - 4H_{(i-1,j)}\Big] - \Phi_{(i-1,j)}\\
\Psi_{(i-2,j)} &\simeq \frac{1}{\Delta^2}\Big[H_{(i-1,j)} + H_{(i-3,j)} + H_{(i-2,j+1)} + H_{(i-2,j-1)} - 4H_{(i-2,j)}\Big] - \Phi_{(i-2,j)}
\end{aligned} \tag{3.46}$$

the final form of the derivatives of the X component can be found by substituting the eqn. 3.46 into eqn. 3.45. The same approach is used for the spatial derivatives in the Y direction.

Boundary condition

In all problems considered in this work, periodic boundary conditions were applied. The periodic boundary means that the same outflow at one boundary enters to the domain from the opposite side of the domain.

Therefore, the grid points value are defined as:

$$\text{for the left boundary, i=1:} \quad H(i-1,j) = H(N-1,j) \tag{3.47}$$

$$\text{for the right boundary, i=N:} \quad H(i+1,j) = H(2,j) \tag{3.48}$$

Using above definition, the second derivatives in X direction can be written as:

$$\left[\frac{\partial^2 H}{\partial X^2}\right]_{(1,j)} \simeq \frac{1}{\Delta^2}\left[H_{(2,j)} + H_{(N-1,j)} - 2H_{(1,j)}\right] \tag{3.49}$$

3.2.2 Differential algebraic solver

Applying the FD discretization to the spatial derivatives results in a system of ordinary differential equations (ODE) with time which has the following form:

$$F(t, y, y^{'}) = 0 \tag{3.50}$$

where F, y and $y^{'}$ are N dimensional vectors. This ODE (eqn. 3.50) is called differential algebraic equation (DAE) because it can not be rewritten in the standard form of

$$y^{'} = f(t, y), \qquad y(t_0) = y_0 \tag{3.51}$$

which can be solved with most of the common ODE solvers. This is due to singular or non- invertible Jacobian matrix ($\frac{\partial F}{\partial y^{'}}$) of the eqn. 3.50 [135]. In order to solve the resulting sets of time differential algebraic equations (DAE), an adaptive time step ODE solver of DASSL (in SLATEC library [136]) is employed [133, 135, 137, 138] with consistent set of initial conditions $y(t_0) = y_0$ and $y^{'}(t_0) = {y_0}^{'}$.

There have been other numerical methods, like Gear's method [139, 140], which was developed before DASSL to solve DAEs which used stiff ordinary differential systems techniques. Subsequently other techniques such as LSODI [141] which can solve the linear implicit DAE systems in the form of $A(t, y)y^{'} = f(t, y)$ have been developed. In the Gear's method, the derivative ($y^{'}$) in eqn. 3.50 is replaced by a difference approximation. Then at the current time, t_n the resulting equation was solved using Newtons's method. However, in the DASSL algorithm (as an extension of this method), the derivative ,$y^{'}$ is replaced by higher order (i.e k^{th} order ranging from one to five) backward difference formula (BDF). DASSL accepts the fixed time steps as an input whereas it chooses the interval time stepsize and order of k based on the solution's behavior so it is called addaptive time step solver. More details regarding the solution procedure in DASSL can be found in Appendix A-1.

The general numeric algorithm used to solve thin film equation can be seen in figure 3.3. All constants and parameters are loaded using an external data file. Based on the specified number of grid points, the grid points spacing is calculated. The film initial thickness is initialized using random perturbation about the predetermined mean thickness value. It is assumed that the solution is converged if the linear norm is less than a threshold value Γ over a given time interval.

$$Norm(H) = \sum_{j=1}^{N_x \times N_y} (H_j|_T - H_j|_{T+\Delta t}) \tag{3.52}$$

This threshold value for convergence was found by examining multiple test cases and depending on the case considered it ranges from 1×10^{-7} to 1×10^{-11}. These values capture the film dynamics while minimizing simulation run time.

In order to use DASSL solver, the Jacobian should be calculated separately which requires all the discretized spatial derivatives and forces. At each time step DASSL provides the solution; H, H' and the last successive time step which DASSL solver has used to converge in *RWORK(7)*. In this work, to improve the proficiency of the algorithm and to reduce the computing time and cost, this value is used as the time step, ΔT in the time loop. Since the thin film equation is a nonlinear PDE and requires different time steps depending on the stage of thin film evolution, using adaptive time step makes the algorithm very computationally efficient.

The code is designed to have multiple checks to avoid unnecessary iterations. Predefined end time in the time loop, iteration limit and norm value for H are three checks which are used to control the solution procedure. If any of these conditions is met, the loop will stop and the solution results will be saved in output files. However, the main criteria for the convergence is reaching to the norm limit, Γ. The code has been ran on Linux using gfortran and Windows using Watcom compilers.

Initial condition

Initial conditions for the simulation are a random disturbance while maintaining liquid film volume. To generate a random number in windows machine, *URAND* command is used and for the Linux machine, *RAND* command is used.

3.2.3 Domain Size and Meshing

To examine the optimum grid size, four different uniform Cartesian grid sizes ($N_x \times N_y$) ranging from 91×91 to 171×171 are employed and the results for the maximum nondimensional interface height growth over nondimensional time are shown in figure 3.4. Another evaluation factor of, "$\Delta H_{mean}\ error$" is defined

$$\Delta H_{mean}\ error\ (\%) = \sum_{j=1}^{N_x \times N_y} \left(\frac{H_j|_{T_f} - H_j|_{T_i}}{H_j|_{T_i}} \right) \times 100$$

and compared for all four cases to ensure satisfaction of the volume conservation. Consequently, 121×121 grid points was found to be the acceptable grid size compromising between computational cost and accurate film interface (H) tracking.

3.2.4 Numerical model validation

Nondimensional film thickness as a function of time shows how the initial disturbances grow during the early stages of pattern formation. A sequence of times (t^*) are shown in figure 3.5 to show the different stages in the dewetting process of an initially unstable film with no applied electric field. The initial random disturbance is reorganized into nonuniform holes (see figure 3.5 (i)) then holes and their surrounding uneven rims are expanded over time (see figure 3.5 (ii)) leading to holes coalescence and bicontinuous structure formation (see figure 3.5 (iii)). Next, long undulating (peak and valley) shape structures form due to coalescence of holes and undergo some fragmentation and create droplets (see figure 3.5 (iv-v)). The size of droplets increases over time (see figure 3.5 (vi)) due to negative diffusion-fluid flow from thinner region to the thicker region. Finally droplets coalesce to minimize the interface area and form one droplet in the final equilibrium condition (image is not shown). These predictions from the presented numerical scheme matches with results presented in literature regarding the pattern formation in unstable thin liquid films [54]. Effect of the viscous force and van der Waals forces on the dewetting process and the film drainage time is also investigated which are not presented here. For more information see Appendix B-1.

In this section, results obtained from numerical simulation are compared to experimental observation [68] to demonstrate the fidelity and accuracy of simulation results in prediction of the EIP process. An upper electrode with a square shape (width of $\sim$12 μm) protrusion seprated with trenches (width of $\sim$1.2 μm) is chosen to reproduce the results in [68]. A 3-D and 2-D snapshots of the film structures and cross-section height profile of the interface are shown in figure 3.6 with details in the figure caption. As expected from experiments (figure 5 in Ref.[68]), 2×2 arrays of pillars with identical height formed under the protrusions (figure 3.6 (a and b)). The intra-array spacing of $\lambda_1 \sim 6.2$ μm and $\lambda_2 \sim 8.8$ μm are reported from experiments which are in good agreement with the current numerical simulation results of $\lambda_1 \sim 5.9$ μm and $\lambda_2 \sim 8.3$ μm (figure 3.6 (c)).

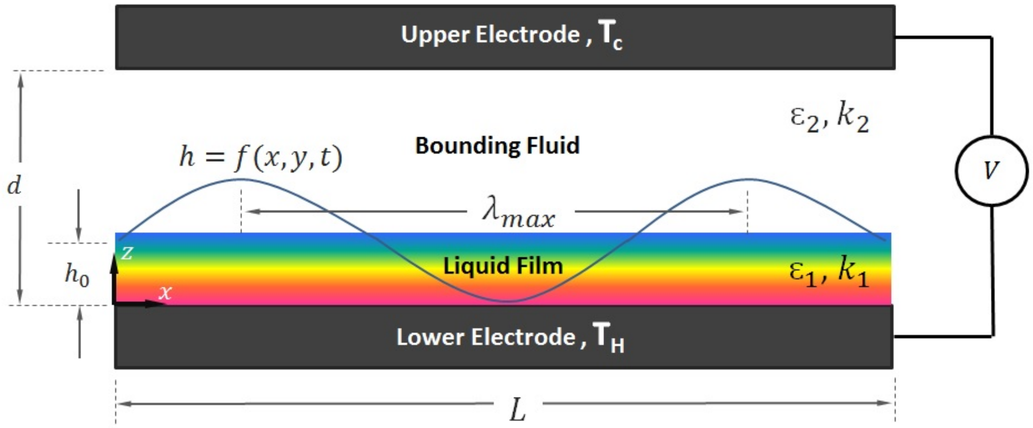

Figure 3.1: Schematic view of the thin film sandwiched between electrodes. Electric field and thermal gradient is applied in transverse direction. The z-position of the free interface is described by the function $h = f(x, y, t)$ with the lateral coordinates x, y and time t. The amplitude of the fluctuation with wavelength is not to scale and is magnified. d=100 nm

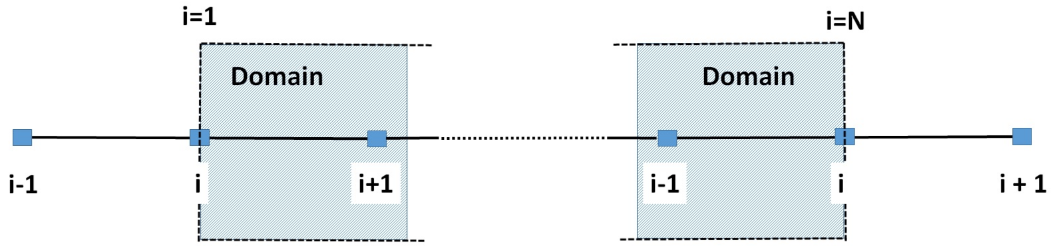

Figure 3.2: Uniform Cartesian grid points in X direction

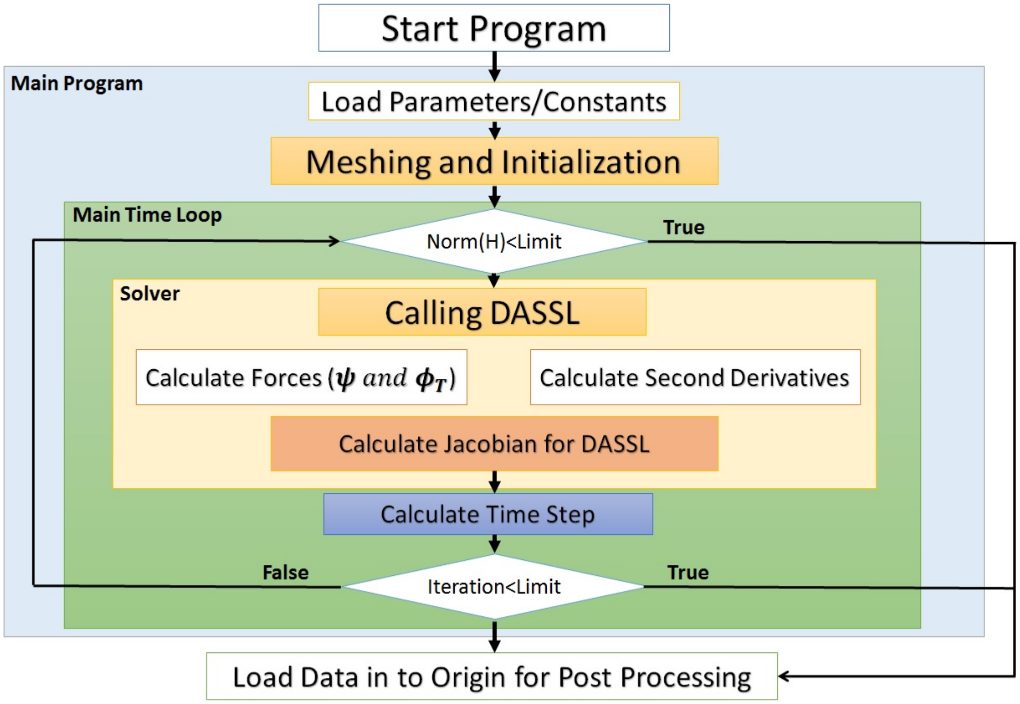

Figure 3.3: Numeric algorithm used to solve the thin film equation

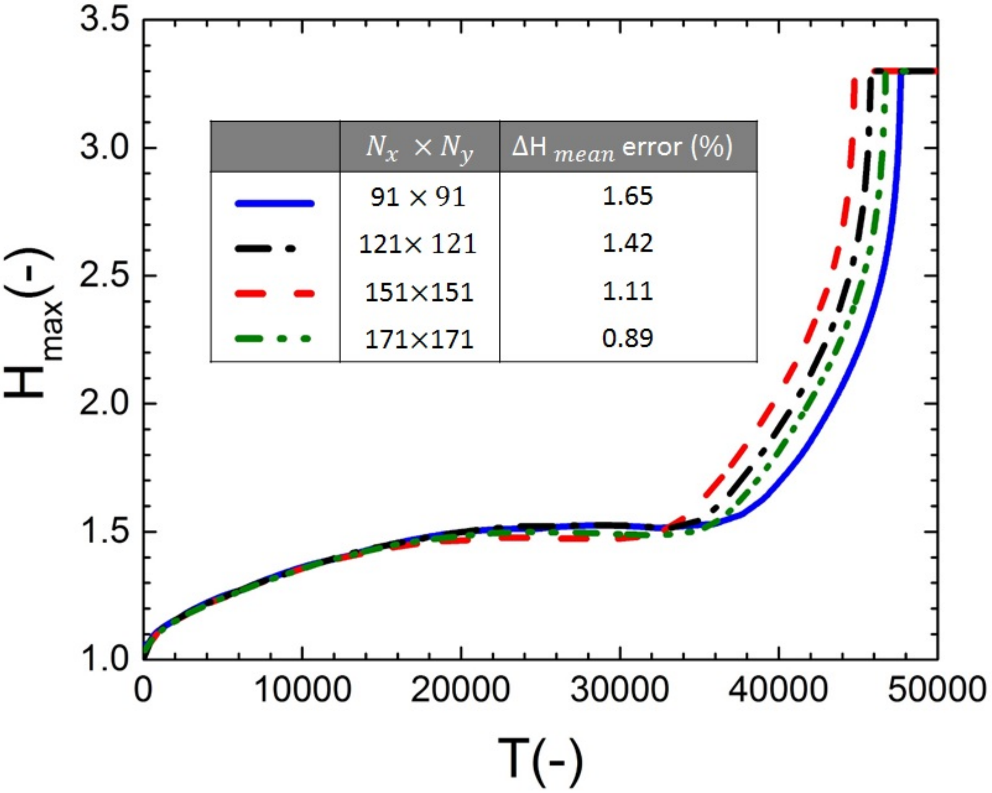

Figure 3.4: Effect of grid sizes on transient growth of interface height. $h_0 = 30$ nm, $V = 20\,V$.

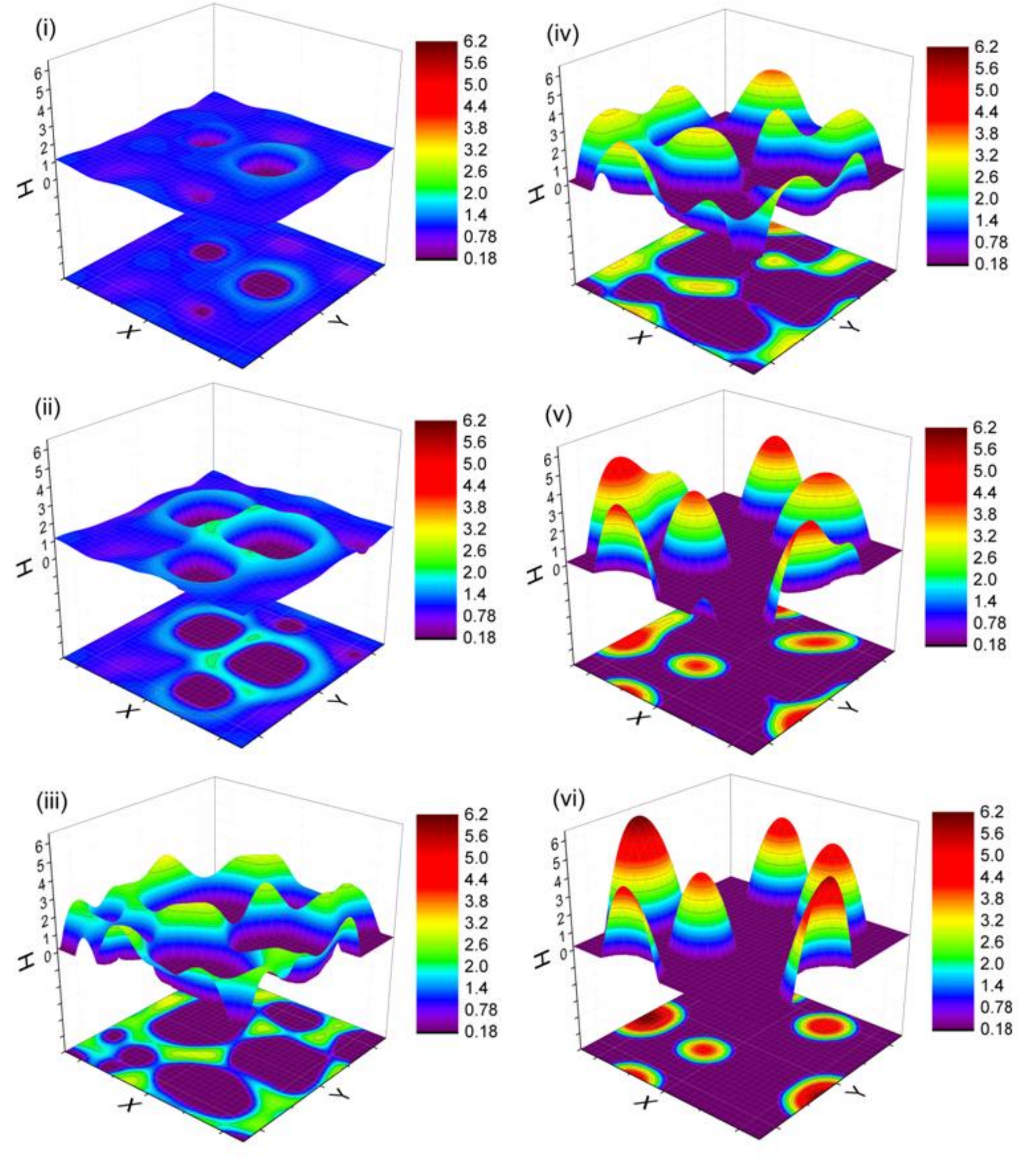

Figure 3.5: Major stages for time evolution of patterns, nondimensional times are t^{*}=29, 30, 32, 33, 35 and 40. $h_0 = 5$ nm and $A = 1.5 \times 10^{-19}(J)$.

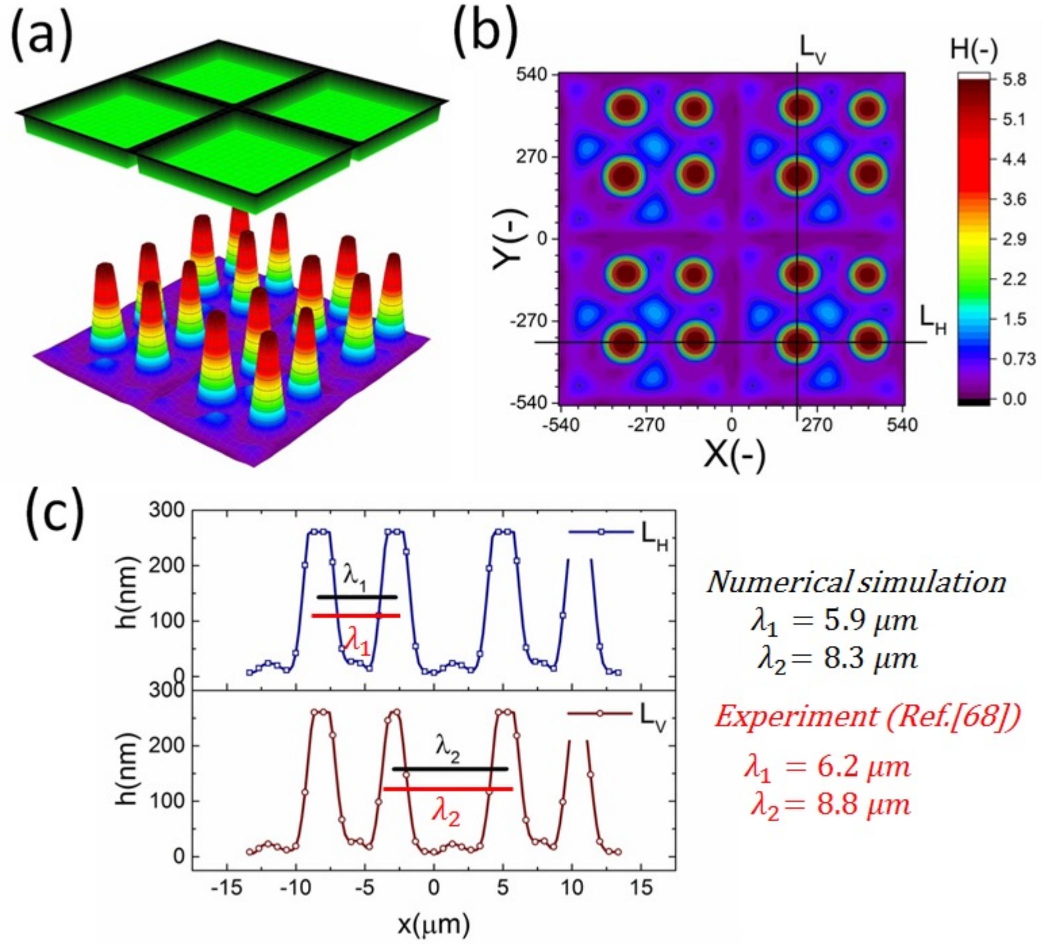

Figure 3.6: Numerical simulation results: (a) 3-D schematic of electrode pattern with square and 3-D snapshot of film structure, (b) 2-D contour of the film structure and (c) cross-section height profile. $h_0 = 45$ nm, $d_1 = 300$ nm, $d_2 = 250$ nm, $\psi_l = 10$ V, $\varepsilon_1 = 2.6$ and $\gamma = 0.038 \, \frac{N}{M}$.

Chapter 4

Electrohydrodynamic patterning of nanofilms using IL model [†]

In the electrohydrodynamic (EHD) patterning process, electrostatic destabilization of the air-polymer interface results in the micro and nano-size patterns in the form of raised formations called pillars. The polymer film in this process is typically assumed to behave like a perfect dielectric (PD) or leaky dielectric (LD). In chapter 3, an electrostatic model (ionic liquid (IL) model, eqns. 3.19 and 3.21) is developed for a finite diffuse electric layer which overcomes the shortcoming of assuming very large and small electric diffuse layer inherent in the PD and LD models respectively. The thickness of diffuse layer forms in nanofilms is comparable with the film thickness which confirms the need for using IL model in EHD patterning process of nanofilms.

This chapter is divided to two sections of EHD patterning of nanofilms using (i) a homogeneous electric field and (ii) a heterogeneous electric field. In the first part, electric potential distribution and the resulting electrostatic pressure are discussed using IL model. Then dynamics and morphological evolution of film interface are discussed and compared with the base-case PD model results. In the second part, the need for using patterned electrode to apply heterogeneous electric field is discussed. Then the influence of electrostatic heterogeneity on the electric-field-induced destabilization of thin IL and PD films is presented. The effect of protrusions shape (strip and square block protrusions) and their size on the dynamics, morphological evolution and pattern formation process of IL films are investigated and the results are compared

---

[†] Parts of this chapter is based on Refs. [3] and [4]

with PD base cases.

4.1 Homogeneous electric field

A thin film system consisting of two layers where the fluid layers are assumed to be Newtonian and incompressible with a constant viscosity, μ, density, ρ and electric permittivity ε are shown in figure 4.1. Unless otherwise indicated, constants and parameters used in the model are listed in Table 4.1.

Table 4.1: Constants or parameters used in simulations for homogeneous electric field.

Parameter	Value
interfacial tension (γ)	0.048 $[\frac{N}{m}]$
viscosity of liquid film (μ)	1 [Pa s]
effective Hamaker constant (A)	-1.5×10^{-21} [J]
permittivity of vacuum (ε_0)	8.85×10^{-12} $[\frac{C}{V\,m}]$
electric permittivity of the liquid film (ε_1)	2.5 ([$-$])
electric permittivity of the bounding media (ε_2)	1 [$-$]
molarity (M)	0.00001$-$0.01 $[\frac{mol}{L}]$
initial film thickness (h_0)	20 $-$ 70 [nm]
electrodes distance (d)	100 [nm]
equilibrium distance (l_0)	1$-$7 [nm]
applied voltage (ψ_l)	20 [V]

The novelty of this work is the addition of the ionic strength of an IL which is determined by IL molarity, M. This is in addition to typical design parameters such as applied voltage ψ_l, electric permittivity of layers ε and electrodes distance d. Hence, a new parameter the ionic strength of IL, which is determined by ILs molarity, M is added. Higher values of M (=0.1 and 0.01 mol/L) account for higher concentration of ions in the layer which results in perfect conducting (PC) behavior M (=0.01 mol/L) whereas lower values of M (=0.000001 mol/L) represent poor conductive medium similar to PDs [116]. The effect of molarity on the electrostatic component of conjoining pressure, as the main force, for pattern formation process is examined.

4.1.1 Electrostatic interaction

To show the effects of molarity on the electric potential distribution across the film thickness, a 50 nm thick IL film bounded with a 50 nm PD media (e.g. air) is considered. Results for four different values of molarity , M, are presented in figure 4.2. Electric potential distribution from the solution of Laplace equation in the bounding media (top 50 nm) is linear as expected.

For M= 0.01 mol/L, electric potential reduction across the IL film is almost zero and IL film behaves like a PC. In this case, the electric field within the IL film is zero. For the limiting case of small molarities M= 0.00001 mol/L, the electric potential distribution is similar to a PD film. For IL films with molarities between these two limiting values, M= 0.001 and 0.0001 mol/L, formation of a DL is evident close to the PD-IL interface and lower electrode (see magnified results in figure 4.2). For M= 0.0001 mol/L, overlapping DL from the interface and the base affects the electroneutrality condition of the entire IL layer. This is due to the large DL thickness, κ^{-1}, as compared to the film thickness. Electroneutrality of bulk is one main assumption in PD and LD models in the literature [23, 82, 93, 96–100] but does not apply in this case.

The value of interface potential, ψ_s, a component of the electrostatic conjoining pressure depends on the molarity of IL film as well as the electric permittivity ratio of layers, $\varepsilon_1/\varepsilon_2$ and the film thickness, h. Interface potential versus interface height for four molarity values of M= 0.01, 0.001, 0.0001, and 0.00001 mol/L are compared in figure 4.3 for a fixed applied potential, ψ_l, electric permittivity of layers, ε_1 and ε_2, and electrodes distance, d. A lower interface height, h, results in a higher interface potential for all molarities which results in a higher conjoining pressure on the interface (see eqn. 3.21). For the case which the PD bounding layer thickness is comparable with the IL film thickness ($h = 50\ nm$ in figure 4.3), higher slope for interface potential occurs for ILs with low molarity indicating that a small change in interface height changes the surface potential considerably. Figure 4.3 confirms that at a constant interface height, a rate of potential drop becomes more significant for lower molarties. On the other hand, as the molarity increases, interface potential becomes more insensitive to the interface height which is similar to the behavior of PC films. In the present work ILs are considered as materials which their height-potential relation lies between the limits of M= 0.01 and 0.00001 mol/L.

The external force in eqn. 3.2 (defined as a gradient of potential,$-\nabla\phi$) also includes the force due to variation of potential with respect to local film thickness, $-\frac{\partial\phi}{\partial h}\nabla h$. This gradient is called spinodal parameter and film instability due to this force called spinodal instability [82]. At a given location, when $\frac{\partial \phi}{\partial h} < 0$, fluid flows from regions with lower thickness to higher thickness (negative diffusion) leading to growth of instabilities. To investigate the instability of IL film subjected to electric field, the term ϕ in eqn. 3.6 is simplified to include only ϕ_{EL} as the electrostatic component since this is dominant compared to other interactions for the EHD patterning [82]. The variations of electrostatic conjoining pressure and the spinodal parameter with interface height for IL films of different molarities are shown in figure 4.4.

A negative value of ϕ_{EL} shows that the electrostatic force pushes the interface toward the upper electrode, often called disjoining force. By increasing the film thickness the electrostatic force is also increased for all three molarity values. Films with higher ions concentration, M= 0.01 and 0.001 mol/L, experience higher electrostatic forces compared to the low concentration case of M= 0.00001 mol/L. This difference is more apparent at higher film thicknesses ($h_0 > 50\ nm$), with thicker films experiencing a higher force (more negative) than the thinner ones. This force accelerates growth of instabilities at initial stages to enhance the growth rate of structures at later stages.

4.1.2 Perfect dielectric films - baseline

To provide insight into the growth of instabilities in EHD pattern formation process, PD films with no free ions ($\rho_f = 0$) are simulated as a baseline for comparison to IL simulations. Since PD simulation has been done [82, 93] the accuracy and capability of the numerical method can be checked.

First the dynamics and spatiotemporal evolution of the liquid film in response to the transverse electric field is investigated. The nondimensional structure height variations over time and 3-D snapshots of a PD film interface, with initial film thickness of $h_0 = 30\ nm$, are presented in figure 4.5. Tracking the structure height over time shows that, the initial random perturbations first grow and when the interface touches the upper electrode for the first time, the minimum height decreases until the film thickness becomes zero. The 3-D snapshots of the PD film interface for four stages of pattern formation process are shown in figure 4.5(a-d). figure 4.5(a) indicates initial random perturbations and formation of bicontinuous structures. At this stage, ridge fragmentation occurs and isolated islands are formed. Fluid flows from regions with lower thickness to higher thickness and eventually pillars are formed. Pillars initially have cone shape (figure 4.5(a)) but become more columnar over time (figure 4.5(b)). The pillar height and width increases over time until they reach the upper electrode (figure 4.5(b)). Then as the contact line expands, the pillars grow in cross-section (figure 4.5(c and d)). The results in figure 4.5 match known results [82, 93] and provide a validation for the code used in this thesis.

4.1.3 Ionic liquid films

In the following mathematical model used for numerical simulation the following points are worth mentioning that: (a) all simulations are terminated at 1 nm (minimum equilibrium distance), which is considered as the limit of the continuum assumption, (b) the analogy of symmetric mono-valent electrolytes is used to analytically relate electrostatic force and DL thickness in ionic liquids, (c) the height between the two electrodes, and the finite volume of the confined liquid film, result in divergence of the hydrodynamic retardation as the electric field intensity diverges which avoids Taylor-cone formation and tip streaming.

EHD patterning of IL films is investigated in this section. Adding free ions to the liquid film is found to increase the electrostatic force significantly (figure 4.4). Thin film height and resulting structures as function of time using 3-D snapshots of a IL film interface, with M= 0.001 mol/L) and initial film thickness of $h_0 = 30\ nm$, are shown in figure 4.6. Tracking of structure height indicates that the first pillar forms after a relatively long time (stage (a)) compared to the total time required for termination of pillar formation process (stages (a-d)) and compared to PD films (figure 4.5). In comparing IL films to PD films, the same sequence of pillar formation is observed. However, the pillars in IL films have a smaller cross-section than those in PD films (figure 4.5 and figure 4.6). For the IL film, pillars are initially formed at random locations and enlarged in cross section with time as the contact line expands on the top electrode. The growth of pillars after touching the upper electrode, depletes the liquid around pillars and forms ring-like depressions around them which is apparent in stage (b).

Increasing the initial film thickness of IL film from $h_0 = 30$ to 50 nm results in faster growth of instabilities and ultimately faster pattern formation process (figure 4.7). However, these patterns are less stable since neighboring pillars tend to coalesce at later stages (figure 4.7(d)). Faster pattern formation and coalescence of pillars at higher initial film thicknesses is also observed in PD films.

To further understand the potential of IL films for making smaller sized patterns in the EHD patterning process, molarity is increased. The effects of molarity and initial film thickness on the number of pillars in the EHD patterning process are presented in figure 4.8. For a fixed area, having a larger number of pillars means formation of smaller sized pillars on the IL film interface. The effect of ionic conductivity of IL films on number of pillars and how fast they form is investigated by varying the molarities from M= 0.00001 to 0.01 mol/L. The results are compared to a PD film of the same initial thickness, $h_0 = 30\ nm$ in figure 4.8(a). In figure 4.8(a) the number of pillars as a function of nondimensional time is plotted. The maximum value of each curve is the final (or maximum) number of pillars formed at the quasi stable condition. Under the same applied voltage, the lowest final number of pillars is formed on the PD film (16 pillars) while 20, 38, 41 and 43 final pillars are formed for the IL films with molarity of M=0.00001, 0.0001, 0.001, 0.01 mol/L. When the molarity of IL film is increased ten times (from M=0.00001 to 0.0001 mol/L), the final number of pillars almost doubled, but a further increase in molarity does not have a significant effect on the final number of pillars (figure 4.8(a)). In addition, it is apparent in figure 4.8(a) that the time gap between the formation of first and the final pillar in the IL film decrease with increasing molarity.

Initial film thickness also affects the final number of pillars as shown in figure 4.8(b). Nondimensional time T, is normalized by initial film thickness cubed, so a modified time is defined as $T^* = Th_0^3$, to cancel the effect of film thickness. Thus three initial film thicknesses of 20, 30 and 50 nm are selected at a constant molarity, $M = 0.0001\ mol/L$ and pillar formation as a function of T^* is plotted in figure 4.8(b). Based on the time axis T^*, films with higher initial thickness and the same interfacial tension and viscosity [96] have faster time evolution which is similar to what is observed in PD films [93]. It is important to note that the above results show the number of pillars formed on the interface from the start to the final number of pillars is in a quasi steady condition. It has been observed that a coarsening of structure in PD films with high initial thickness occurs in further later stages beyond these simulations [82, 96]. The coarsening of structure in IL films and related coarsening mechanism are discussed later. The simulation results show that the number of pillars on the interface increases as the initial film thickness increases as shown in figure 4.8. The number and density of pillars for three

Table 4.2: A summary of number of pillars formed with change of initial film thickness ratio in PD films and IL films with $M = 0.0001\ mol/L$

h_0(nm)	Final number of pillars		Domain size$[(\mu m)^2]$	Density$[\frac{pillars}{(\mu m)^2}]$	
	PD	IL		PD	IL
20	15	22	32.41	0.46	0.68
30	16	38	26.22	0.61	1.45
50	16	52	16.31	0.98	3.19

initial thickness for both IL and PD films are given in Table 4.2. For the IL film the final number of pillars formed on the interface is increased significantly from 22 to 52 when the initial film thicknesses increased from 20 to 50 nm. The number of pillars formed in 1 $(\mu m)^2$ area of the domain is defined as the density of pillars and is given in Table 4.2. The pillar density increases for both PD and IL films as a function of the initial film thickness with IL films having almost 5 times increase (0.68 to 3.19) and PD films having 2 times increase (0.46 to 0.98) in the pillar density.

To gain further insight into the 2-D spatiotemporal evolution of an IL film, a film with 30 nm and molarity of M= 0.00001 mol/L is presented in figure 4.9(a-e) using interface height contours. Figure 4.9(a) shows an early stage of the pattern formation process and contains an initial bicontinuous structure, isolated islands and a first columnar structure formation in one snapshot. Isolated islands from previous stage are developed and converted to columnar structure in figure 4.9(b). The contact lines have expanded on the top electrode and pillars are expanded in cross section. Depletion of liquid around pillars and formation of a ring-like depression around them are more obvious at this stage. The later stages of pillar formation are identified in figure 4.9(c) and (d) by dotted circles. Here coalescence of previously formed pillars is seen. Two neighboring pillars (dotted 1 and 2 in figure 4.9(c)) merge and form one larger size pillar (3 in image (d)). The coalescence of neighboring pillars continues over time and pillars in figure 4.9(d) (dotted circle) merge to an even larger size pillar with oval cross section as shown in the dotted circle in figure 4.9(e).

The dynamics and structure formation on the interface over time for PD and IL films can also be compared using 1-D spatiotemporal evolution of 50 nm IL films at $Y = 0$ (i.e. mid-plane). For an initial film thickness $h_0 = 50\ nm$, IL films with a with molarity of M= 0.001 and 0.0001 mol/L are compared to a PD film and the results are presented in figure 4.13. Increasing time is shown going upward in the subplots. Increasing the ionic conductivity of films (from zero in the case of PD films) results in pillars with smaller diameter and consequently denser structures as seen when comparing figure 4.13(a) to figure 4.13(b and c). The expansion of the contact line on the top electrode is also visible with this 1-D spatiotemporal evolution of interface, figure 4.13 a(ii-iii), b(iii-iv) and c(iv-v). Two mechanisms of pillar coalescence in the EHD patterning process are observed. The first one is Ostwald ripening of neighbor pillars in PD film (figure 4.13 a(iv)-a(vi)) in which incomplete smaller pillar merge with a larger size pillar [96]. The second mechanism is collision of neighbor pillars in IL film with molarity of M= 0.001 mol/L (figure 4.13 c(v)-c(vii)). In the second case, completely formed pillars with almost the same size merge and form larger size pillars. This type of coarsening is also observed in PD films, $h_0/d < 0.5$, which have uniformly distributed pillars [1, 82]. An intermediate stage between the PD film and highly ionic conductive film is shown in figure 4.13 b(i)-b(vii)) where the number of pillars formed is increased compared with the PD film.

4.2 Heterogeneous electric field

In the previous section, it is seen that addition of ionic conductivity to the film results in an increase in number of pillars forming on the interface and consequently more compact structures (pillars with smaller size) are created. The number of pillars formed in the IL films is also increased at higher filling ratios. The PD film shows similar trend below the critical filling ratio of $h_0/d = 0.5$. As a summary, the effects of ionic conductivity and film initial filling ratio (mean initial film thickness to electrodes distance ratio) on the shape and size of structures are shown. Snapshots in time of the 3-D patterns for thin PD and IL liquid films ($d_1 = d_2 = 100$ nm) are presented in figure 4.11.

It is also shown that addition of ionic conductivity to the polymer film leads to more compact but less ordered pillars. Coarsening of of structure happens randomly over the domain similar to the PD [91, 96] films resulting in non-uniform patterns. In PD films, the hexagonally packed pillars typically span about 10 to 15 pillars or they are randomly distributed over the domain [91]. To overcome this limitation, a patterned mask is used to electrostatically control the structures size and fluid patterns. Using a patterned mask, which results in replication of mask on the polymer film, has been already investigated for the PD and LD films [59, 65, 68, 80, 82, 93, 100, 142, 143]. Fabricating controllable submicron sized structures using the EHD patterning process is the main objective of this section and the influence of electrostatic heterogeneity on the EHD pattern formation of thin IL films is investigated.

A schematic of thin liquid film resting on a lower electrode and confined with a patterned upper electrode (i.e. mask) is shown in figure 2.2 (a). The gap between the film and the mask can be filled with air or a polymer. It is assumed that the material properties of the layers such as interfacial tension, viscosity and dielectric permittivity are constant. Gravity effects are neglected and it is assumed that the liquid film is incompressible Newtonian fluid. Constants and parameters used through this study are presented in in Table 6.1.

Table 4.3: Constants or parameters used in simulations for heterogeneous electric field.

Parameter	Value
mean initial film thickness (h_0)	$20 - 70$ [nm]
electrodes distance (d_1 and d_2)	$80 - 300$ [nm]
protrusions width (W_1)	0.64−2.56 [μm]
groove width (W_2)	0.64−2.56 [μm]
equilibrium distance (l_0)	1 [nm]
applied voltage (V)	20 [V]
Molarity (M)	0.0001 [$\frac{mol}{L}$]

4.2.1 Conjoining/disjoining pressure

The final shape and size of features in the EHD patterning process is a result of a balance between the electrostatic (as the main driving force), intermolecular, viscous and interfacial force [84]. Distribution of conjoining/disjoining pressure components acting on the film interface under heterogeneous electric field are compared in figure 4.12. The 2-D cross-section height profile of the upper electrode and patterned film is shown in figure 4.12 (a and b), respectively. The Laplace pressure (figure 4.12 (c)), the van der Waals pressure (figure 4.12 (d)) and electrostatic pressure for the PD (figure 4.12 (e)) and IL (figure 4.12 (f)) films are all scaled with the electrostatic pressure acting on the PD film at initial stage (flat interface) when exposed to homogeneous electric field ($d_1 = d_2 = 100$ nm and $h_0 = 30$ nm).

Negative (positive) pressure values in figure 4.12 represent the upward (downward) direction in which the interface is pushed toward upper (lower) electrode. The electrostatic pressure has a negative value over the domain irrespective to the interface pattern but its magnitude changes significantly with interface height (figure 4.12 (e and f)). The thin film is exposed to higher electrostatic force under protrusions (decreased electrode distance) caused by a lower electric potential drop in bounding layer. Thinner film regions also experience lower electrostatic pressure compared to the thicker regions (located under protrusions) which results in fluid flowing from thinner regions to thicker regions. This confirms the destabilizing role of the electrostatic pressure in the EHD patterning process.

The curvature of the interface determines the Laplace pressure with a convex shape of the interface (in the valleys) resulting in negative values for pressure and vice versa (figure 4.12 (c)). Film regions with higher (lower) interface height experience a pressure toward the lower (upper) electrode. As a consequence, the Laplace pressure tends to flatten the interface, thereby stabilizing the film in contrast to the destabilizing effect of electrostatic pressure.

Short ranged van der Waals forces are considered in the simulation of the EHD pattering process when the film thickness is less than 100 nm. The van der Waals forces depend on the property and surface energy of materials used for electrodes, film and the bounding fluid. In the present work, the lower electrode surface (apolar substrate) has higher energy compared to the liquid film leading to spinodally stable film (negative values for the pressure, shown in figure 4.12 (d)) for the initial stage of the EHD patterning process.

Using a patterned electrode applies a heterogeneous pressure on the film interface leading to replication of upper electrode pattern onto the polymer film (figure 4.12 (a and b)). The distribution of scaled electrostatic pressure (Φ_{ES}) acting on the IL film at initial stage (i.e. flat interface) is compared with a PD film as shown in figure 4.12 (e) and (f). A smaller electrode distance results in a higher electrostatic pressure in both ILs and PDs; however, the IL films experience higher electrostatic pressure compared to the PD films at the protrusions regions (38 times higher in the case considered here).

4.2.2 Morphologies in heterogeneous electric field

The effect of heterogeneous electric field on the EHD patterning of PD and IL films using strip-like and block protrusions is discussed. Effects of the size and shape of the patterns and initial filling ratio on the EHD pattering process and morphology of structures are investigated.

Strip-like protrusions:

The 3-D snapshots of the thin IL film interface are used to show the change in structure height over time under a heterogeneous electric field with strip-like patterns in figure 4.14. Mean initial film thickness, h_0 is 30 nm and electrode distances d_1 and d_2 are 100 and 188 nm, respectively. Protrusions width, W_2 is 0.64 μm and the groove width, W_1 is 2.88 μm. Fluid interface height increases toward the upper electrode with the same rate as it decreases downward during the initial linear stage (i) of the process (see figure 4.14 (b)). This growth in height results in formation of undulating 2-D structures mainly under the protrusions region (see figure 4.14 c(i)) where the ridges are surrounded by grooves. In the next stage (ii), fragmentation occurs and raised initially cone shape structures form which occur randomly along the ridges (see figure 4.14 c(ii)). Next the raised structures bridge the upper and lower electrodes and their cross-section enlarges to form raised columnar structures (pillars) (see figure 4.14 c(iii)). A further increase of the size of pillars from the collision of neighbor pillars and their coalescence leads to formation of larger size pillars (see figure 4.14 c(iv)). The width of the pillars in this case is less than 0.4 μm which is about 38% less than the width of protrusions on the electrode.

For comparison, a 3-D snapshot of the PD film structure formed at similar condition is shown in figure 4.14 (d) which has much fewer pillars with oval cross-section formed under the protrusions. The cross-section height profiles (along the L_1 and L_2) provide more information regarding the size and shape of pillars in the PD and IL films (figure 4.14 (f and g)). The center-to-center distance of adjacent pillars in the PD and IL film is around 2.6 and 1.2 μm respectively. A 53% reduction of pillar width in the IL film, compared to the PD film, is achieved. Cross-section height profile along the X direction (L_2) for the PD and IL films shows that the pillars are not necessarily aligned in the x direction. Hence the number of pillars and their shape may vary between the protrusion lines.

When a flat electrode is replaced with the patterned one, two characteristic spatial lengths are identified. The first is the spacing distance that pillars form within each protrusions (λ_1) and the second characteristic length is the distance of pillars form in two neighbor protrusions (λ_2). The first one is controlled by the same parameters that affect the EHD patterning process of pattern-free electrodes such as applied voltage, film filling ratio and electric permittivity, etc. But the second one can also be controlled by adjusting the groove width.

To investigate the effect of patterned electrode on the IL films, the width of protrusions is increased from 0.64 to 2.56 μm. Structures formed at the quasi steady state stage (stage (iv) in figure 4.14 (b)) of the EHD process are compared in figure 4.15. Protrusions height and applied voltage are the same as in figure 4.14. Results for the PD and IL thin films with the mean initial thicknesses of 30 nm in figure 4.15 (b and c) and 50 nm in figure 4.15 (d and e) are presented. The 30 nm thick IL film, forms two rows of pillars under the protrusion at the middle whereas in the PD film just one row of pillars is formed. In addition, the number of pillars formed in one row of the IL film is higher than in the PD film. For the 30 nm film thickness using a patterned electrode reduces the size of pillars in the IL films compared to a PD films. As previously mentioned, when a flat electrode is used, increasing the initial ILs film thickness resulted in more compact structures with smaller sizes (see figure 4.11 (b and c)). However, increasing the initial film thickness for the patterned electrode case results in formation of roll-like structures.

The effect of reducing the groove width (w_1) from 2.46 to 0.64 μm at constant width of protrusions (2.56 μm) is investigated and the 3-D snapshots of the structures formed in the PD and IL films are shown in figure 4.16. The total number of pillars for the PD film is 12 whereas it exceeds 46 pillars for the IL film at the same condition. By decreasing the width of grooves from 2.46 to 0.64 μm the undulating patterns are not formed under the grooves. Therefore the groove width should be smaller than the strip width to avoid secondary pattern formation under the low electric field (high gap) regions. Finally, by using an appropriately patterned electrode, smaller size features are generated and the structures are more compact and well ordered.

Square block protrusions:

Another common shape of protrusions used in the EHD pattering is the square block protrusion [59, 68, 82]. The square shape protrusions are used to create heterogeneous electrostatic force in both x and y directions to control the two length scales. In order to validate our numerical simulation, the EHD patterning of PD film is simulated for the same experimental condition reported in literature [68]. A schematic of electrode pattern and 3-D snapshots of the pattern formed on the PD and IL film at quasi-steady stage of pattering process are shown in figure 4.17 (a-c). Experimental [68] (not shown here) and simulation both result in four pillars forming with identical height under the square protrusions. Based on our simulation, the pillars formed in the IL film are located exactly at the corners whereas for the PD film they are close to the center. The pillar size is reduced by 42% in the IL film as compared to the PD film. Examining figure 4.17 (b) and 4.17 (c) closely, it can be seen that an equal number of pillars are formed in both PD and IL films for square block protrusions This differs from the case of strip-like protrusions where more pillars were observed in the IL film. A possible explanation for this result may be the lack of adequate polymer liquid fluid to create more pillars due to low initial thickness of the IL film with respect to the electrodes distances.

The cross-section height profile of the interface for the PD and IL films are compared in figure 4.17 (d). The intra-array spacing of $\lambda_1 \sim 5.9$ μm and $\lambda_2 \sim 8.3$ μm in the PD film match the experimental observation [68] of $\lambda_1 \sim 6.2$ μm and $\lambda_2 \sim 8.8$ μm with reasonable accuracy. This provides validation of the fidelity and accuracy of simulation results for the prediction of the patterned formed in the EHD process–at least for this case. In the IL film, the center to center distance of pillars under the block protrusions is increased to $\lambda_1 \sim 9$ μm and the distance between the neighbor blocks is decreased to $\lambda_2 \sim 4.5$ μm.

To create well ordered structures with higher number of pillars, the electrode distances are reduced to $d_1 = 100$ nm, $d_2 = 80$ nm and an electrode mask with square protrusions ($W_1 = W_2 = 0.84$ μm) is used. A schematic of the upper electrode and spatiotemporal evolution of PD and IL films are shown in figure 4.18. Tracking the interface height over time (figure 4.18 b(i)), it is found that the pattern formation includes three main stages. First, the interface is pushed toward the upper electrode in regions with higher electrostatic force (under the protrusions) and castle shape structures with four corner towers are formed. The cone shape structures are formed close to the corners of squares as the gradient of electrostatic force is higher at these boundaries (figure 4.18 b(ii) and c(ii)). Fluid depletion around boundaries (blue color ring in color print) is evidence of fluid flow from thinner regions to the thicker ones. The cone shape structure formed in the IL film are thinner compared to the PD film and formed at the corners, whereas in the PD film they are closer to the center. In the second stage, collision and coalescence of neighbor cones in the PD film occurs even before completion of the pillar formation. Hence, in the PD film, only one pillar is formed under the protrusions bridging the two electrodes (figure 4.18 b(iii)) while in the IL film, four pillars with separate ring shaped fluid depletion are formed (figure 4.18 c(iii)). In the third stage of pattern formation, secondary pillars are formed in the low electric field region (under the grooves) in both PD and IL films (figure 4.18 b(iv) and c(iv)). In the IL film the four pillars formed under the protrusions are merged and form a pillar with a larger cross-section (similar to stage ii in the PD film), then the secondary pillars are created. The number of secondary pillars in the IL film is doubled compared to that in the PD film. Reducing the electrodes distances d_1 from 188 nm to 100 nm and d_2 from 100 nm to 80 nm results in secondary pillars formation under the grooves. This can be used to create multi level structure formation.

To further examine the effect of protrusion size, W_2 is increased to $W_2 = 1.26\ \mu\text{m}$ $(= 1.5 \times \lambda_m)$ and the groove width is reduced to $W_1 = 0.42\ \mu\text{m}$ $(= 0.5 \times \lambda_m)$ as illustrated in figure 4.19 a(i). As seen in figure 4.18 b(iii) and c(iii), using protrusions with the same size as the characteristic wavelength for growth of instabilities $W_2 = \lambda_m$ results in formation of one (four) pillar(s) under the protrusions in the PD (IL) film. Increasing the protrusion size leads to formation of four (nine) pillars in the PD (IL) film. The groove width is chosen narrow enough to avoid the secondary pillars formation (figure 4.19 a(ii and iii)). More detailed information regarding the size of pillars and their intra-spacing is shown in figure 4.19 a(iv). The center to center distance of pillars formed under the protrusions (λ_1) is reduced to ∼0.675 for the PD and 0.43 μm for the IL film. By reducing the grooves width, the secondary pattern is no longer formed under the grooves for both PD and IL films. The distances between neighboring pillars under the grooves (λ_2) is around 1.0 and 0.78 μm in the PD and IL film respectively.

The results show that for every n pillars that are formed with a PD film, $(\sqrt{n}+1)^2$ pillars would be created using an IL film under the same condition. Although the number of pillars formed in the PD is less than the IL film, the size of pillars in the PD film are identical. In the case of IL film, the pillars located at the pattern center are smaller than those formed at the corners resulting in non-uniformity of pillar sizes. To have a maximum number of pillars with identical shape and size, a new pattern with nine uniform square block protrusions and the same patterning domain of $3.37 \times 3.37 \mu\text{m}^2$ as figure 4.18 (a) is used (see figure 4.19b(i)). From previous numerical results (figure 4.18 b(iii) and c(iii)) it is expected to have one (four) pillar(s) under each protrusion in the PD (IL) film. Since only one pillar forms under each protrusions in the PD film the center to center distance of pillars changes with the groove width ($\lambda_1 = \lambda_2 \sim 1.1$ μm). In the IL film, the intra-array spacing of $\lambda_1 \sim 0.47$ μm and $\lambda_2 \sim 0.6$ μm is found to create consistent sized structures over the patterning area and maximizes the number of pillars.

4.3 Summary

When a transverse electric field is applied to IL film, the free ions move and accumulate close to the charged surfaces. This results in the formation of diffuse layers, called double layers, which are absent in perfect dielectric (PD) and leaky dielectric (LD) models. An electrostatic model is developed for confined IL films in contact with PD bounding media via coupling of linearized Poission-Boltzmann and Laplace equations to obtain the electric potential distribution and consequently the net electrostatic pressure acting on the interface. The key insight our electrostatic model provides is that, the leaky dielectric model may not account for phenomena important for EHD patterning, namely the presence of finite ions in the conducting layers. Debye length is defined using ionic strengths, which provides a realistic range of free charge concentrations in the conducting fluid layer compared to the previous work in literature [116].

The developed IL model is not limited to having very large or small electric diffuse layer as assumed in the PD and LD models respectively. This model is coupled to the nonlinear thin film equation and solved numerically to investigate the dynamics, instability and process of pattern formation in the EHD patterning process. Based on this model, ionic liquids are defined to be materials having properties between two limiting cases of PC and PD materials based on their ionic strength. IL films experience a much higher electrostatic pressure compared to similar PD films (with the same electric permittivity) and an increase in ionic strength results in higher electrostatic pressure. PD films are modeled first to investigate the accuracy of numerical scheme and to provide a well known baseline case (compared to experiment) and then compared to the results with IL thin films. Finally IL films of various molarity are numerically simulated and the structure and number of pillars is compared to PD films.

For the case of homogeneous electric field application several observations are noted. Early stages of pillar formation process in IL films is found to be similar to PD films and electric induced instabilities grow is caused by negative diffusion. Pillars are initially formed on the random locations and enlarge in cross section over time as the contact line expands on the top electrode. The pillars formation process occurs faster in IL films and is further accelerated with increasing the ionic strength. Generally, smaller structures are found in IL film when compared to similar PD films and increases with initial film height. For the case of increasing h_0 from 20 to $50nm$, the IL film with $M = 0.0001\ mol/L$ gets 5 times more structures per $(1\mu m)^2$ while it increases is about 2 times in the PD film.

It is also shown that addition of ionic conductivity to the polymer film leads to more compact but less ordered pillars. Coarsening of of structure happens randomly over the domain similar to the PD films [91, 96] resulting in non-uniform patterns. To overcome this limitation, a patterned mask is used to electrostatically control the structures size and fluid patterns.

The effects of protrusion and groove size (width and depth) in strip-like and square block patterns and the film initial filling ratio on the size, shape and order of fluid patterns are investigated. When flat electrode is replaced with the patterned electrode, two characteristic spatial lengths are identified which are controlled by the: width of strip/square block (W_2), groove width (W_1) and groove depth ($d_1 - d_2$). Results show that depending on the groove width and depth the EHD patterning process has either two or three main stages. In the two-stage process, patterns only form under the protrusions whereas in the three-stage one, pattern (either undulating or secondary pillars) also form under the grooves. The two-stage process can be used for the pattern replication of mask onto the film and the three-stage one is utilized when a multilevel structure formation is desired. Furthermore, more pillars are found to be created using IL film rather than PD film. By using electrodes with square protrusions $(\sqrt{n} + 1)^2$ pillars are formed in IL film for every n pillars generated in PD film. In the PD film, electrode square block mask protrusions with width of $W_2 = 1.5 \times \lambda_m$ and groove width of $W_1 = 0.5 \times \lambda_m$ and in the IL film square block protrusions with width of $W_2 = \lambda_m$ and groove width of $W_1 = 0.25 \times \lambda_m$ result in compact and well ordered fluid pillars.

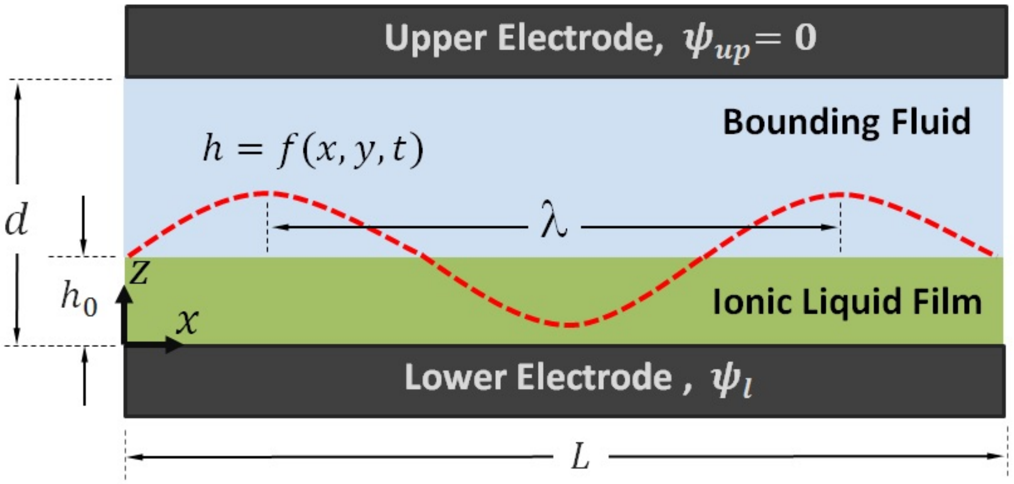

Figure 4.1: Schematic view of the thin film sandwiched between electrodes. $h = f(x, y, t)$ is the film height described by the function with the lateral coordinates and time. λ is the maximum growing wavelength.

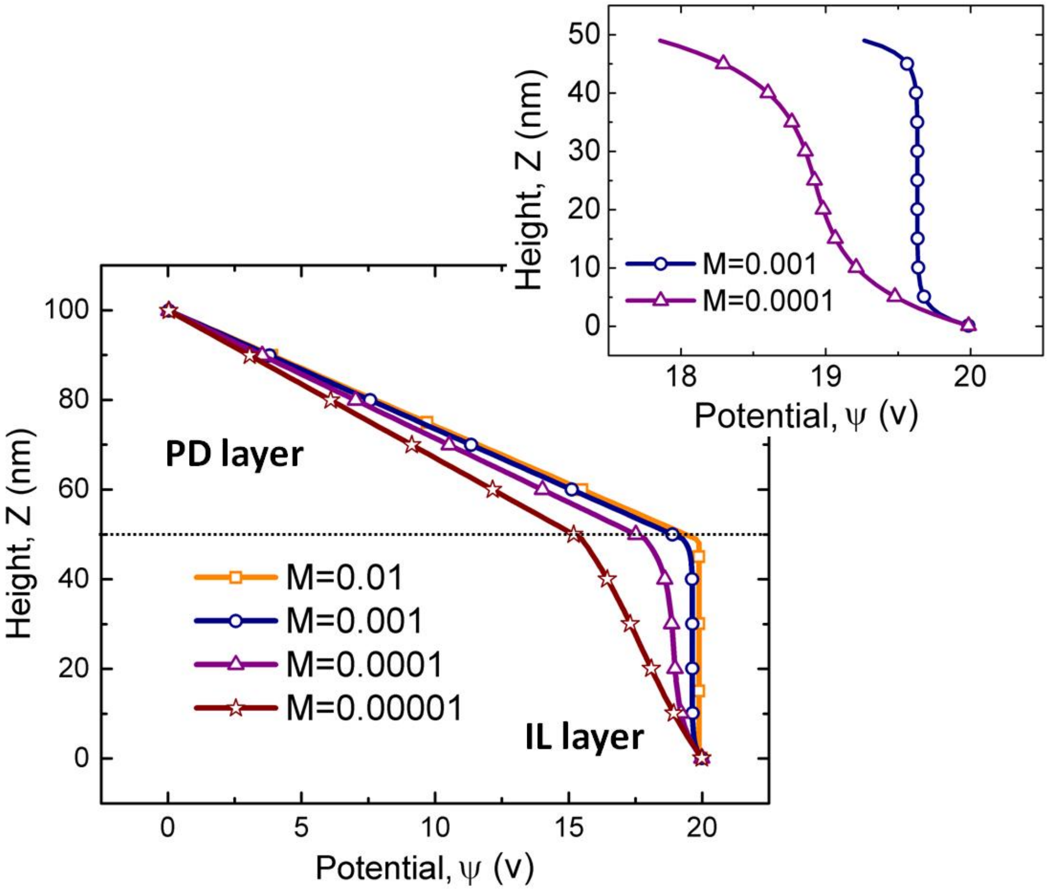

Figure 4.2: Electric potential distribution versus height for four molarity values of M= 0.01, 0.001, 0.0001, and 0.00001 mol/L and corresponding Debye lengths, $(\kappa)^{-1}$ are: 0.5, 1.7, 5.4 and 17 nm

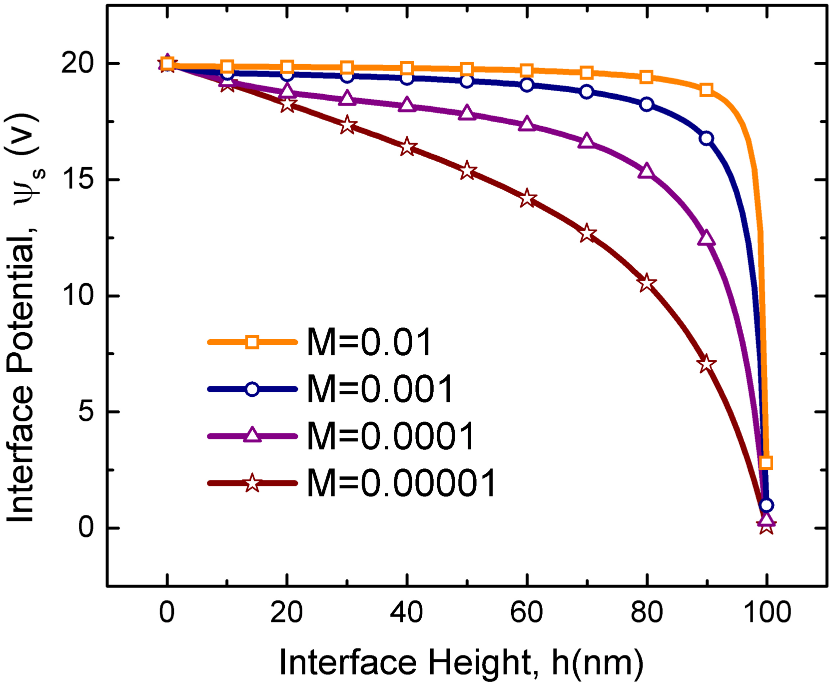

Figure 4.3: Interface potential distributions versus interface height for four molarity values of M= 0.01, 0.001, 0.0001, and 0.00001 mol/L. $\phi_l = 20\ V$, $\varepsilon_1 = 2.5$ and $\varepsilon_2 = 1$

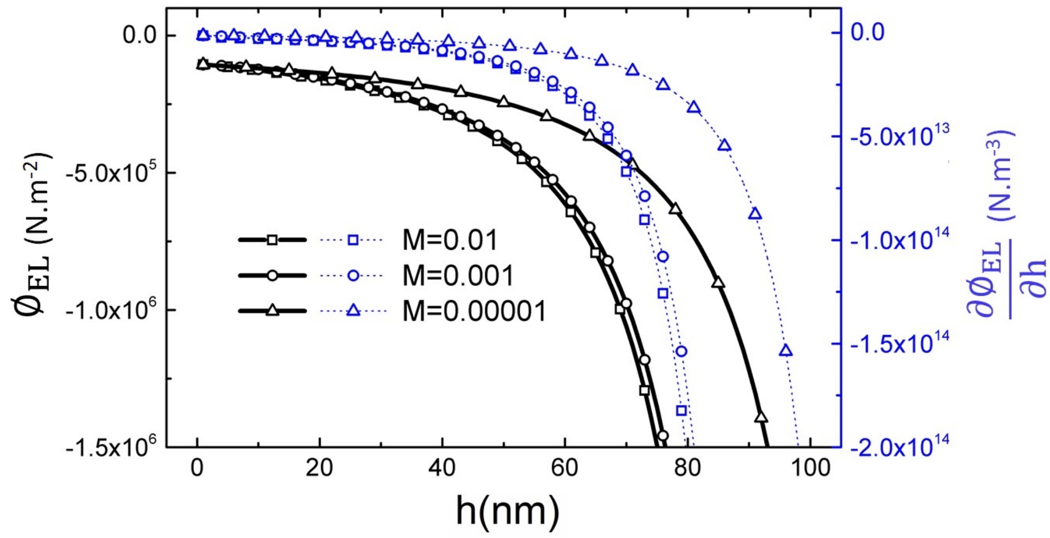

Figure 4.4: Electrostatic pressure, left axis, and spinodal parameter, right axis, distributions versus film thickness for three molarity values of M= 0.01, 0.001 and 0.00001 mol/L. $\phi_l = 20\ V$, $\varepsilon_1 = 2.5$ and $\varepsilon_2 = 1$

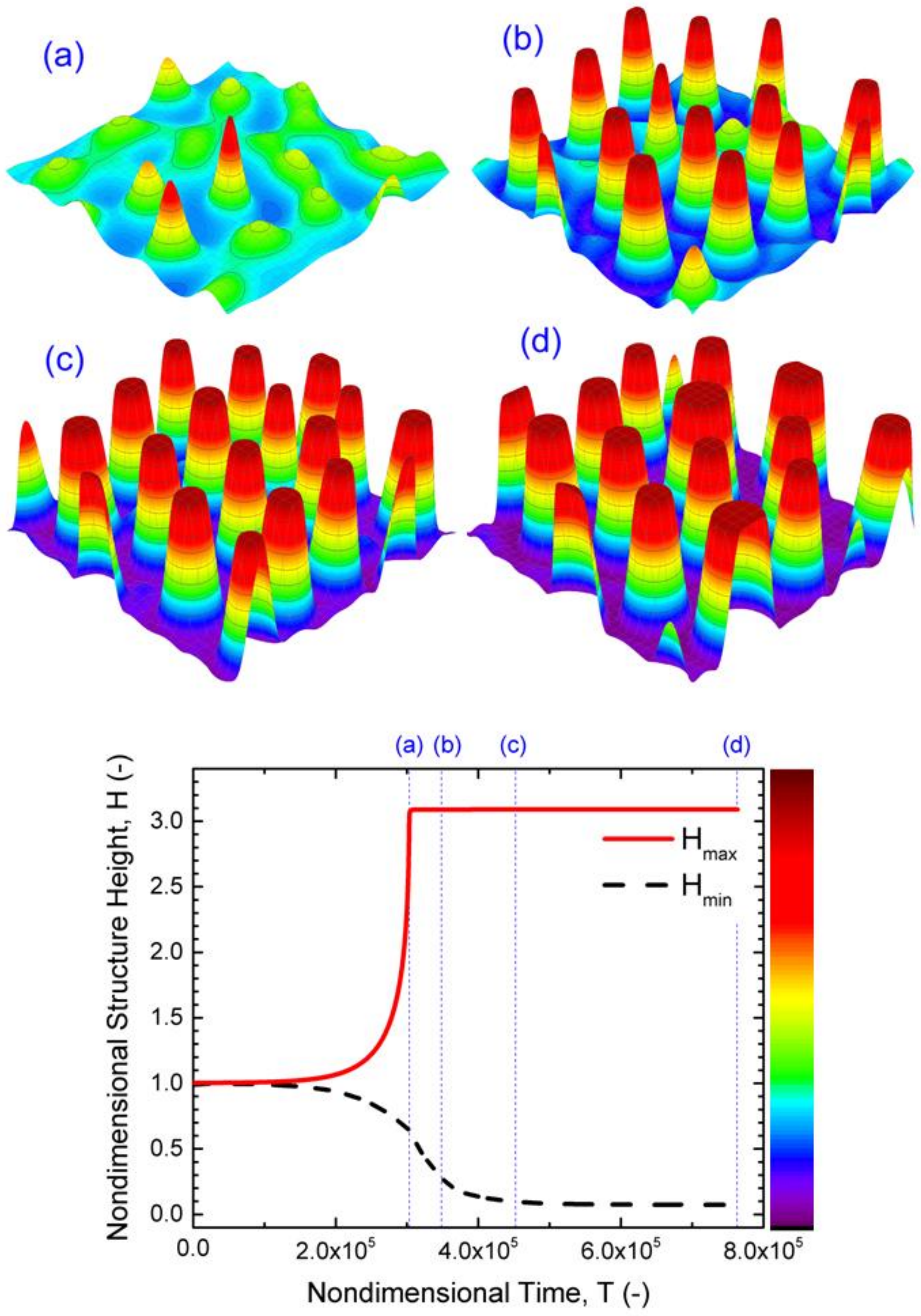

Figure 4.5: PD film with $h_0 = 30\ nm$, 3-D spatiotemporal evolution of a PD liquid PD film (images a-d) and nondimensional structure height variations versus nondimensional time. Nondimensional times, T are: (a) 3×10^5 (b) 3.5×10^5 (c) 4.5×10^5 and (d) 7.6×10^5. and $\psi_l = 20\ V$

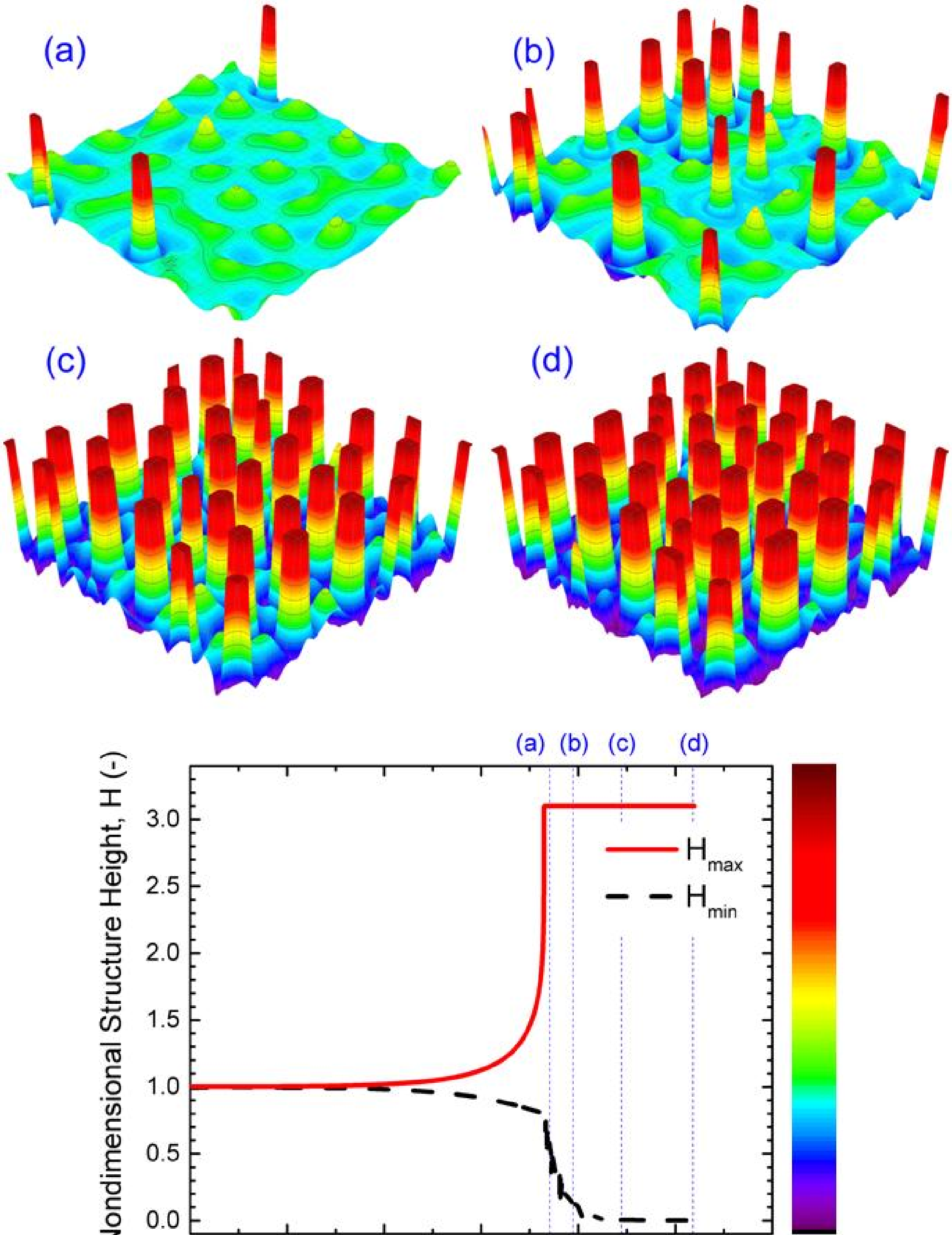

Figure 4.6: IL film with $h_0 = 30\ nm$, 3-D spatiotemporal evolution of a IL liquid film (images a-d) and nondimensional height variations versus nondimensional time. Nondimensional times, T are: (a) 7.4×10^4 (b) 7.9×10^4 (c) 8.9×10^4 and (d) 1×10^5. M= 0.0001 mol/L and $\psi_l = 20\ V$

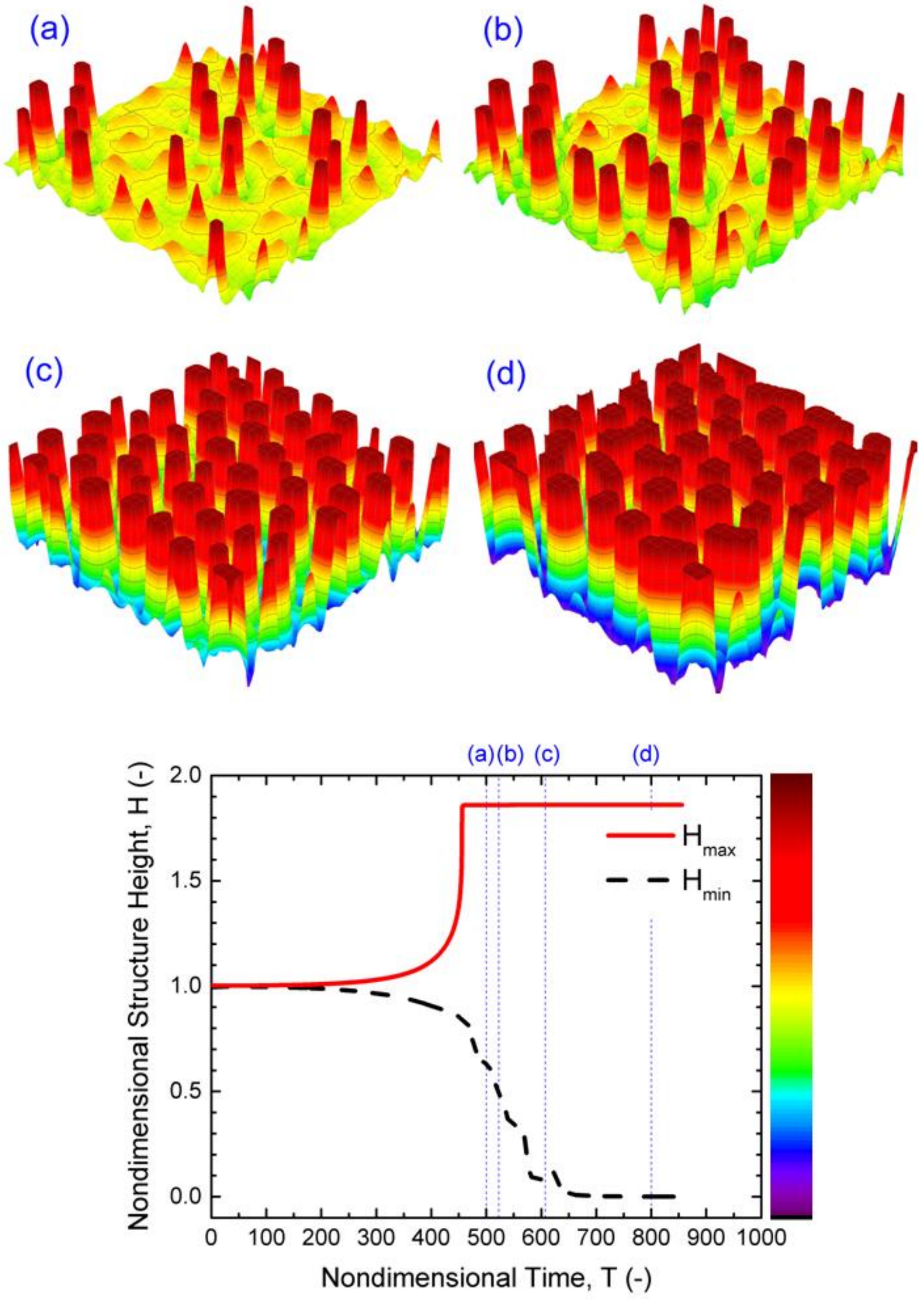

Figure 4.7: IL film with $h_0 = 50\ nm$, 3-D spatiotemporal evolution of a IL liquid film (images a-d) and nondimensional structure height variations versus nondimensional time. Nondimensional times, T are: (a) 5×10^2 (b) 5.2×10^2 (c) 6×10^2 and (d) 8×10^2. M$= 0.0001\ mol/L$ and $\psi_l = 20\ V$

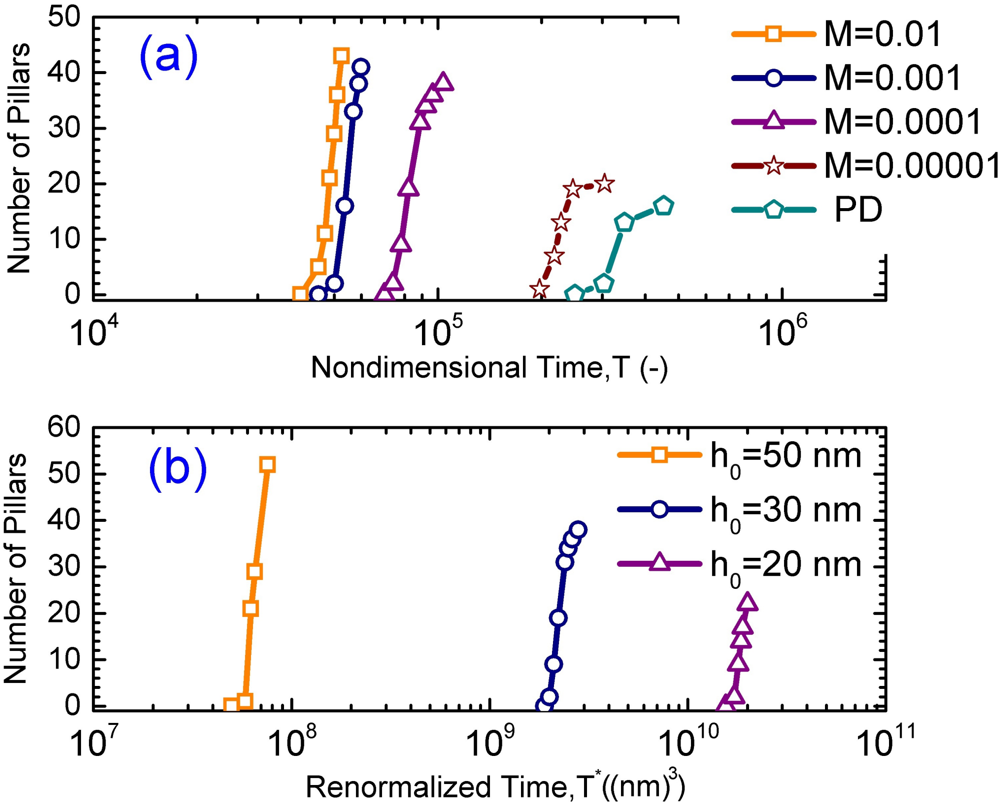

Figure 4.8: Number of pillars formation with (a) molarity changes with constant initial film thickness of $h_0 = 30\ nm$ and (b) initial film thickness changes with constant molarity M= 0.0001 mol/L

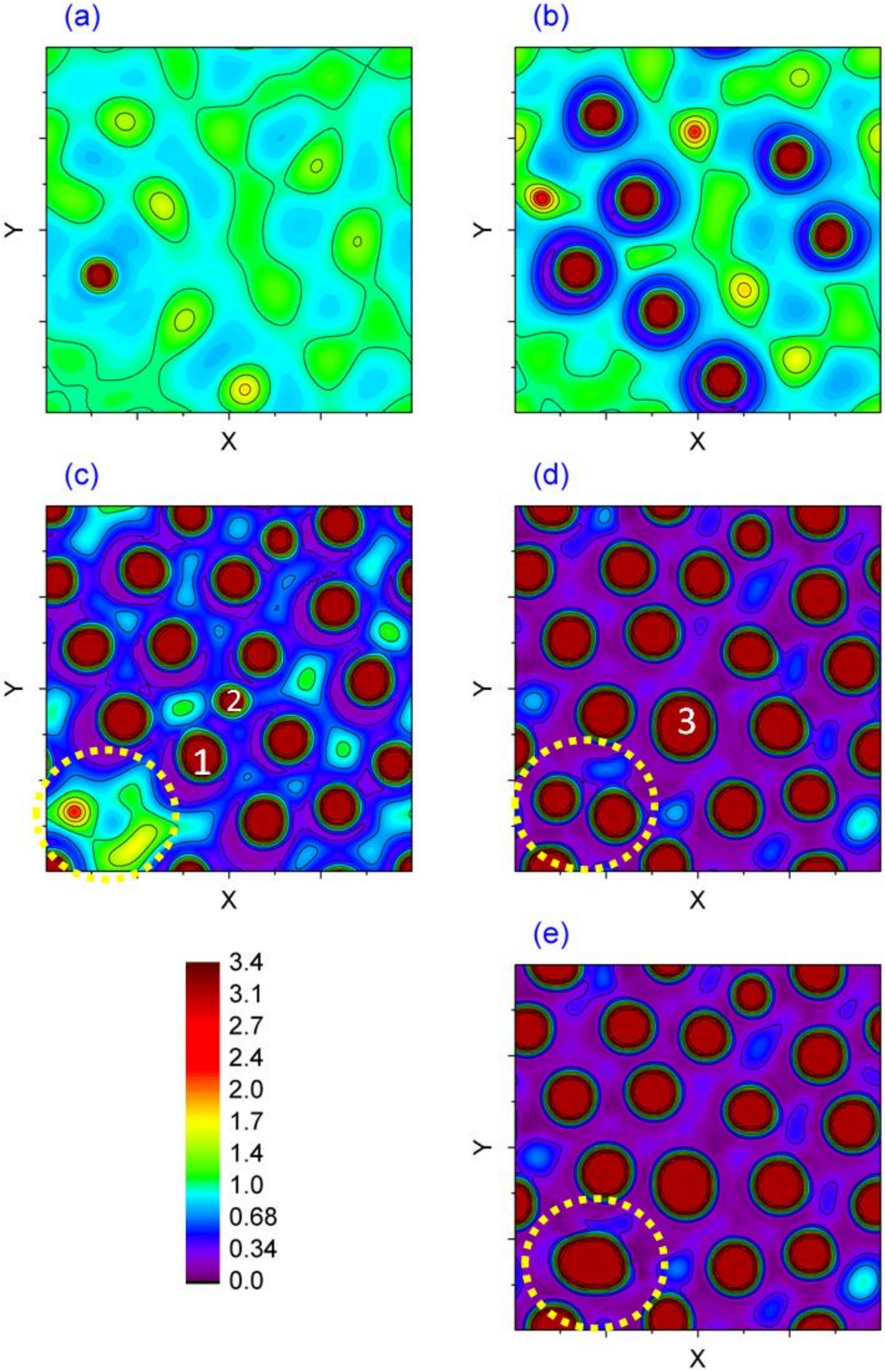

Figure 4.9: 2-D spatiotemporal evolution of a 30 *nm* IL film with molarity of M= 0.00001 *mol*/*L*. Nondimensional times, *T*, are (a) 197650, (b) 217980, (c) 247010, (d) 304670 and (e) 329150

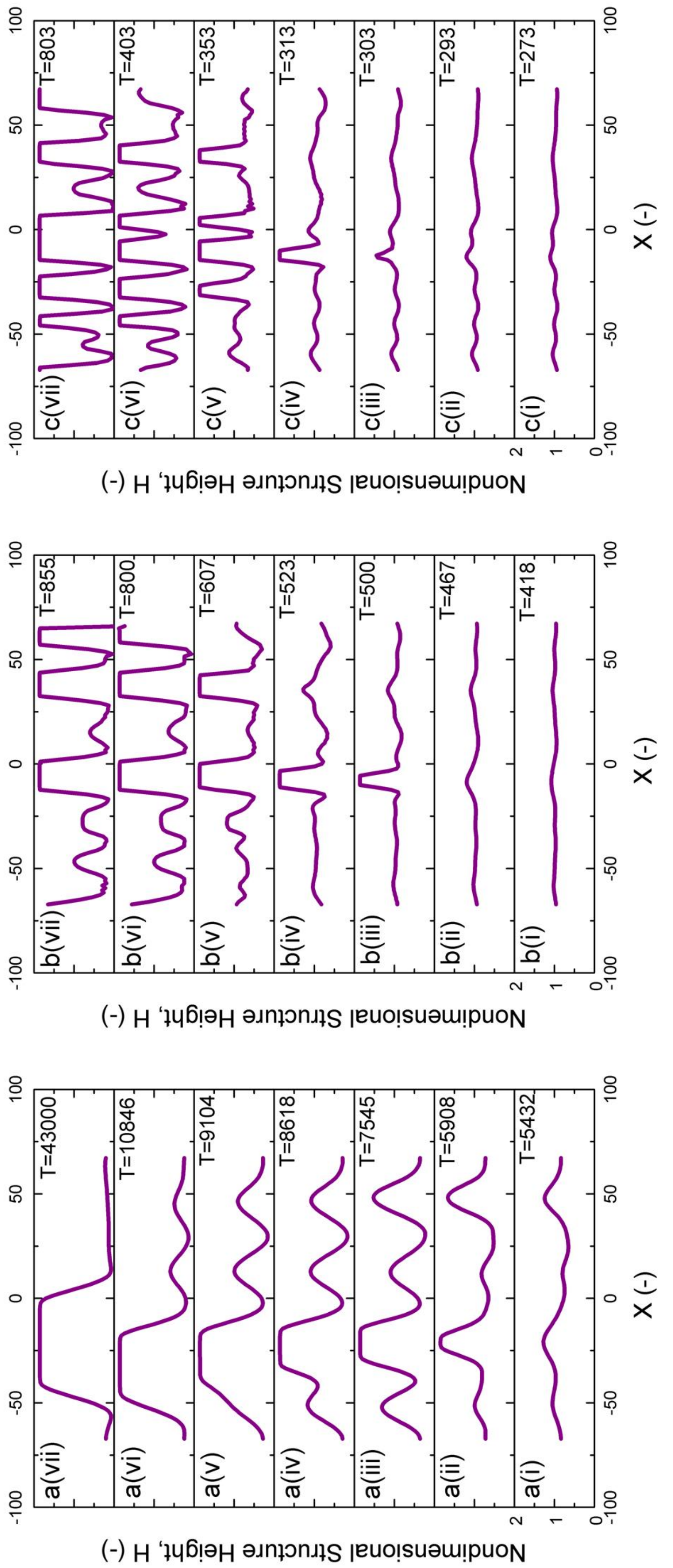

Figure 4.10: 1-D spatiotemporal evolution of 50 nm initial thick at $Y = 0$. (a) PD film and IL films with (b) M= 0.0001 and (c) M= 0.001 mol/L

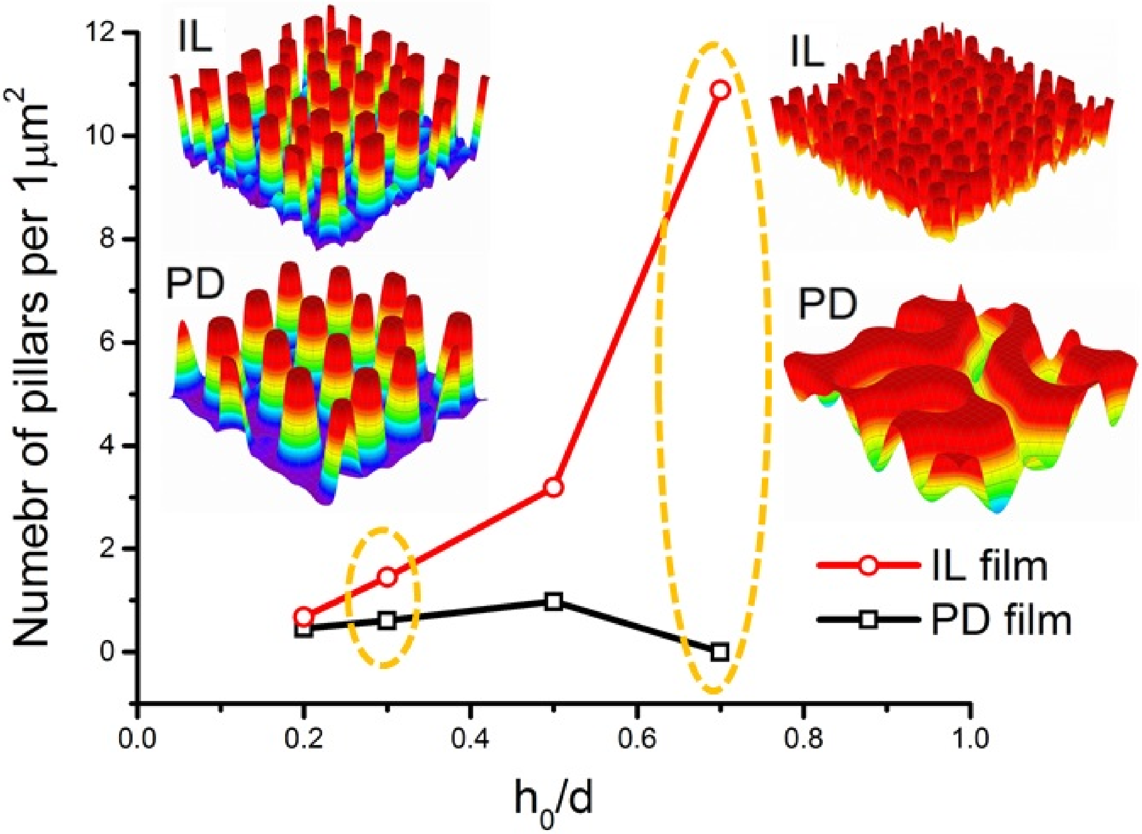

Figure 4.11: Total number of pillars versus initial filling ratio of film. 3-D snapshots of the patterns formed in PD and IL films with $h_0 = 30$ and 70 nm. $d_1 = d_2 = 100$ nm, $V = 20$ V.

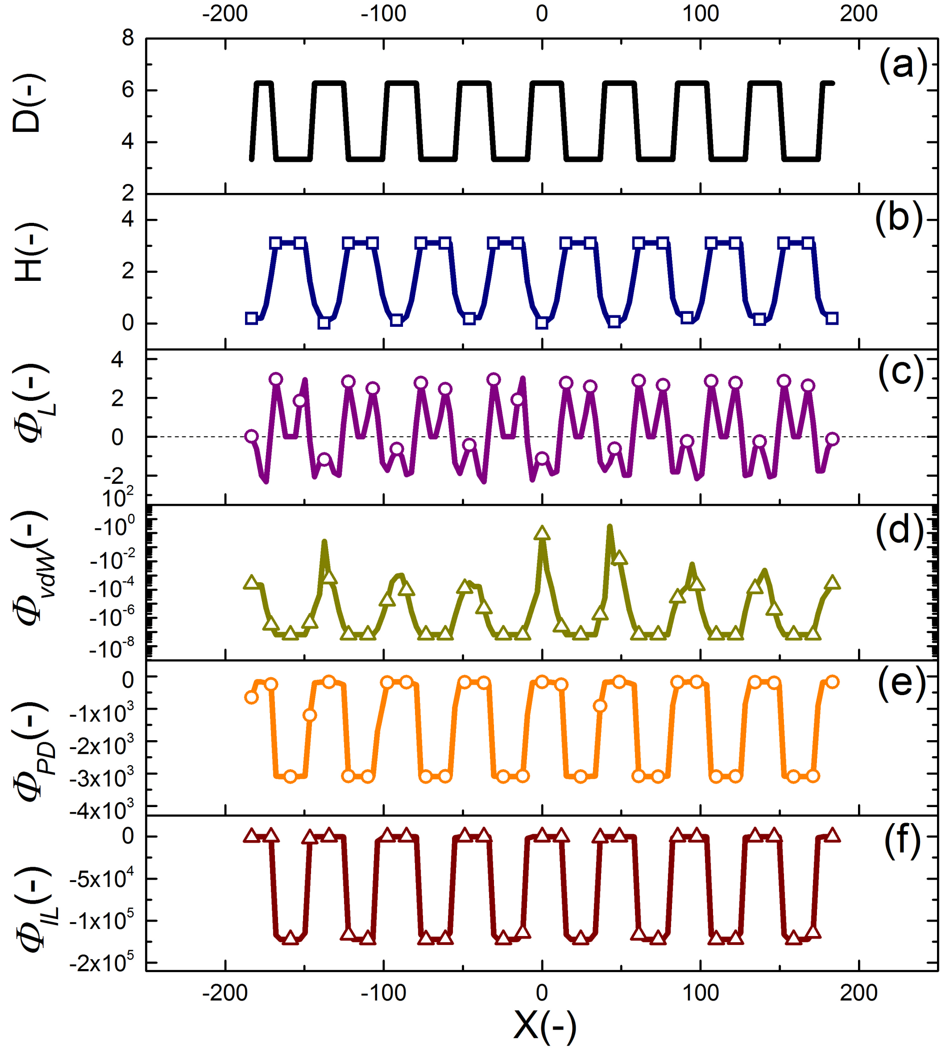

Figure 4.12: 2-D non-dimensional profile of (a) upper electrode, (b) patterned film interface, (c) Laplace pressure, (d) van der Waals pressure, electrostatic pressure acting on (e) PD and (f) IL film.

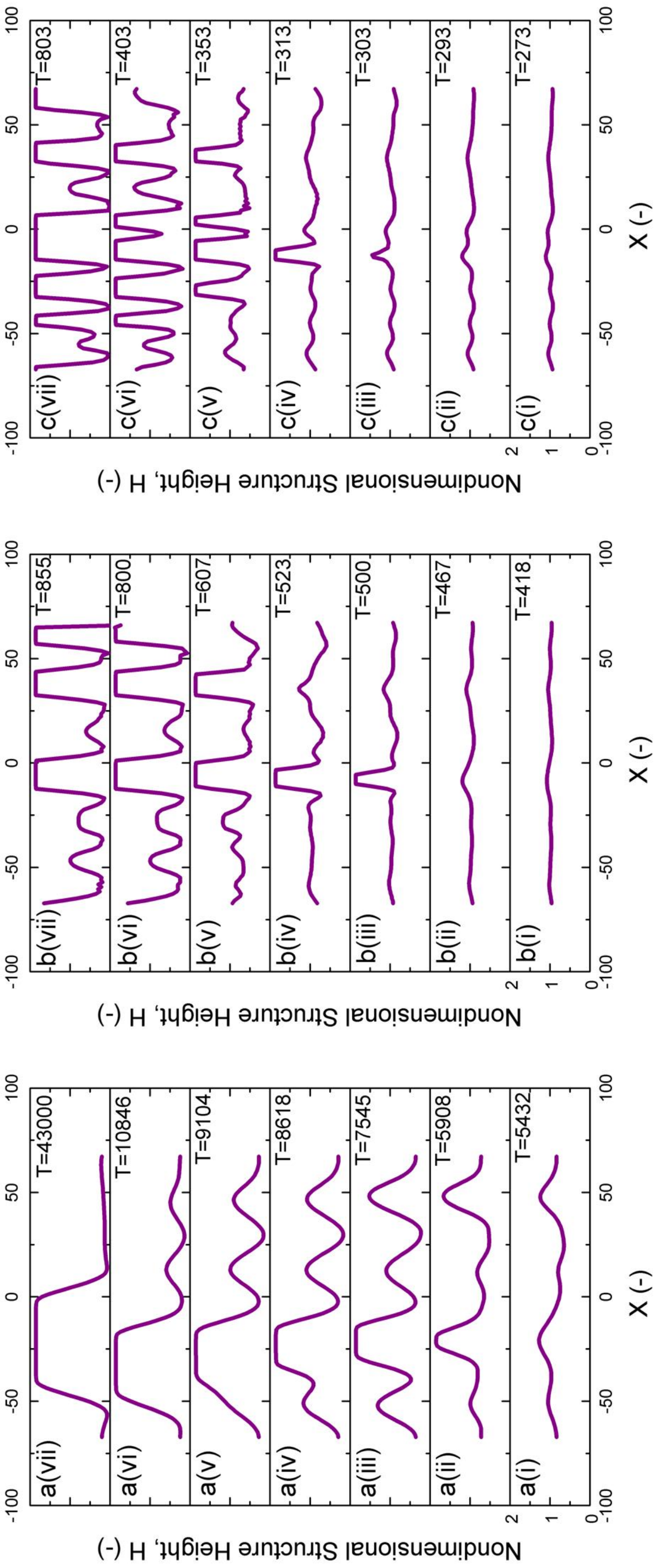

Figure 4.13: 1-D spatiotemporal evolution of 50 nm initial thick at $Y = 0$. (a) PD film and IL films with (b) M= 0.0001 and (c) M= 0.001 mol/L

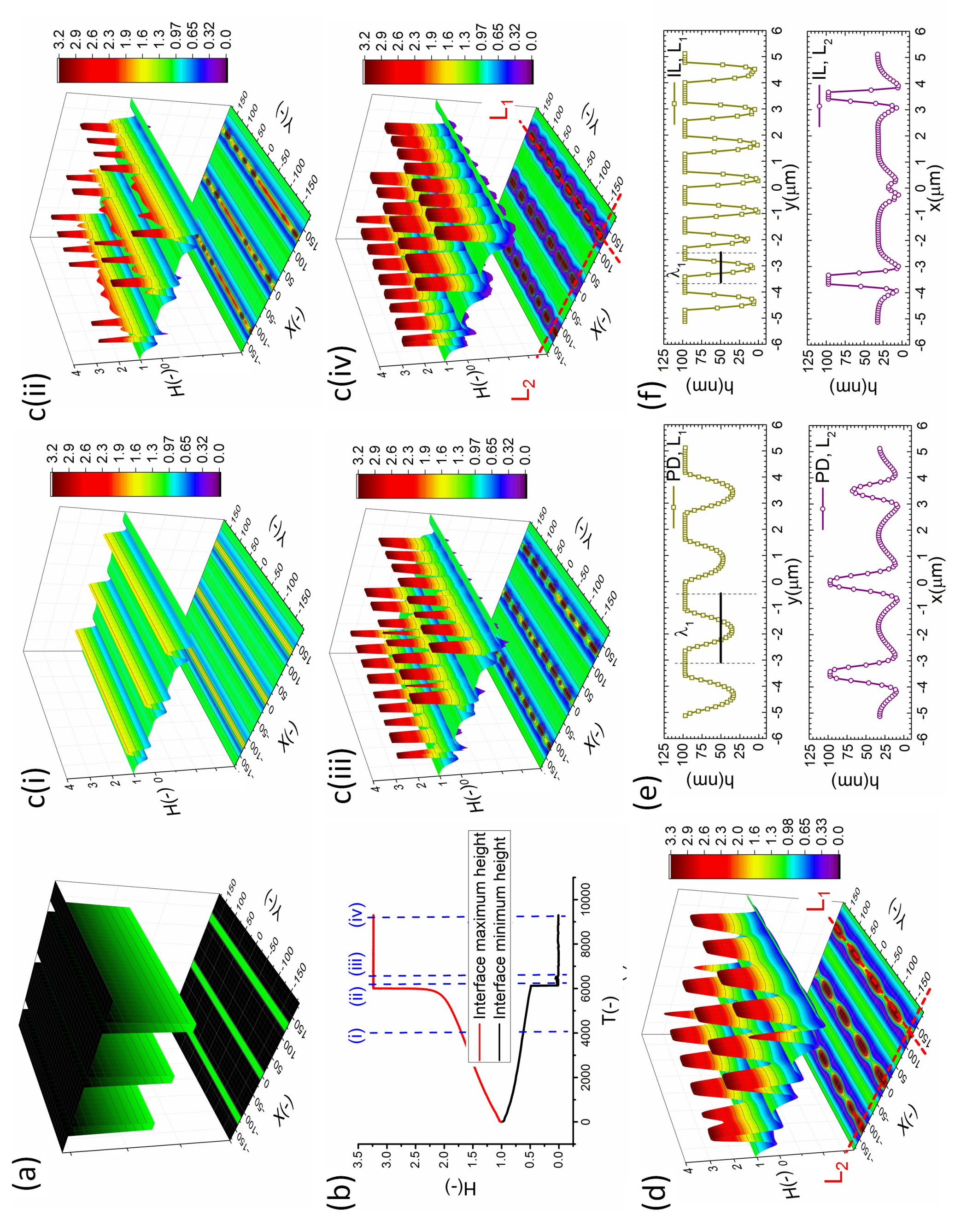

Figure 4.14: (a) 3-D schematic of upper electrode pattern, (b) nondimensional maximum and minimum interface height variations versus nondimensional time, c(i-iv) stages for time evolution of IL film patterns (d) 3-D snapshot of pattern formed in PD film, cross-sectional height profile of features in (e) PD and (f) IL film. Nondimensional times are: T= c(i) 4021, c(ii) 6175, c(iii) 6584, c(iv) 9231. Mean initial film thickness, $h_0 = 30$ nm. $d_1 = 188$ nm, $d_2 = 100$ nm, $W_1 = 3.52$ μm, $W_2 = 0.64$ μm and $V = 20$ V.

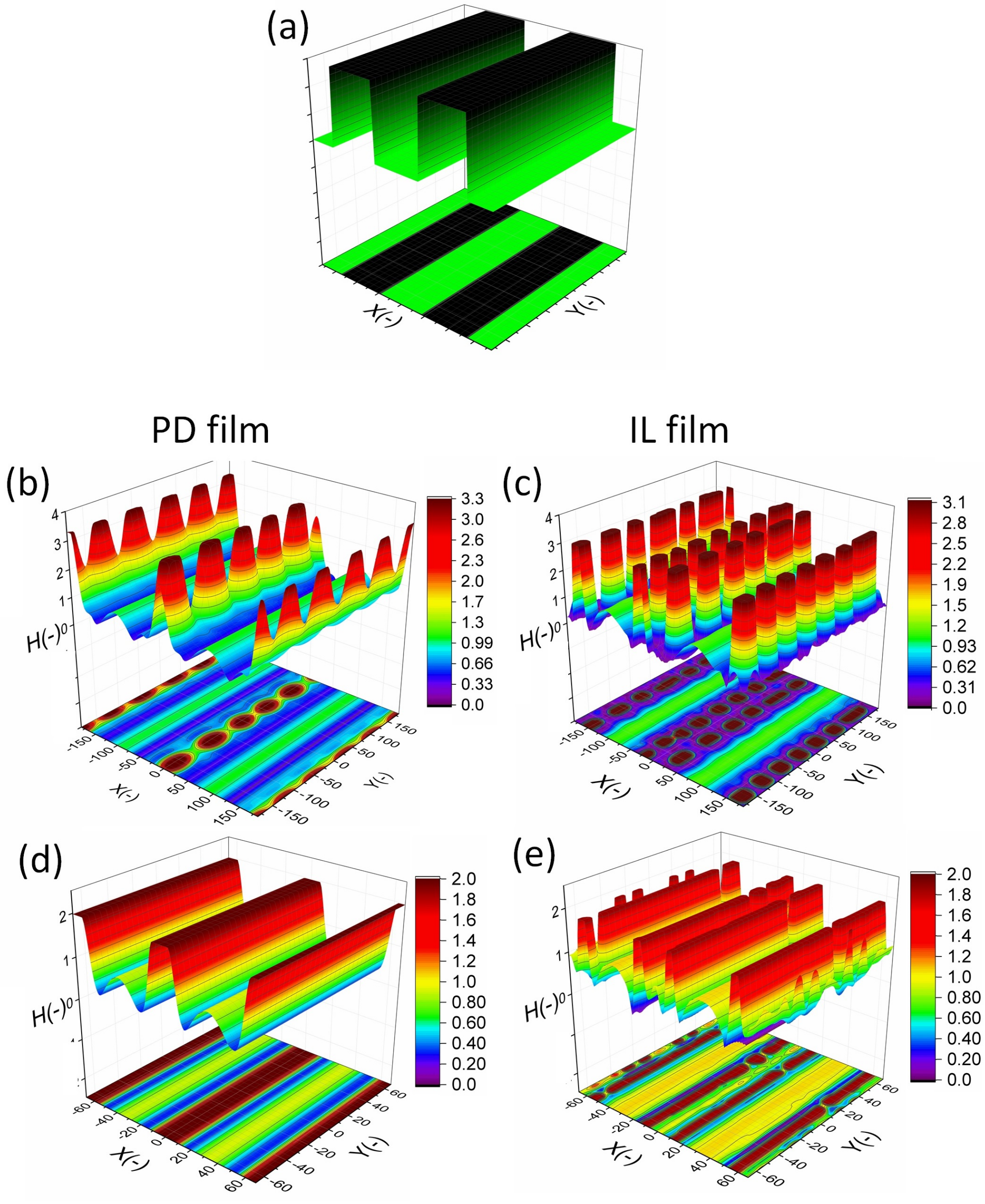

Figure 4.15: (a) 3-D schematic of upper electrode pattern and 3-D snapshots of the interface height of (b and d) PD films, (c and e) IL films. Mean initial film thicknesses, h_0 are (b and c) 30 and (d and e) 50 nm. $d_1 = 188$ nm, $d_2 = 100$ nm, $W_1 = W_2 = 2.46$ μm and $V = 20$ V.

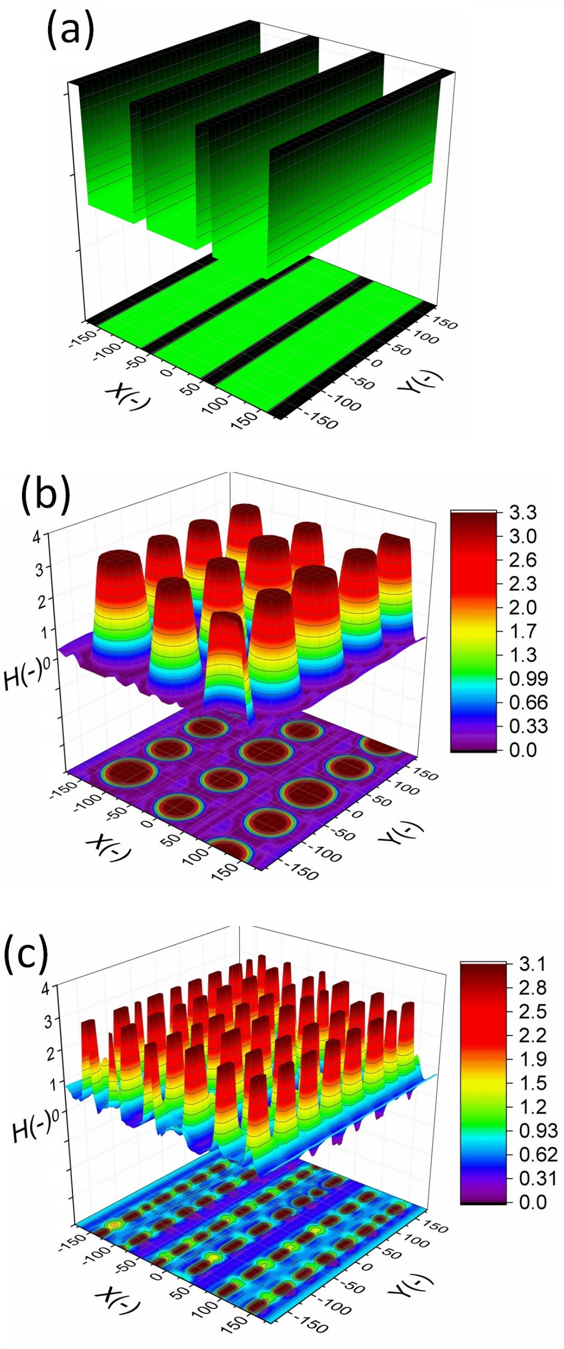

Figure 4.16: (a) 3-D schematic of upper electrode pattern and 3-D snapshots of the interface height of (b) PD film, (c) IL film. Mean initial film thicknesses, h_0 is 30 nm. $d_1 = 188$ nm, $d_2 = 100$ nm, $W_1 = 0.64$ μm, $W_2 = 2.46$ μm and $V = 20$ V.

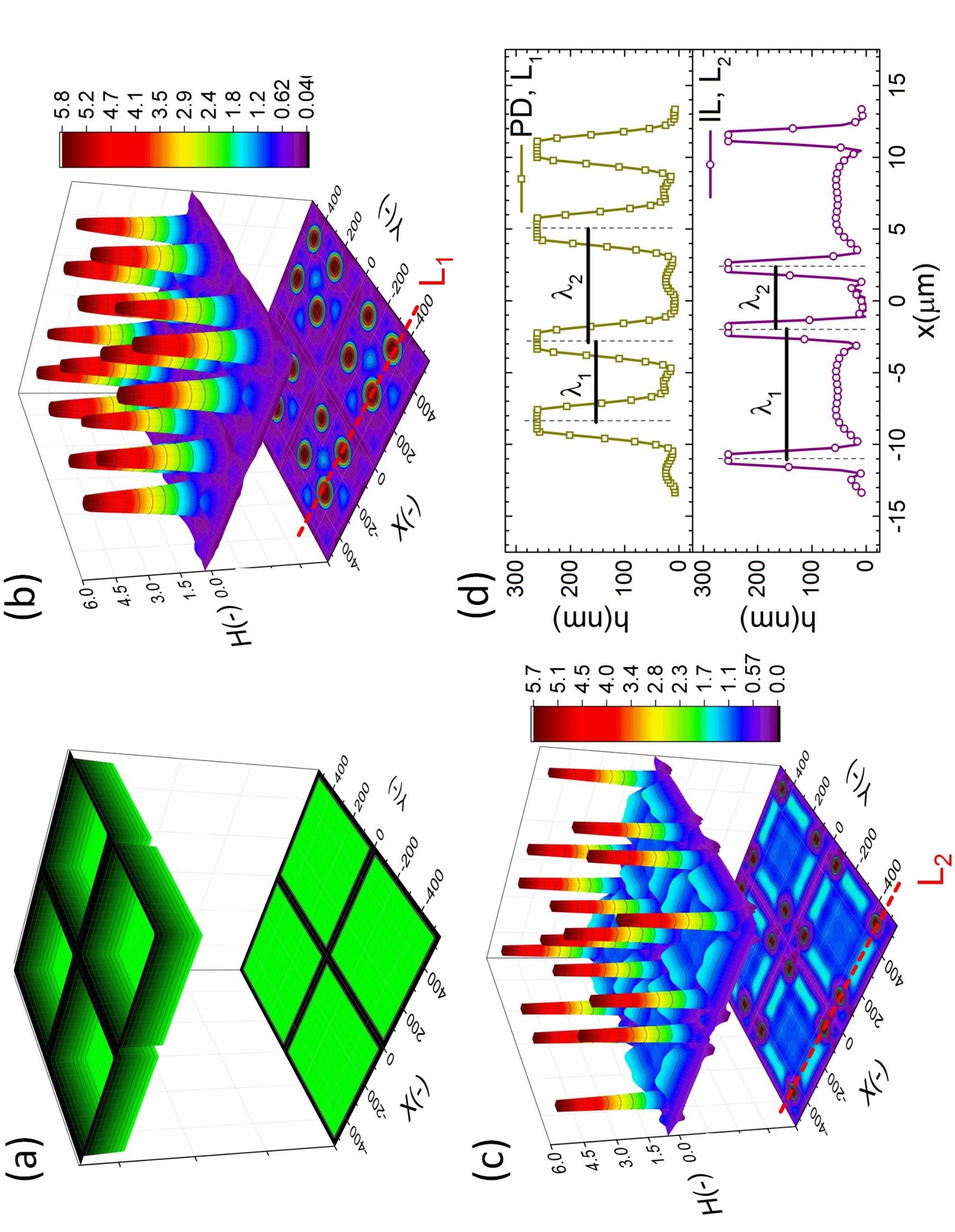

Figure 4.17: (a) 3-D schematic of upper electrode pattern (b) 3-D snapshots of the interface height of (b) PD (c) IL film and (d) cross-section height profile. $h_0 = 45$ nm, $d_1 = 300$ nm, $d_2 = 250$ nm, $V = 10$ V, $\varepsilon_1 = 2.6$ and $\gamma = 0.038\ \frac{N}{M}$.

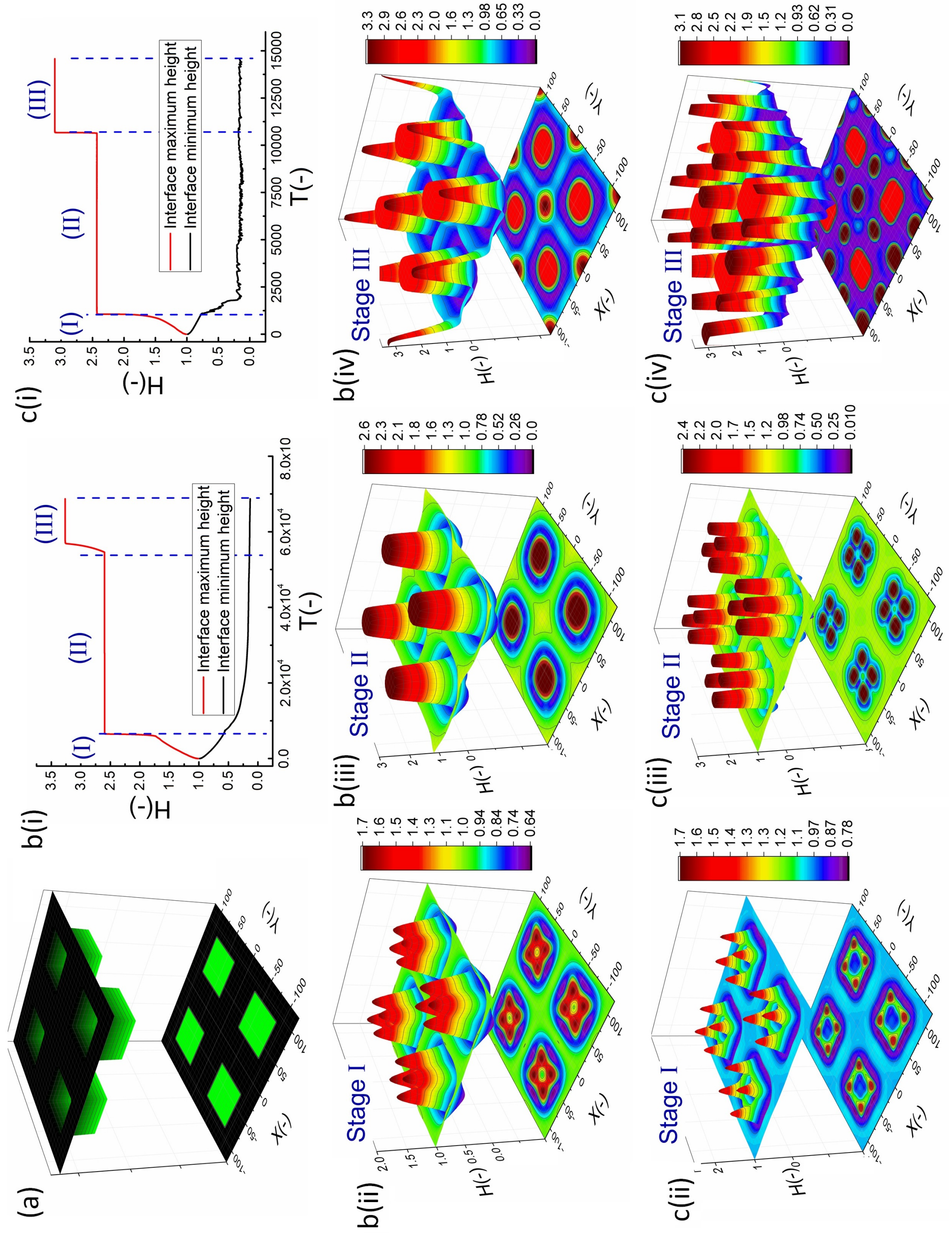

Figure 4.18: (a) 3-D schematic of upper electrode pattern and interface height profile of (b) PD and (c) IL film. (i) Maximum and minimum interface height profile over time and (ii-iv) 3-D snapshots of the formed structure on the thin film from stage i to iii. Nondimensional times are: T= b(i) 5100, b(ii) 20550, b(iii) 60021 and c(i) 1000, c(ii) 2000, c(iii) 3000. Mean initial film thicknesses, h_0 is 30 nm. $d_1 = 100$ nm, $d_2 = 80$ nm, $W_1 = W_2 = 0.84$ μm and $V = 20$ V.

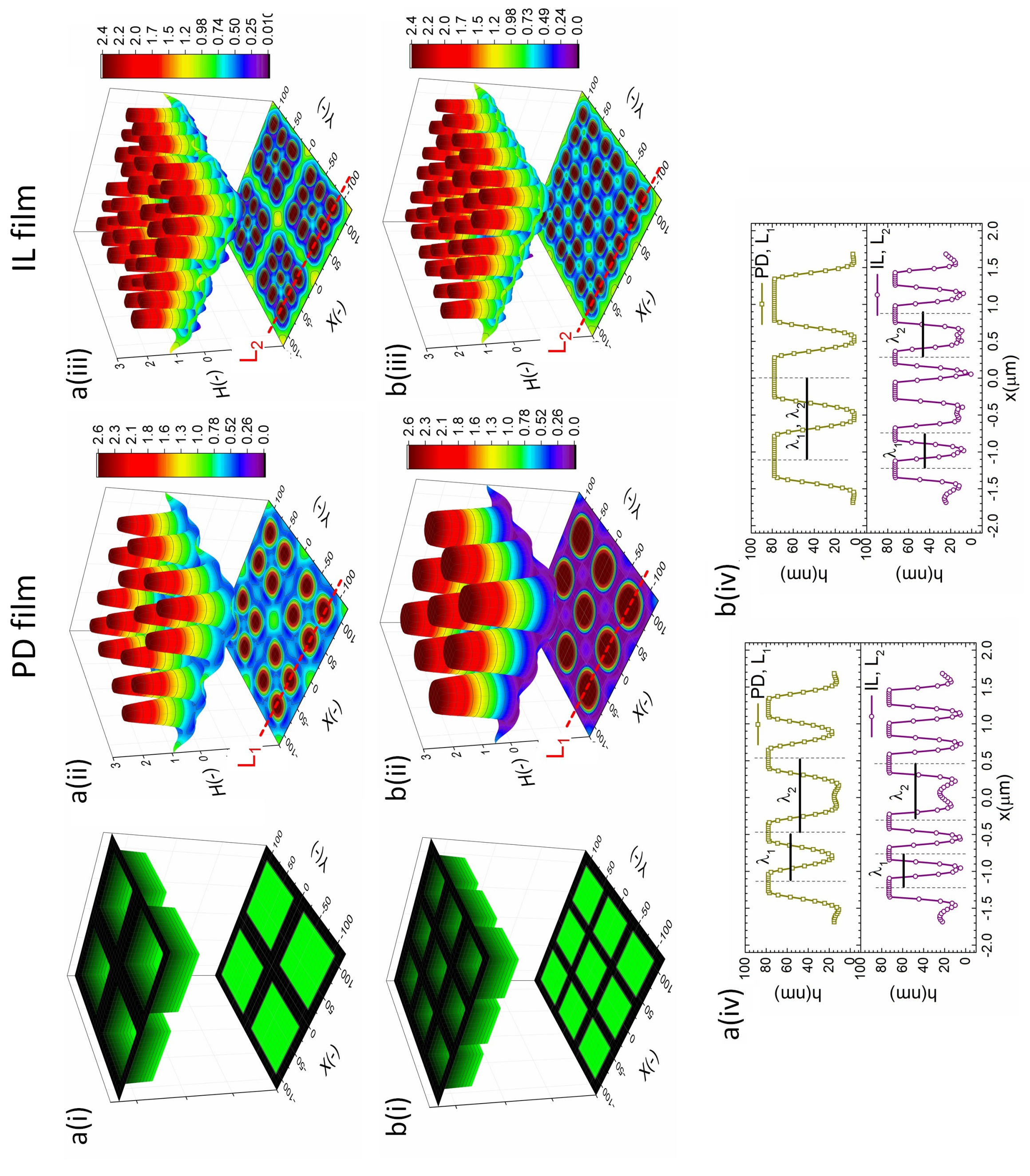

Figure 4.19: (i) 3-D schematic of upper electrode pattern, 3-D snapshots of the formed structure at quasi-steady stage on the thin (ii) PD and (iii) IL film and (iv) cross-section height profile along lines L_1 and L_2. Mean initial film thicknesses, h_0 is 30 nm. $d_1 = 100$ nm, $d_2 = 80$ nm, and $V = 20$ V. Upper electrode pattern dimensions are: (a) $W_1 = 0.42$ μm and $W_2 = 1.26$ μm (b) $W_1 = 0.21$ μm and $W_2 = 0.84$ μm.

Chapter 5

Electrohydrodynamic patterning of bilayers: Role of ionic conductive layer †

In linear stability (LS) analysis, λ_{max} is a function of electric permittivity of layers ε, electrode distance d, initial mean film thickness h_0, applied voltage V and interfacial tension γ [23, 82, 83]. If the air gap between the film and the upper electrode is filled with other medium, the system is called bilayer. Bilayers with electric permittivity ratio of layers $\varepsilon_r = \frac{\varepsilon_{\mathbf{film}}}{\varepsilon_{\mathbf{bounding\ layer}}} > 1$ have been widely studied both numerically [82, 88, 89, 93, 144] and experimentally [1, 23, 83, 145–147]. However, bilayers with $\varepsilon_r < 1$ have received less attention despite their potential for producing smaller features as demonstrated by experiments [1, 83]. Dynamics and spatiotemporal evolution of perfect dielectric (PD) and leaky dielectric (LD) bilayers which are bounded with air are numerically modeled for both flat and patterned electrodes [100, 148]. It has been experimentally shown that the use of an ionic liquid (IL) bounding layer results in sub-micrometer sized features even with the use of flat electrodes [1].

In chapter 4 is shown that in the EHD patterning of nanofilms, considering finite diffuse layer of free ions/charges significantly affects the shape and size of the structures form on the interface.

In this chapter, more comprehensive model based on the coupled nonlinear Poisson-Boltzmann and Laplace equations is developed to obtain the electric potential distribution within layers and consequently the electrostatic pressure acting on the interface in bilayer. Analytical calculations are performed and

---

†Parts of this chapter is based on Refs. [2] and [6], see Appendix C-1

integrated into the numerical simulation to obtain the interface potential and to define an electrostatic component of conjoining/disjoining pressure acting on the interface. The morphology of film and its drainage time under the effects of filling ratio and electric permittivity ratio are studied. Finally, the perfect dielectric (PD) upper layer is replaced with IL layer to investigate spatiotemporal behavior of the bilayer.

Since the bilayer interface potential is a function of interface location, applied voltage, electric permittivity of layers and the Debye length (eqn. 3.26), changing any of these parameters changes the interface potential and the electrostatic component of conjoining pressure and consequently shape and size of the structures. The simulation parameters and constants used in this study are listed in Table 6.1.

Table 5.1: Constants or parameters used in simulations.

Parameter	Value
electric permittivity of the liquid film (ε_1)	2.5 [$-$]
electric permittivity of the bounding media (ε_2)	1$-$36 [$-$]
molarity (M)	0.01$-$1 [$mmol/L$]
initial film thickness (h_0)	$20-85$ [nm]
electrodes distance (d)	100 [nm]
Born repulsion cut off distance (l_0)	1$-$8 [nm]
applied voltage (ψ_{up})	0.25$-$70 [V]

5.1 Electrostatic interaction

The use of an external electric field induces instabilities on the deformable film interface to create a variety of structures from simple hexagonal ordered columns, the bicontinuous and holes [1, 23, 59, 82–84, 93, 96, 99, 100, 145–147, 149, 150] to the more complex ones such as cage-like [101], hierarchical [102], core-shell and embedded [103] structures. The film interface structure changes under a homogeneous electric field based on the relative electric permittivity difference of layers which determines the net electric force direction. Referring to eqn. 3.15, for the case of $\varepsilon_1 > \varepsilon_2$ ($\varepsilon_1 < \varepsilon_2$) the electrostatic force acts upward (downward) which results in a disjoining (conjoining) pressure (ϕ_{EL}).

In ionic liquids, migration and redistribution of free ions result in double layer formation close to the interface. This accumulation of ions alters the electric potential distribution within the IL layer and depends on the ionic strength which is characterized by the Debye length, κ^{-1}. The conductivity of ionic liquids increases with high molarity and lower Debye length. The analytical solution eqns. 3.24 and 3.25 are examined for three values of molarity in the IL-PD bilayer and results are compared to the electric potential distribution in a PD-PD bilayer in figure 5.1(a). Electric permitivity ratio, $\varepsilon_r = 0.6$, and applied potential, $\psi_{up} = 0.25\ V$, are kept constant.

Ionic liquids with higher molarity, $M = 1\ mmol/L$ (lower Debye length $\kappa^{-1} = 1.08\ nm$) act like perfect conductors and electric potential decreases slightly near the interface whereas potential drop close to the interface is more significant when the ionic strength is lower, $M = 0.01\ mmol/L$ (higher Debye length, $\kappa^{-1} = 10.8\ nm$). For the PD film, as expected from solution of Laplace equation, electric potential decreases linearly near zero at the lower electrode (see figure 5.1(a)). The proposed analytical solution, eqns. 3.25 and 3.26, gives reasonable results for ionic liquids with $M \geq 0.01\ mmol/L$ (i.e. $\kappa^{-1} \leq 10.8\ nm$). The maximum growth rate, s_{max} and its corresponding maximum wave number, κ^*_{max} are found for IL-PD bilayers from LS analysis. Growth rate as a function of wave number for IL-PD and PD-PD bilayers are compared in figure 5.1(b). The maximum wave number is increased when the PD bounding layer is replaced with the IL one which results in lower maximum wavelength, λ_{max}, resulting in smaller center to center distance of pillars [23]. As shown in figure 5.1(a), higher ionic strength leads to lower electric potential drop within IL layer. Therefore the lower layer film experience a higher electric field. Consequently a IL-PD interface is subject to higher electrostatic pressure, ϕ_{EL} (eqn. 3.27). Effects of electrolytes molarity on the net electrostatic pressure acting on the IL-PD interface for two electric permittivity ratio of layers, $\varepsilon_r = 0.6$ and 2.5 are shown in figure 5.2(a). In all cases, the magnitude of electrostatic pressure decays as the interface height increases. The negative values for ϕ_{EL} represent the upward disjoining pressure and positive values are downward conjoining pressure.

The effects of relative electric permittivity ratios of the fluid layers in PD-PD bilayers on the electrostatic conjoining/disjoining pressure is presented in figure 5.2(b). In this case the applied potential, $\psi_{up} = 20\ V$, is 80 times greater than that used for the IL-PD bilayers (figure 5.2(a)). Comparing ϕ_{EL} values for $\varepsilon_r = 0.6$ and 2.5 between IL-PD bilayers and PD-PD bilayers show that electrostatic pressure varies more uniformly with change of interface height in PD-PD bilayers. Using bounding layers with high relative electric permittivity in PD-PD bilayers also leads to higher electrostatic pressure with similar exponential decrease as a function of interface height to IL-PD bilayers. Although the applied potential is 80 times smaller in IL-PD case, the interface experience higher electric pressure even without considering the change in molarity.

When the spinodal parameter (derivation of conjoining pressure with respect to the film thickness) becomes negative, the film becomes unstable. For the PD-PD bilayers (eqn. 3.15), both cases $\varepsilon_1 > \varepsilon_2$ and $\varepsilon_1 < \varepsilon_2$ result in negative spinodal parameter values. However for the IL-PD bilayers (eqn. 3.27), the spinodal parameter is negative only for bilayers with $\varepsilon_1 < \varepsilon_2$. Therefore, this study focuses on the unstable case, where the upper layer has a higher electric permittivity than the lower layer ($\varepsilon_1 < \varepsilon_2$).

Variation in electrostatic pressure due to change in applied potential for PD-PD and IL-PD bilayers are presented in figure 5.3. To show the broad range of variations in ϕ_{EL}, results are plotted on a log-log scale. An electric permittivity ratio of $\varepsilon_r = 0.6$ and the IL layer molarity of $M = 0.1\ mmol/L$ ($\kappa^{-1} = 3.43\ nm$) are constant. The IL-PD interfaces is subject to a much higher electrostatic pressure compared with the PD-PD interface (in the order of 10^3 to 10^7 times higher for the $\psi_{up} = 10\ V$ case).

IL-PD bilayers are unstable under applied electric field while $\varepsilon_r < 1$. To investigate this response, PD-PD bilayers with $\varepsilon_r < 1$ are first considered by calculating the dynamics and resulting spatiotemporal evolution of interface. This provides a basis of comparison for unstable IL-PD bilayers in the subsequent step.

5.2 Perfect dielectric - Perfect dielectric bilayers

Bilayers with $\varepsilon_r < 1$, which act like perfect dielectric materials (i.e. there is no free charge or free ion in media) are examined first as a baseline for comparison to IL-PD bilayers. Electric breakdown in layers is not included in the simulations and it is assumed that the film layers behave like perfect dielectrics during the patterning process. The applied voltage, ψ_{up} is set to a low value (20 V) but even at this low applied voltage the expected electric field within the layers may exceed the dielectric field strength of the material and resulting in electric breakdown violating the model assumption [1].

A 2-D spatiotemporal evolution and 3-D snapshots of the liquid-liquid interface instabilities for the homogeneous electric field and PD-PD bilayer with $\varepsilon_r = 0.6$ is shown in figure 5.4. Initial mean film thicknesses (h_0) are a(i-iv) 20 nm, b(i-iv) 50 nm, c(i-iv) 70 nm and d(i-iv) 85 nm. The electrostatic conjoining pressure pushes the interface downward, so some hollows in the lower layer are expected to form. Negative diffusion [82] moves the fluid from the thinner to the thicker region which assists in the growth of instabilities over time. Four distinct structures of: pillars a(iv), bicontinuous b(iv), holes c(iv) and roll-like d(iv) are observed. Similar to the bilayers with $\varepsilon_r > 1$ [82, 93], pillars and bicontinuous structures form in PD-PD systems. However, holes and roll-like structures only form when there is a conjoining pressure for $\varepsilon_r < 1$ [83, 84].

Pillars which have a hexagonal structure in figure 5.4 a(ii), imply the coalescence of the neighboring pillars a(iii) is due to their collision [96]. Bicontinuous structures, b(ii) and b(iii), behave like an air-in-liquid dispersion which occurs in air-polymer (i.e. monolayer) system with high filling ratios [82]. For hole formation the interface touches the upper electrode in the early stages of process, figure 5.4 c(i), with dumbbell shape dents on the interface. These dents evolve into round shapes with time and deepen toward the lower electrode, figure 5.4 c(ii). Compared to the pillars, figure 5.4 a(ii), the holes, figure 5.4 c(ii), do not have a hexagonal order over the domain, therefore Ostwald ripening [96] is one possible reason for the coalescence of neighbor holes over time. Roll-like or a straight groove type structures seem to be an organized form of the bicontinuous structures generated by the same phase inversion mechanism. Images in figure 5.4 a-d (ii) show the quasi-equilibrium structures and a-d (iii) which are snapshots for the coalescence stage. The time that patterns remain in the quasi-equilibrium condition depends on physical parameters of the system like viscosity, electric permittivity ratio of layers and initial mean thickness [82, 93, 96]. To characterize different morphological behaviors in bilayers with $\varepsilon_r = 0.6$ and different thicknesses, as shown in figure 5.4, a systematic numerical investigation is performed. A parametric map that captures the liquid-liquid interface structure for wide ranges of relative electric permittivity ratios of layers, ε_r, and nondimensional initial mean film thickness, h_0/d is shown in figure 5.5. Both initial layer thickness and electric permittivity ratio are critical factors in the EHL process and can create different patterns on the film. When the lower layer is thicker than the upper layer, the final pattern is more sensitive to electric permittivity. Changing the electric permittivity ratio of the bilayers, results in the interfaces having two to four different kinds of structure depending on the layers initial thicknesses. For example, in case of $\varepsilon_r = 1.5$ pillars and bicontinuous structures will form when $h_0/d = 0.2$ and 0.7, respectively (see figure 5.6 a(i-iii)). But for $\varepsilon_r = 0.3$ pillars, bicontinuous and holes structures are observed for h_0/d ratios of 0.35, 0.5 and 0.6, respectively (see figure 5.6 b(i-iii)). Moreover, the interface can have four distinct structures, namely pillars, bicontinuous, holes and roll-like where $\varepsilon_r = 0.6$ and h_0/d ratios of 0.2, 0.6, 0.7 and 0.85, respectively.

From a thermodynamic point of view, the final structure in the pattern formation process is the shape that is in the lowest Helmholtz free energy of the system which is in a thermodynamically stable state condition. In figure 5.5, a critical initial film thickness for each ε_r can be found such that EHD patterning process of films with initial thicknesses below this critical value results in pillar formation. The critical film thickness is called the Maxwell point [24, 84] which is the inflection point in the plot of conjoining/disjoining pressure versus interface height in the steady state solution [84]. Varying the relative electric permittivity ratio of the layers changes the conjoining/disjoining pressure (see figure 5.2) which results in a shift to the critical film thickness value.

In some cases, structures do not last for a long time. Particularly for patterns that are close to the boundaries between different structures in figure 5.5. Filled triangles in figure 5.5 denote the unstable pillars which coalesce quickly and form bicontinuous structures. These are bounded between stable pillars and bicontinuous structures. Examining figure 5.5 carefully, it is found that as the mean initial thickness of the layers is varied (h_0/d), more types of structures are produced when $\varepsilon_r < 1$ compared to $\varepsilon_r > 1$.

The effect of relative electric permittivity ratios of layers, ε_r, on the nondimensional maximum and minimum film thickness, h_{max}/d and h_{min}/d, over nondimensional time, T for three polymer film thicknesses of 20, 50 and 70 nm is shown in figure 5.7. Four values of ε_r (a) 0.1, (b) 0.6, (c) 1.5 and (d) 2.5 are chosen to compare the bilayers behavior for $\varepsilon_r > 1$ and $\varepsilon_r < 1$. The parameter h_{min} indicates when the lower layer drains (or non-wet the lower electrode) and h_{max} indicates when the lower layer touches the upper electrode in the domain. To compare bilayers with different thicknesses, interface height, h is nondimensionalized using electrode distance as a length scale. The actual time in real experiments depends on the properties of the applied materials, mainly viscosity [96]. For bilayers with $\varepsilon_r < 1$, thicker films drain faster than thinner ones as shown in figure 5.7(a) and (b), similar trend is found for the bilayers with $\varepsilon_r > 1$ shown in figure 5.7(c) and (d).

5.3 Ionic liquid - Perfect dielectric bilayers

When IL-PD bilayers are considered, it has been found that the interface experiences a higher electric field. The electrostatic model and corresponding electrostatic pressure derived earlier are used in the thin film equation to examine the spatiotemporal evolution of IL-PD interface. The electric permittivity ratio of bilayer is set to $\varepsilon_r = 0.6$, and other physical parameters are kept the same as PD-PD bilayers for comparison purpose. Three bilayers cases, with initial mean lower layer thickness (h_0) of $20,\ 50$ and $70\ nm$, are simulated and the 2-D spatiotemporal evolution and 3-D snapshots are shown in the figure 5.8.

For the IL-PD cases in figure 5.8, a homogeneous electric field is applied in a $(4 \times 4)\lambda^2$ domain at $\varepsilon_r = 0.6$ and $M = 100\ mmol/L$. In the IL-PD case with a $20\ nm$ lower layer initial thickness (figure 5.8(a)), pillars form on the interface similar to the PD-PD system (figure 5.4(a)). However, the generated pillars are more sparsely spread and have elliptical cross-section instead of a circular. Increasing h_0 to $50\ nm$ causes the IL-PD to switch to polydisperse holes (figure 5.8 b(ii)). In the PD-PD bilayer a bicontinuous structure (figure 5.4b(ii)) is formed at $h_0 = 50\ nm$, which is unlike the similar condition IL-PD bilayer holes (figure 5.8 b(ii)). A further increase in h_0 to $70\ nm$ in IL-PD case leads to the generation of more organized holes (figure 5.8 c(ii)). Thus using an ionic liquid, in place of a perfect dielectric, seems to effectively causes a shift to the left in the boundaries between structure types in figure 5.5.

The disordered and polydispersed pillars of the IL-PD system which are captured in the numerical simulation are also experimentally observed [1]. Thus the numerical simulation developed here in predicting the interface behavior in IL-PD system seems to capture the dynamics of interest. A 2-D spatiotemporal evolution for liquid-liquid interface instabilities for the homogeneous electric field in (a) PD-PD and (b) IL-PD bilayer are directly compared in figure 5.9. The number of pillars in the IL-PD bilayer is more than what is immediately apparent in figure 5.9 since the physical domain size in IL-PD is 10 times less than the PD-PD (compare images a(ii) and b(ii)). Specifically, the average center-to-center distance of pillars is 210 nm for the IL-PD bilayer compared to 1336 nm for the PD-PD bilayer, quantifying the smaller size features in the IL-PD bilayers for this case.

5.4 Summary

Electrostatic force is used as a destabilizing external force to study the dynamics, morphological evolution and drainage time of thin liquid bilayers ($< 100\ nm$). Due to the geometrical properties of the system (small aspect ratio of mean film thickness to lateral domain) a long-wave asymptotic theory is employed to simplify the coupled mass and momentum equations. This results in a nonlinear thin film equations approximation which is numerically solved. The generated thin film fluid structures of an IL-PD bilayers for varying parameters are simulated and compared to the well known PD-PD base case.

In PD-PD bilayers with $\varepsilon_r < 1$, pillars, bicontinuous, holes and roll-like structures are formed, whereas the last two features are not observed in the bilayers with $\varepsilon_r > 1$. When the thin film is thicker than bounding media, the final pattern is more sensitive to electric permittivity ratio. Thicker films are found to drain faster in bilayers with $\varepsilon_r < 1$ similar to bilayers with $\varepsilon_r > 1$.

For IL-PD bilayers, to predict the electrostatic component of conjoining/disjoining pressure acting on the interface, an analytical model is developed based on the nonlinear Poission-Boltzmann equation. Perfect dielectrics and perfect conductors are found as limiting cases for ionic liquids with low and high ionic strength, respectively. The IL-PD interfaces is subject to a much higher electrostatic pressure compared with the PD-PD interface (in the order of 10^3 to 10^7 times higher for the $\psi_{up} = 10\ V$ case). It is found that the IL-PD bilayers with $\varepsilon_r > 1$ remain stable under the action of transverse electric field whereas the similar PD-PD bilayers are unstable.

The use of an IL layer is found to reduce the size of the structures by a factor of ten (λ_{PD-PD} is about ten times larger than λ_{IL-PD}) for the case studied. This has important implication when the goal is to produce small structures. The IL-PD pillars tend to be polydispersed and more disordered over the domain compared to the PD-PD ones. The developed analytical models and resulting numerical simulation closely predicts the interface behavior for both

PD-PD and IL-PD bilayers over the parameters range tested when compared to other numerical studies and experimental observations in the literature. This indicates the developed numerical simulation is of utility in predicting PD-PD and IL-PD bilayer response to an applied electric field.

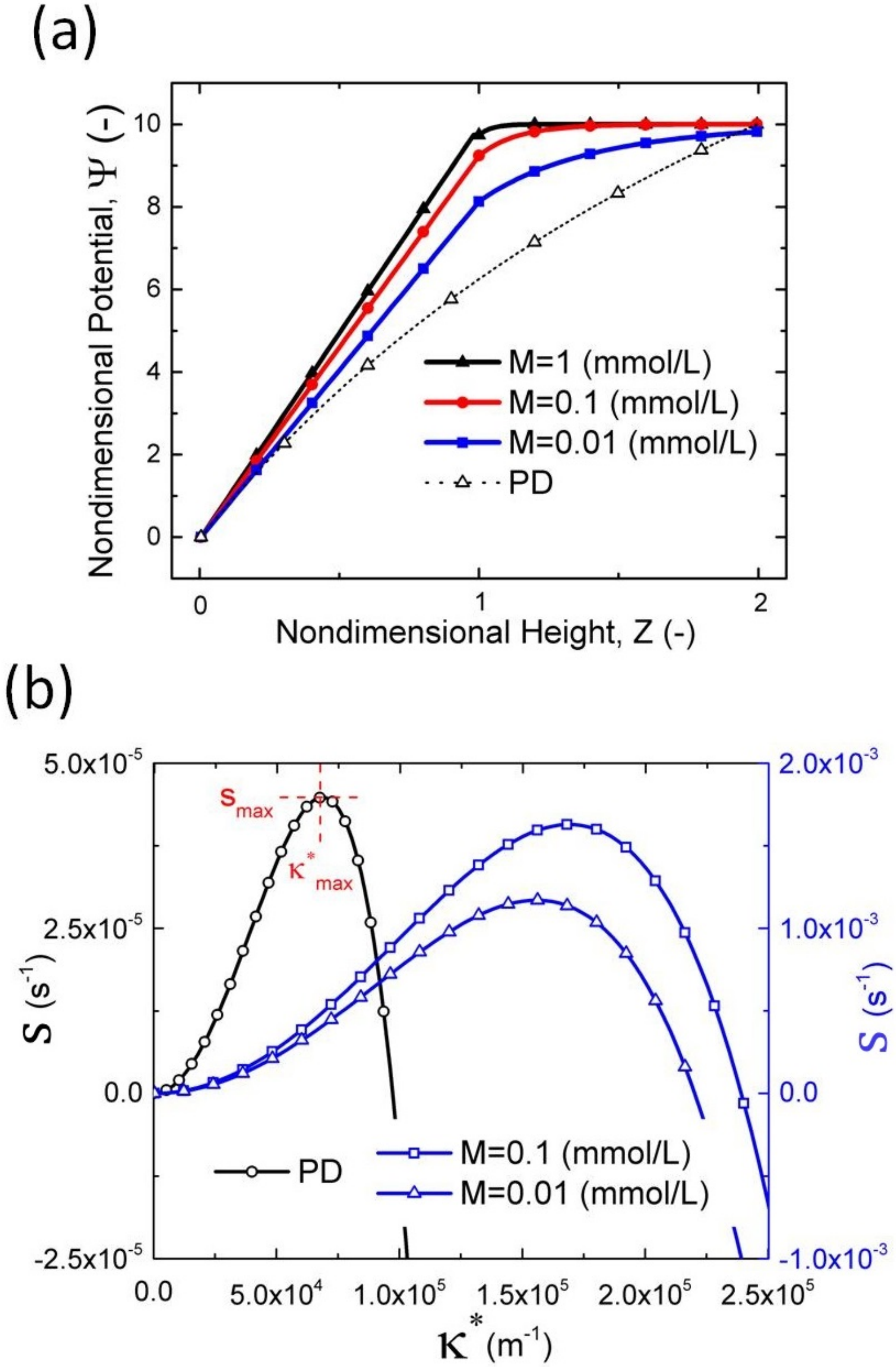

Figure 5.1: Effects of IL layer molarity on (a) nondimensional electric potential, $\Psi = e\psi/k_BT$, variations versus nondimensional height, $Z = z/(d-h)$ and (b) growth rate, s, variations versus wave number, κ^*. $d = 100\ nm$, $h_0 = 50\ nm$, $\psi_{up} = 0.25\ V$, $\varepsilon_1 = 2.5$ and $\varepsilon_2 = 4.17$.

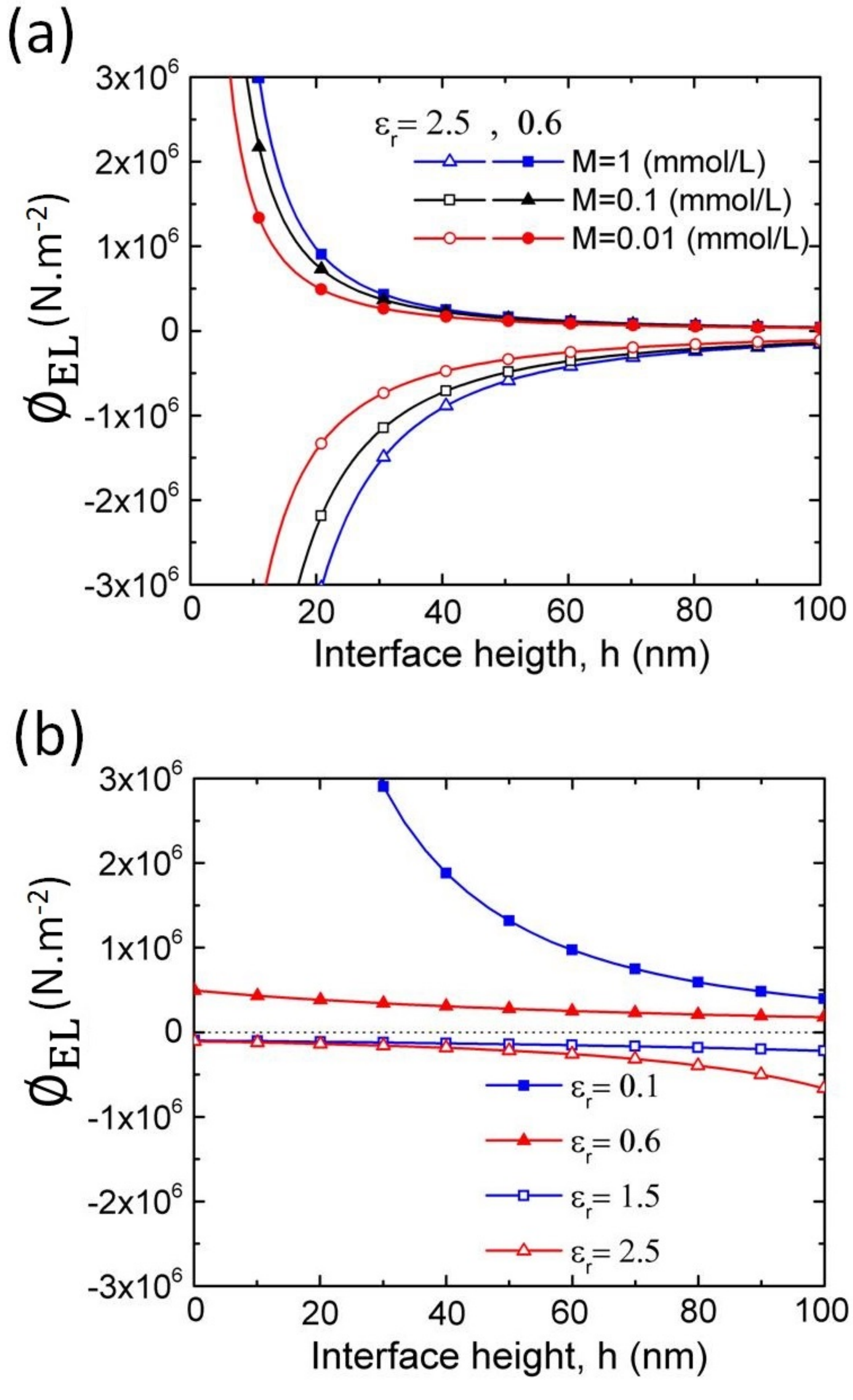

Figure 5.2: Electrostatic pressure variations versus interface height, Effects of (a) electrolyte molarity in IL-PD bilayers, (b) relative electric permittivity ratios of layers in PD-PD bilayers, ε_r. Applied potential, ψ_{up}, is (a) 0.25 and (b) 20 V and $\varepsilon_1 = 2.5$.

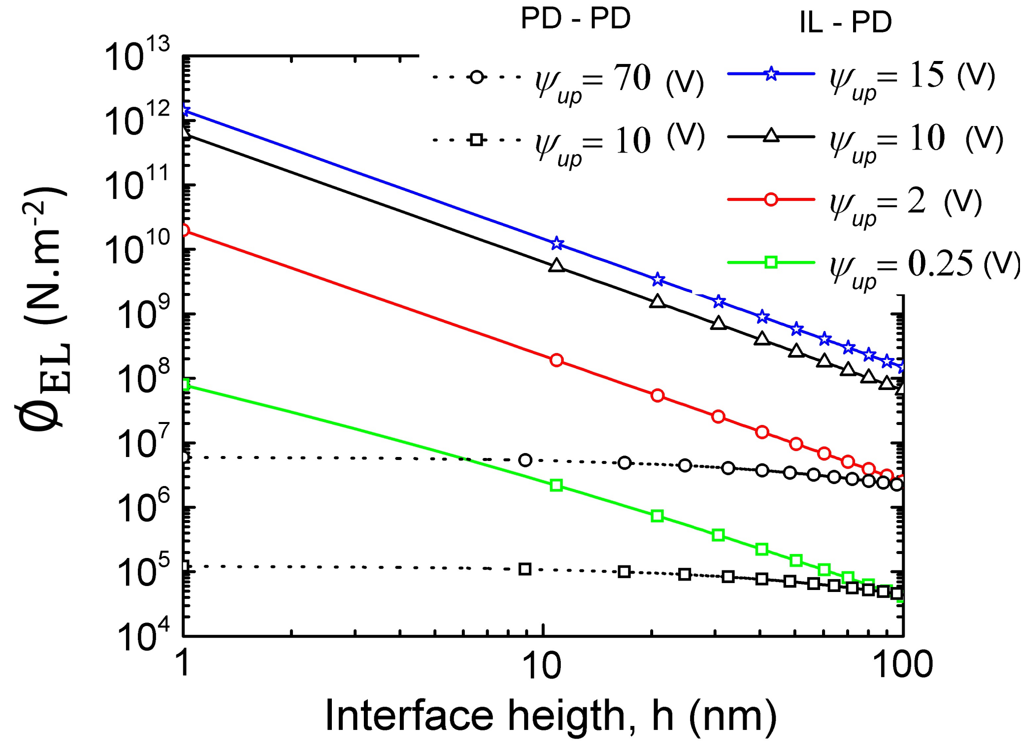

Figure 5.3: Electrostatic pressure variations versus interface height in PD-PD bilayer and IL-PD bilayer, considering applied potential effects. $M = 0.1\ mmol/L$ for IL-PD, $\varepsilon_1 = 2.5$ and $\varepsilon_2 = 4.17$.

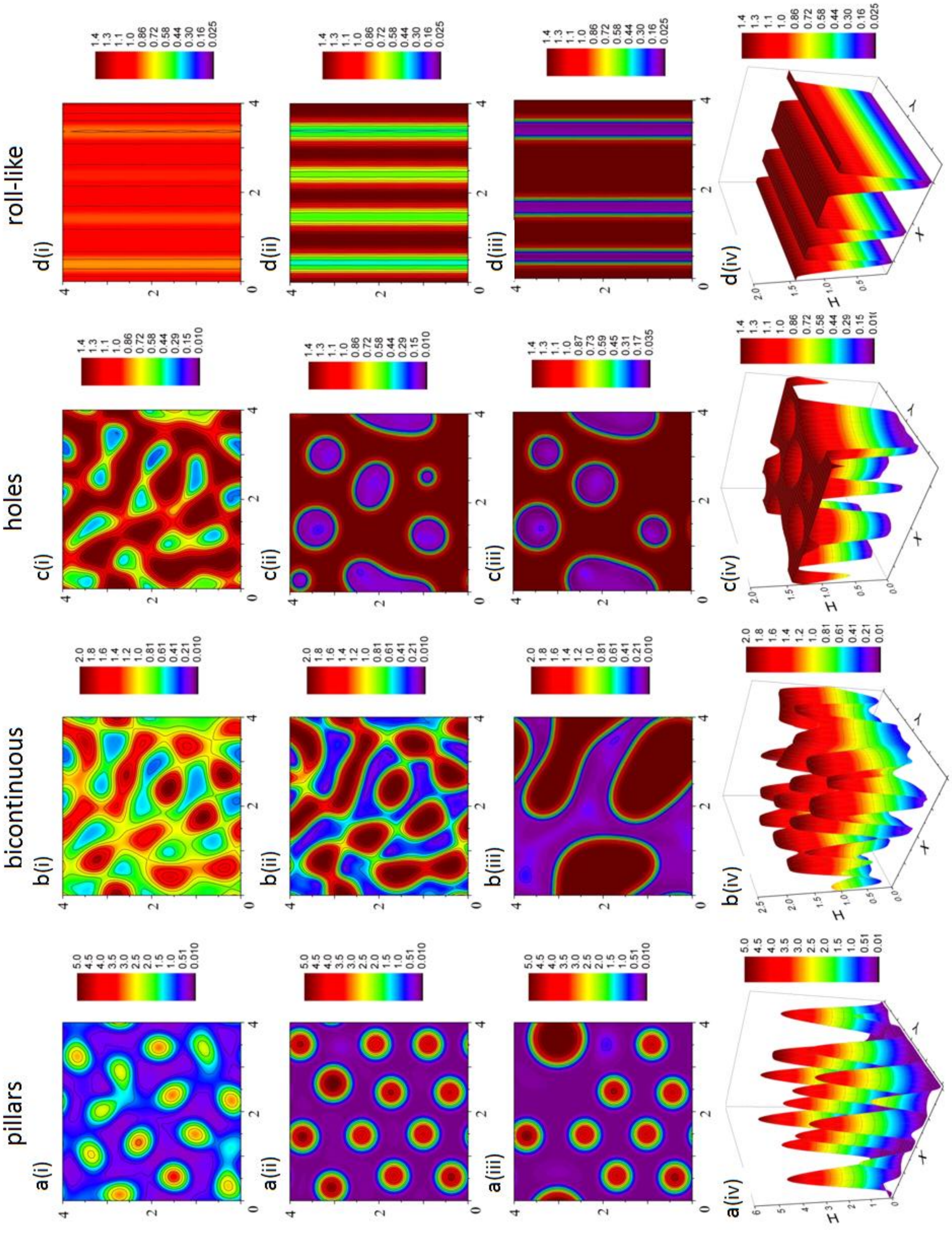

Figure 5.4: Basecase PD-PD bilayer, (a-d) images from i to iii show the 2-D spatiotemporal evolution for liquid-liquid interface instabilities in a $(4 \times 4)\lambda^2$ domain when $\varepsilon_r = 0.6$ and $\varepsilon_1 = 2.5$. Initial mean film thicknesses (h_0) are: a(i-iv) 20 nm, b(i-iv) 50 nm, c(i-iv) 70 nm and d(i-iv) 85 nm. Initial electric field intensities (E_0) are: 294, 250, 227 and 212 MV/m, respectively. Nondimensional times for the 2-D plots are T= a(i) 9×10^4, a(ii) 3.4×10^5 and a(iii) 2.4×10^6; b(i) 8×10^2, b(ii) 1×10^3 and b(iii) 4×10^3; c(i) 2×10^2, c(ii) 6×10^2 and c(iii) 9×10^2; d(i) 1.8×10^3, d(ii) 2.2×10^3 and d(iii) 6.1×10^3. Plots a-d (iv) show 3-D snapshots of the liquid-liquid interface structure. Nondimensional times for the plots are T= a(iv) 3.4×10^5, b(iv) 1×10^3, c(iv) 6×10^2 and d(iv) 6.1×10^3.

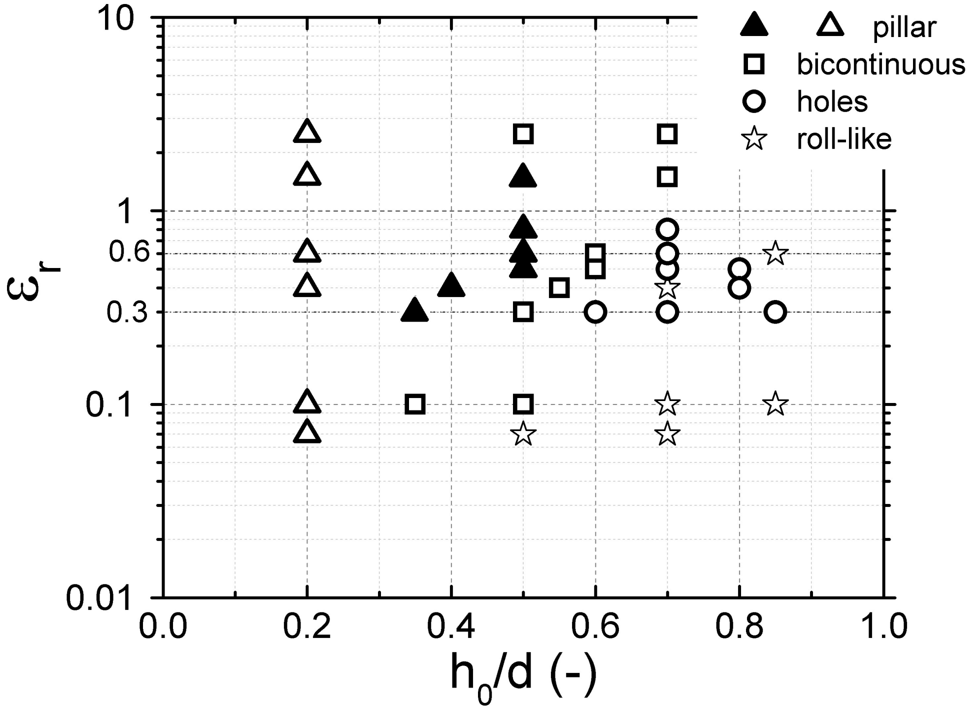

Figure 5.5: 2-D parametric map that illustrates the liquid-liquid interface structure as a function relative electric permittivity ratios of layers, ε_r, and nondimensional initial mean film thickness, h_0/d.

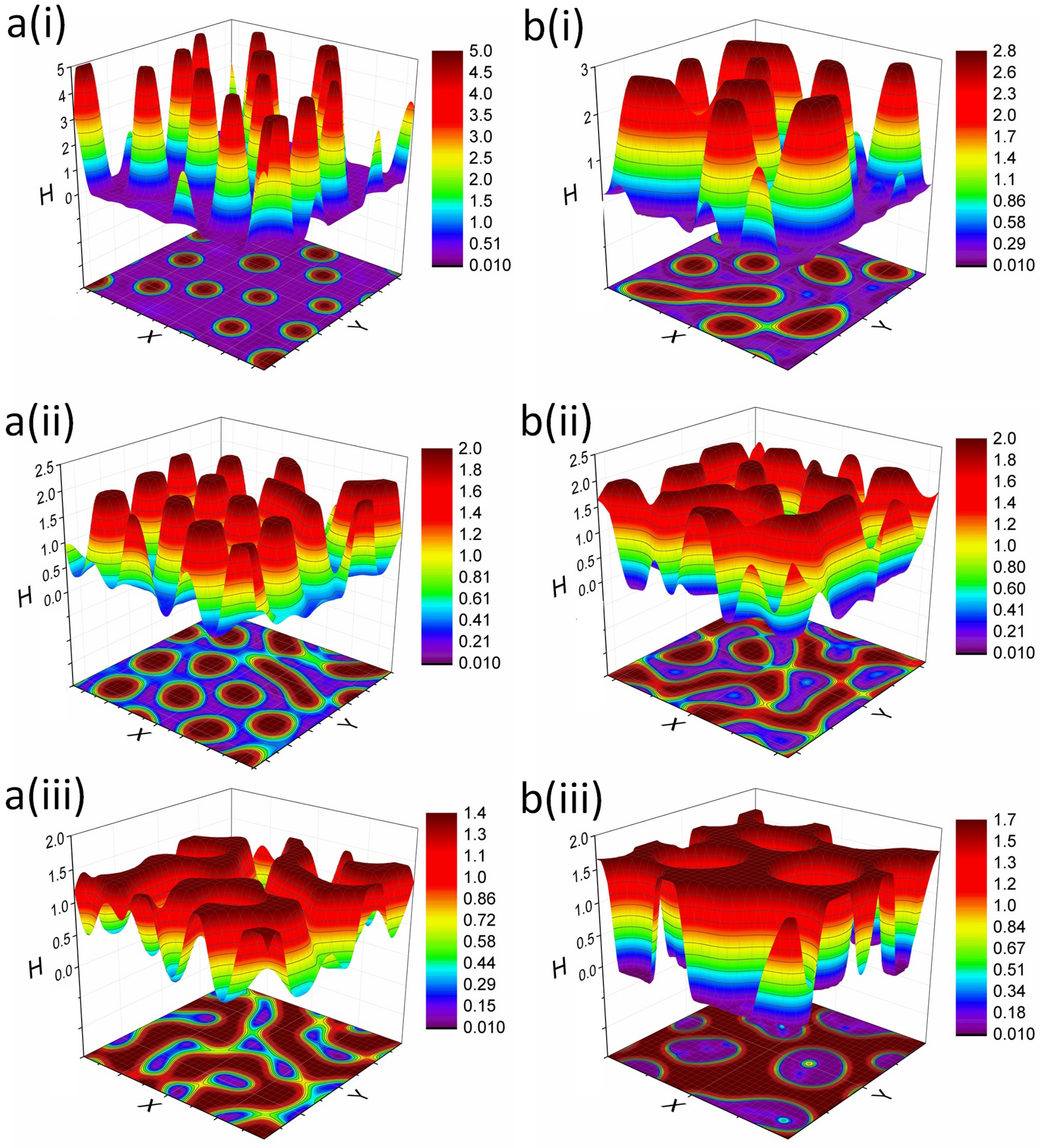

Figure 5.6: 3-D and 2-D snapshots of the liquid-liquid interface structure; (a) $\varepsilon_r = 1.5$, nondimensional initial mean film thickness $h_0/d =$ (i) 0.2, (ii) 0.5, (iii) 0.7 and (b) $\varepsilon_r = 0.3$, nondimensional initial mean film thickness $h_0/d =$ (i) 0.35, (ii) 0.5, (iii) 0.6 .

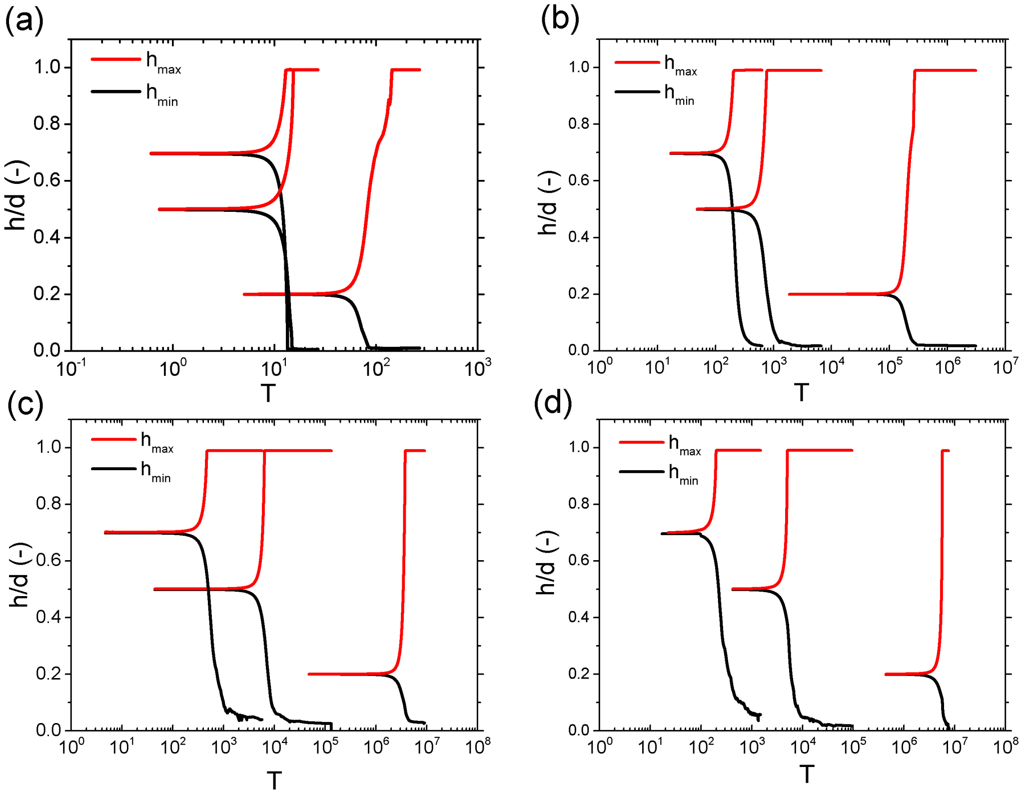

Figure 5.7: Nondimensional maximum and minimum film thickness, $h/d\ (-)$, variations versus nondimensional time, T, Relative electric permittivity ratios of layers, ε_r, and initial mean film thickness, h_0, effects on the drainage time. Permittivity ratios are: ε_r= (a) 0.1, (b) 0.6, (c) 1.5 and (d) 2.5. Initial electric field intensities (E_0) for 20, 50 and 70 nm thick films are: (a) 714, 363 and 273 MV/m, (b) 294, 250 and 227 MV/m, (c) 142, 160 and 174 MV/m and (d) 90, 114 and 137 MV/m, respectively.

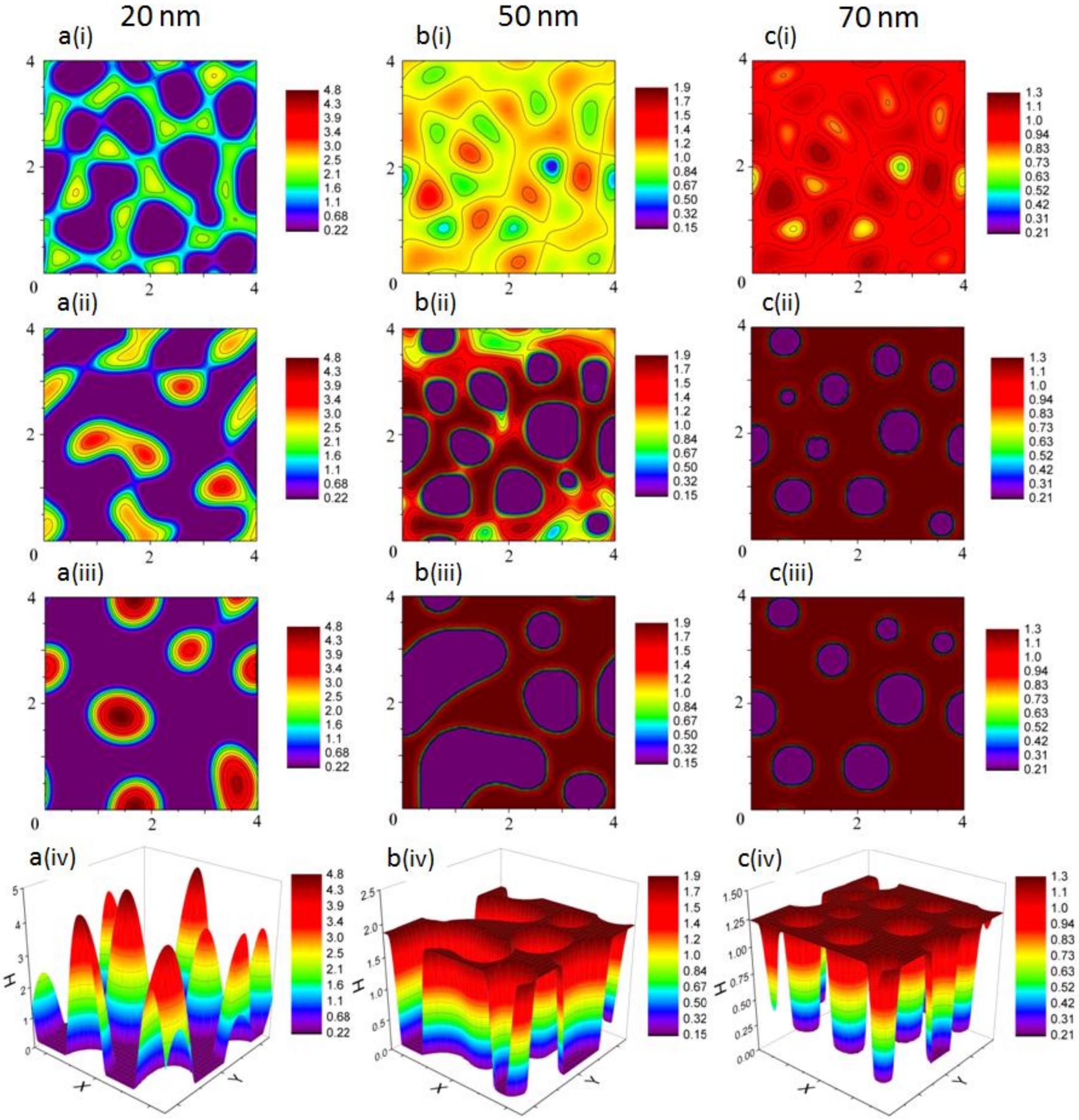

Figure 5.8: IL-PD bilayer, (a-c) images from i to iii show the 2-D spatiotemporal evolution for liquid-liquid interface instabilities in a $(4 \times 4)\lambda^2$ domain when $\varepsilon_r = 0.6$ and $M = 100$ $(mmol/L)$. Initial mean film thicknesses (h_0) are: a(i-iv) 20 nm, b(i-iv) 50 nm and c(i-iv) 70 nm. Nondimensional times for the plots are T= a(i) 9, a(ii) 11 and a(iii) 13.5; b(i) 7, b(ii) 8 and b(iii) 20; c(i) 7, c(ii) 10 and c(iii) 17. Plots a-c (iv) show 3-D snapshots of the liquid-liquid interface structure. Nondimensional times for the 3-D plots are T= a(iv) 13.5, b(iv) 20 and c(iv) 10. Initial electric field intensities (E_0) are: (a) 90, (b) 11 and (c) 137 MV/m.

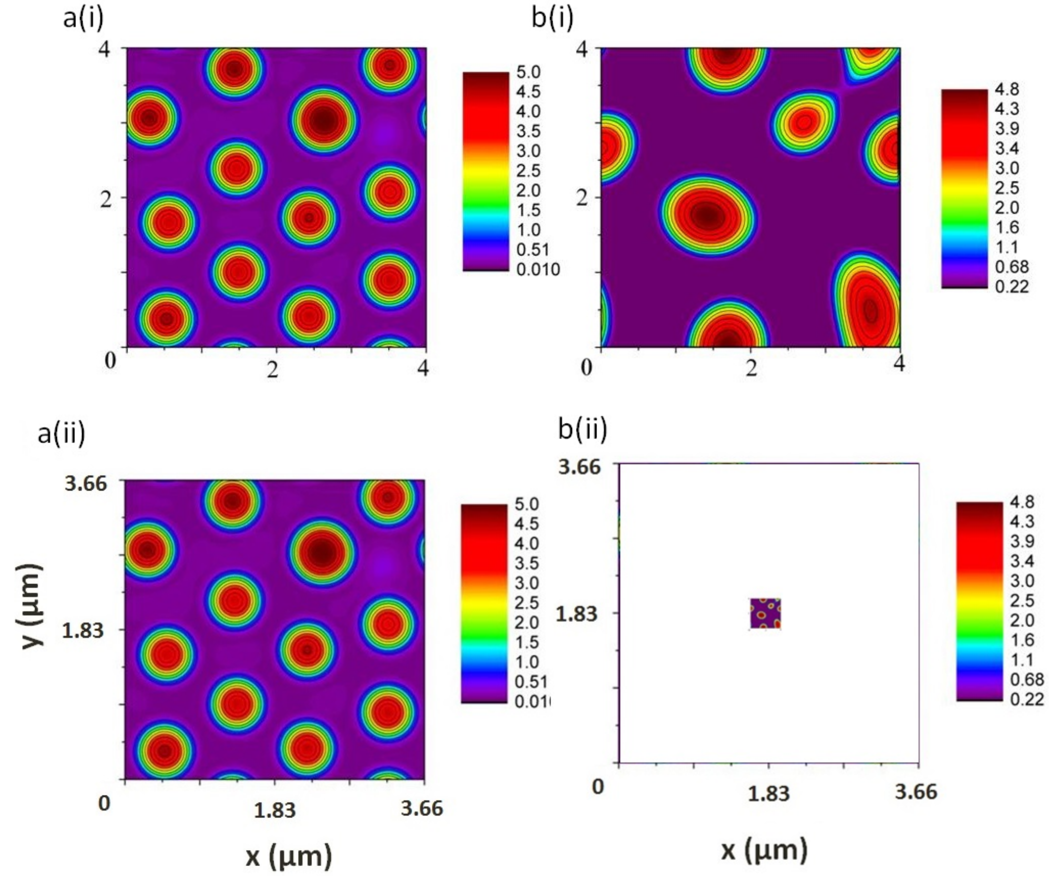

Figure 5.9: 2-D spatiotemporal evolution for liquid-liquid interface instabilities for the homogeneous electric field in (a) PD-PD and (b) IL-PD bilayer, (i) in a $(4 \times 4)\lambda^2$ domain and (ii) in a physical domain, when $\varepsilon_r = 0.6$ and $M = 100$ $(mmol/L)$ for IL-PD bilayer. Initial mean film thickness is: $h_0 = 20$ nm and nondimensional time for the plots are T= (a) 3.4×10^5 and (b) 13.5. $\psi_{up} = 20$ (V) and initial electric field intensities (E_0) are: (a) 294 and (b) 995.

Chapter 6

Combined thermo-electrohydrodynamic instabilities[†]

In the EHD patterning, the thin liquid film is typically assumed to be isothermal during its evolution process. Linear stability (LS) analysis (eqns. 3.34 and 3.35) shows that, lowering the interfacial tension leads to smaller structures since increased temperature reduces the interfacial tension (in commonly used materials in the EHD). Thus combining the thermocapillary (TC) effect with the EHD process is predicted to result in the formation of smaller sized features. The simultaneous effect of temperature gradient and the EHD in the patterning of films has been theoretically analyzed [127]. For 1-D films, the LS analysis predicted creation of smaller structures when EHD and thermal forces are combined.

To the best of our knowledge, the dynamics and mechanism of pattern formation in combined TC-EHD assisted patterning of nanofilms using a 3-D nonlinear formulation have not been analyzed. The main goal of this study is to investigate how to create smaller sized pillar arrays (compact features) by integrating the EHD patterning process with the TC model in a long-wave limit formulation. The effects of Marangoni number and thermal conductivity ratio of layers on the time evolution, the shape and the size of structures are investigated using analytical LS analysis and nonlinear numerical simulation.

A list of constants and simulation parameters are presented in Table 6.1.

[†] Parts of this chapter is based on Ref. [5], see Appendix C-1

Table 6.1: Constants and simulation parameters.

Parameter	Value
interfacial tension gradient (α)	48×10^{-5} N/mK
electric permittivity of the liquid film (ε_1)	2.5 [−]
electric permittivity of the bounding layer (ε_1)	1 [−]
applied voltage (ψ_{up})	0−20 [V]
thermal conductivity of film (k_1)	0.18 [W/mK]
temperature difference ($T_H - T_C$)	0 − 100 [K]
thermal conductivity ratio (k_1/k_2)	2 − 10 [−]
initial film thickness (h_0)	26 − 55 [nm]
electrodes distance (d)	100 [nm]
cut off distance (l_0)	1−3 nm

6.1 Electrostatic and thermocapillary pressures

A thin liquid film interface destabilizes and deforms when it is subjected to an electric field and/or a temperature gradient. In electrically assisted patterning, a variety of structures form depending on the initial filling ratio (ratio of initial film thickness to electrodes distance), electric permittivity ratio of the layers, the number of layers, etc [1, 23, 59, 82–84, 93, 96, 99–102, 145–147, 149–151].

From LS analysis, increasing the applied voltage results in smaller size patterns, however, experimental studies [1] show that electric breakdown occurs in either the film or the bounding layer when the applied electric field passes the electric breakdown limit of the material. Experimentally, the electric breakdown results in formation of larger size structures and unevenly distributed patterns in experiments which are not captured in the theoretical predictions ($\lambda_{exp} \gg \lambda_{LS}$). Therefore, creating ordered smaller structure (at a submicron level) is a limitation of the EHD patterning technique. Although different solutions have been suggested using multi-layer films with PD and/or LD [59, 96] and IC [1–3] properties, minimizing the size of structures in the EHD process is still an open research area.

In the EHD process, viscosity and interfacial tension tend to flatten the interface (i.e. damping forces). Using low viscous polymers is found to make the EHD patterning process faster. Lowering the process time from 24 hours to 2 hours in some cases [80]. Lowering the interfacial tension by using thermal gradient results in thermocapillry instability of the film. The dynamics and pattern formation in heated thick (with gravity effects) liquid films [90, 123–126] and nanofilms (with negligible gravity effects) [25, 60–62] have been extensively studied. Here the focus is on combining thermocapillary effects with EHD to pattern nanofilms. The goal is to find techniques to effectively reduce the structure size.

The variation of the electrostatic, ϕ_{EL} (N.m^{-2}), and thermal , ϕ_T (N.m^{-1}), pressures with film thickness is compared in figure 6.1 and provides insight into destabilizing factors. Negative values for ϕ indicate that the interface is pulled toward the upper electrode. In these cases, higher pressure acts on the interface when film is thicker implying that both electrostatic and thermal forces tend to amplify the perturbations. Thicker regions experience higher (upward) forces compared to the thinner regions and so instabilities grow. The impact of applied voltage on ϕ_{EL}, and the effects of modified Marangoni number and thermal conductivity ratio on ϕ_T are presented in figures 6.1(a) and 6.1(b), respectively.

In figure 6.1(a), increasing applied voltage (5→20 V) results in higher electrostatic pressure as expected. The increase in Marangoni number increases the thermal pressure over the range of film thickness as shown in figure 6.1(b). However, increasing the thermal conductivity ratio of layers, k$_r$, (from 2 to 5) results in lower absolute value of thermal force ϕ_T (for example, in h= 50 nm, the $\mid \phi_T \mid$ decreases from 0.096 to 0.03 N.m^{-1}).

The maximum wave number κ_{max} from LS analysis is found to be a function of the gradient of electrostatic and thermal pressure with respect to the film thickness (eqn. 3.35) and these gradients are called spinodal parameters [54]. In figure 6.1, the spinodal parameters ($\frac{\partial \phi}{\partial h}$) are also plotted (dotted lines and blue) versus the film thickness.

The negative values of electrostatic and thermal gradients demonstrate their destabilizing effect and the negative flow diffusion [54]. Higher values of $\frac{\partial \phi_{EL}}{\partial h}$ and $\frac{\partial \phi_T}{\partial h}$ result in higher values of κ_{max} which means smaller structure sizes will be formed. Increasing modified Marangoni number ($\bar{M}$) at a constant k$_r$ = 2 increases the absolute value of $\frac{\partial \phi_T}{\partial h}$ and ϕ_T. However, for the case of constant $\bar{M} = 4.5$, a decrease in k$_r$ does not necessarily lead to an increase in thermal force but depends on the film thickness. In other words, thicker regions of film (h> 75nm) in case of $\bar{M} = 4.5$ and k$_r$ = 5 experience much higher thermal forces ($\frac{\partial \phi_T}{\partial h}$) compared to the case of $\bar{M} = 4.5$ and k$_r$ = 2, whereas the behaviour is opposite for their thinner regions (h< 75nm).

6.2 Linear stability analysis

In figure 6.2, the LS analysis results for the growth rate of instabilities s, is plotted as a function of wave number, κ. The isothermal film (pure EHD) is compared to the heated film (combined EHD and thermocapillary effects) in figure 6.2(a). The peaks in growth rate variation indicate the maximum growth rates (s_{max}) and their corresponding maximum wave number (κ_{max}) in growth of instabilities. The LS analysis confirms that the addition of thermal gradient to the system results in application of higher force to the film interface and a smaller structure (higher κ_{max}). For the case of $\bar{M} = 4.5$ the increase in κ_{max} is more than 30%. The effect of thermal conductivity ratio of layers, k_r, on κ_{max} is also investigated using LS analysis and the results are shown in figure 6.2(b). Maximum wave number occurs for the lower ratio $k_r = 2$ which agrees with the thermal pressure results presented earlier. Similar trends of a decrease in characteristic wave length of instabilities with increase in Marangoni number and a decrease in the thermal conductivity ratio for the combined EHD and TC instabilities in the 1D film are observed [127].

6.3 Electrohydrodynamic (EHD) and Thermocapillary (TC) instabilities (base-cases)

The dynamics and 3-D snapshots of thin liquid film morphology in both isothermal and non-isothermal films have been investigated and because results are shown in figure 6.3. The interface pattern is presented in the quasi-steady stage in which the formed pillars do not merge for a long period of time. The interface maximum and minimum heights are tracked over time to demonstrate: (i) the thin liquid film drainage time, (ii) the time it takes the film interface to touch the upper electrode (growth rate of instabilities) and (iii) the rate of formation of pillars on the interface. The significant difference in non-dimensional times in figures 6.3a(i) and 6.3b(i) is due to the different scalings (see eqns. 3.36 and 3.39) used to nondimensionalize thin film equation for these two cases.

The negative diffusion (negative spinodal parameter) of fluid flow from thinner to thicker region of film results in raised columnar structures (pillars) on the interface (figure 6.3 a,b (ii)). When pillars touch the upper electrode their height is limited to the electrodes distance. The results show that growth rate of the interface is higher in the EHD case compared to the thermocapillary case. For both cases, over time more fluid flows to the core region and this entrainment enlarges the pillar and deepen the surrounding ring. Formed pillars in the EHD base-case have a more cylindrical shape whereas in the TC (Marangoni) case pillars have a more conical shape. In both cases, four pillars with circular cross section form in the $2\lambda \times 2\lambda$ computation spatial domain.

6.4 Combined EHD-Thermocapillary (EHD-TC) instabilities:

In order to investigate the addition of the thermocapillary effects on the morphological evolution of EHD nanofilms, the modified thin film equation in a long-wave limit (eqn. 3.37) is solved numerically. Modified Marangoni and thermal conductivity ratio are found as effective parameters from pressure distribution and LS analysis results (figures 6.1 and 6.2). The effects of Marangoni number and thermal conductivity ratio on the dynamics and film evolution process are investigated next. The applied voltage is chosen as low as ψ_{up} =5 V, to both avoid the electric breakdown in nanofilm and the bounding layer [1] and to also enable capturing the thermocapillary contribution in the patterning formation.

The main spatiotemporal evolution milestones of thin liquid film under combined effect of electrostatic and Marangoni forces are summarized in figure 6.4. The thin film undergoes the five major stages. Initial disturbances are reorganized and small amplitude bicontinuous structures are formed (stage i). Fragmentation occurs at long ridges and cone-shape pillars are formed (stages i and ii). The size of pillars is increased and isolated pillars with a hexagonal pattern are created (stages iii and iv). At quasi-steady state of patterning process, pillars have circular cross-section. Lastly, the coarsening begins which results in uneven distribution and larger pillars over the domain. The coarsening process and coalescence of neighbor pillars will be discussed in detail later.

When the modified Marangoni number is increased from $\bar{M} = 0.22$ (figure 6.4) to $\bar{M} = 2.26$ (figure 6.5), while holding all electrostatic parameters constant, it is found that the interface evolution time decreases considerably due to increased Marangoni effect. The lower evolution time and consequently faster fabrication process has also been experimentally reported when using low viscous polymer films in the EHD pattering process [80]. Although the mechanism of pattern formation remains the same (figure 6.5 b(i-iv)), pillars with a smaller size are formed leading to more compact structure fabrication when comparing figure 6.4 to figure 6.5. This decreasing trend in structure size qualitatively matches with those previously found for the 1D films [127].

To investigate the effect of the thermal conductivity ratio of the film and the bounding layer on the interface dynamics, $k_r = 2$ to 10 is varied and the spatiotemporal evolution of interface is presented in figure 6.6. As mentioned earlier, decreasing the relative thermal conductivity of layers (lower k_r) increases the thermal pressure at the interface. In addition, based on LS analysis, as k_r decreases the maximum wave number of the induced instabilities increases. This behavior is matched by the spatiotemporal evolution of interface as shown in figure 6.6. According to this figure, initial instabilities first grow and form a bicontinuous structure (stage i). Then fragmentation begins and spike shape pillars randomly grow on the interface and touch the upper electrode (stage ii). At this stage, pillars formed early get bigger and merge to neighbor pillars before complete pillar formation over the domain occurs (see figure 6.6 b(ii) and image M-ii). This early coarsening process avoids the formation of hexagonal pattern structure (see figure 6.6 b(ii, iii)). The final structure in figure 6.6 b(iv) consists of unstable non-uniform sized pillars which are randomly distributed over the domain. This behavior might be attributed to a significant increase in the thermal force for thicker regions of film when k_r is high which leads to higher and faster flow diffusion to the thicker regions (early formed pillars) whereas the flow diffusion is slower in other thinner regions (not completely formed pillars). The exponential increase in the thermal pressure and force is shown and compared for $k_r = 2$ and 5 in figure 6.1 (b).

When figure 6.6 is examined closely, two coarsening mechanisms are found: (a) collision of neighbor pillars with the same size which mainly occurs at the early stage of coarsening (compare region A in images M-iii and M-iv), and (b) Ostwald ripening which is merging of smaller pillars into larger size ones occurring predominantly in later stages of coarsening (compare region B in images M-iii and M-iv).

Improving the EHD patterning process in nanofilms by creating smaller sized pillars or more compact features by adding thermocapillary instability is the main goal of this chapter. So far it is shown that the modified Marangoni number and the thermal conductivity ratio affect both pattern formation time period and shape and size of the final structures. To quantify the compactness of the formed patterns, the number density of pillars formed in 1 μm^2 area of thin film is needed. Additionally the improvement in active surface area of the film is needed as this is of interest in data storage applications and surface analysis. The effect of modified Marangoni number on density of pillars and active surface area is now examined.

The thin film equation (eqn. 3.37) is numerically solved for different modified Marangoni numbers and 3-D snapshot of the pattern structure at the quasi-steady states are presented in figure 6.7 (i-iv). The base-case EHD patterning (figure 6.7 (i)) results show that in $(4\lambda \times 4\lambda)$ domain, 16 pillars formed which are hexagonally ordered over the domain. Adding thermocapillary effects ($\bar{M}$ increased from 0.22 to 4.5, in figure 6.7 (ii)-(iv)) results in an increase in total number of pillars forming on the interface. At $\bar{M} = 4.5$ a dense structure of cone shape pillars packed in smaller domain of $(2\lambda \times 2\lambda)$ in figure 6.7 (iv) is observed. The number density of pillars is defined as total number of completely formed pillars in 1 μm^2 area. Increasing the Marangoni number from 0 to 4.5 increases the number density of pillars significantly from 0.03 to 3.2 – a factor of 100. In addition, the center to center distance length decreases from $\sim$5 μm to $\sim$0.3 μm. The thermocapillary effect also decreased the cross section area of pillars, as can be observed in figure 6.7 (i-iv). The surface area of the interface is also calculated and its relative value with respect to the flat film interface at initial stage are plotted. Results show that the surface area is increased (relative to the initial flat film interface area) from 0.31% to 18.1% by adding the thermocapillary effects compared with traditional (isothermal film) EHD patterning.

6.5 Summary

Corbett and Kumar [127] showed, for the first time, the characteristic length scale in growth of instabilities decreases in the thermal-EHD patterning using both the LS and nonlinear analysis in 1D films. To extend that, the dynamics, morphological evolution and drainage time of liquid nanofilm (thickness$<$ 100 nm) subjected to a combined thermal-electrical field are studied considering a 2D lubrication-theory-based model. The thin film equation that includes thermal effects is re-derived in a long-wave limit and solved for both short time, linear stages, and long time, nonlinear stages. The LS analysis predicts a significant effect of the modified Marangoni number (relative strength of interfacial tension gradient force to the electrostatic force) and the thermal conductivity ratio of layers on the maximum wavelength on the growth of instabilities which, qualitatively matches the 1D film results [127].

The thin film equation is then numerically solved to numerically explore the nonlinear interface dynamics stages. Thermally and electrically induced base-case patterns are used to validate the numerical scheme. Then effects of Marangoni number and thermal conductivity ratio of layers on the shape and size of structures are investigated. Increasing the relative strength of thermocapillary force or, induced by the Marangoni effect, results in much smaller sized pillars while the mechanism of pattern formation remains unchanged. However, the thermal conductivity ratio is found to have an inverse effect on the pattern formation process. A coarsening mechanism is found to initiate at the early stages of pattern formation for high thermal conductivity ratios that prevents formation of uniform and hexagonal ordered pillars. This is attributed to a drastic increase in the thermocapillary force applied to thicker region of films at higher thermal conductivity ratios.

In general, the smaller structures are formed when the thermocapillary effects are combined with the EHD patterning mechanism. The number density of pillars formed in 1 μm^2 of domain area is increased from 0.03 to 3.2 (over one hundredfold) resulting in nano-sized pillar formation. The relative surface area of the patterned film (compared to initial flat stage) is increased up to 18% for combined TC-EHD, whereas this increase is about 1% in the EHD base-case which is of interest in the data storage applications in this nano-sized structures.

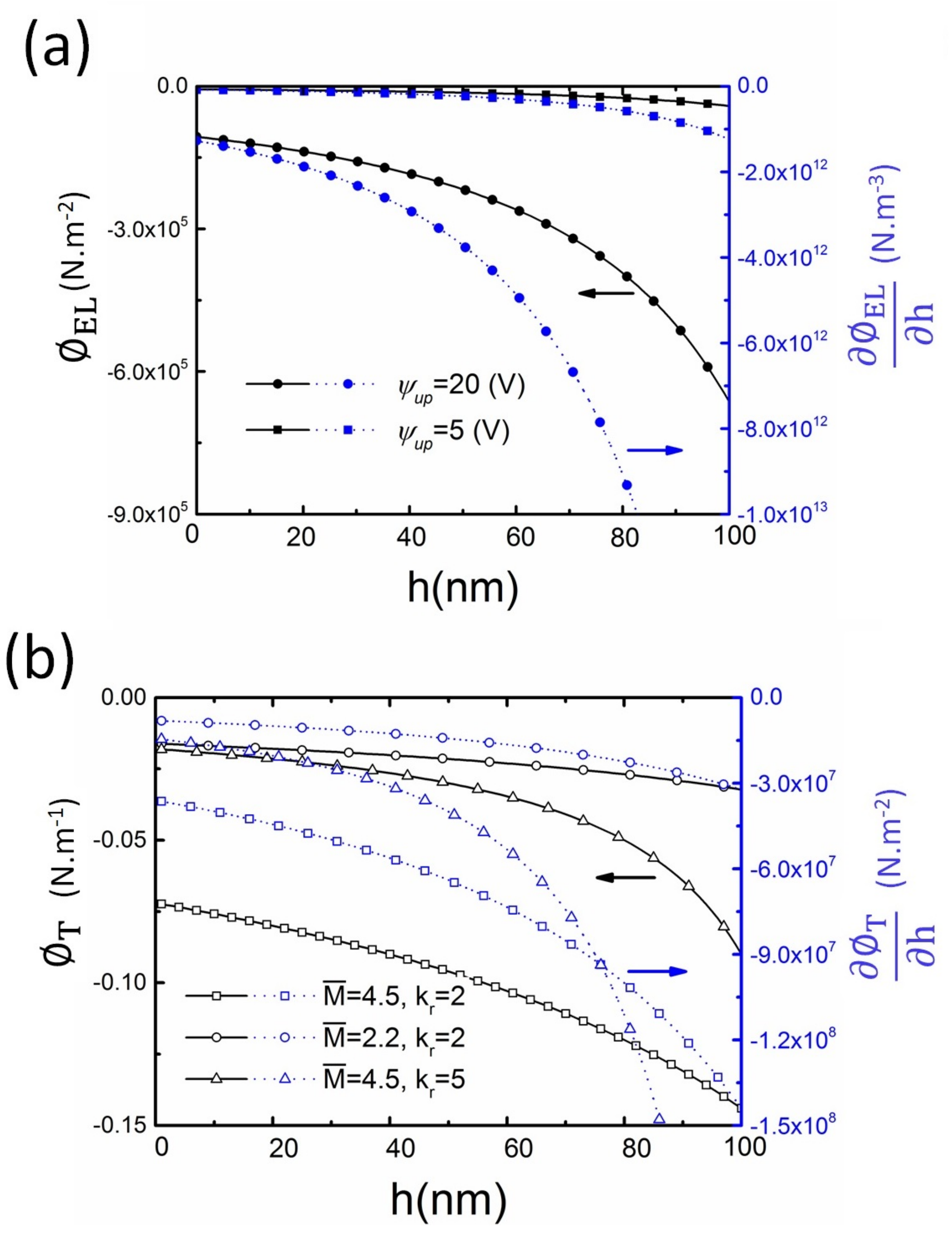

Figure 6.1: (a)Electrostatic and (b)thermal pressure, left axis, and spinodal parameter, right axis, distributions versus film thickness, effects of (a) applied voltage,ψ_{up} (b) modified Marangoni number, $\bar{M}$ and thermal conductivity ratio, k$_r$.

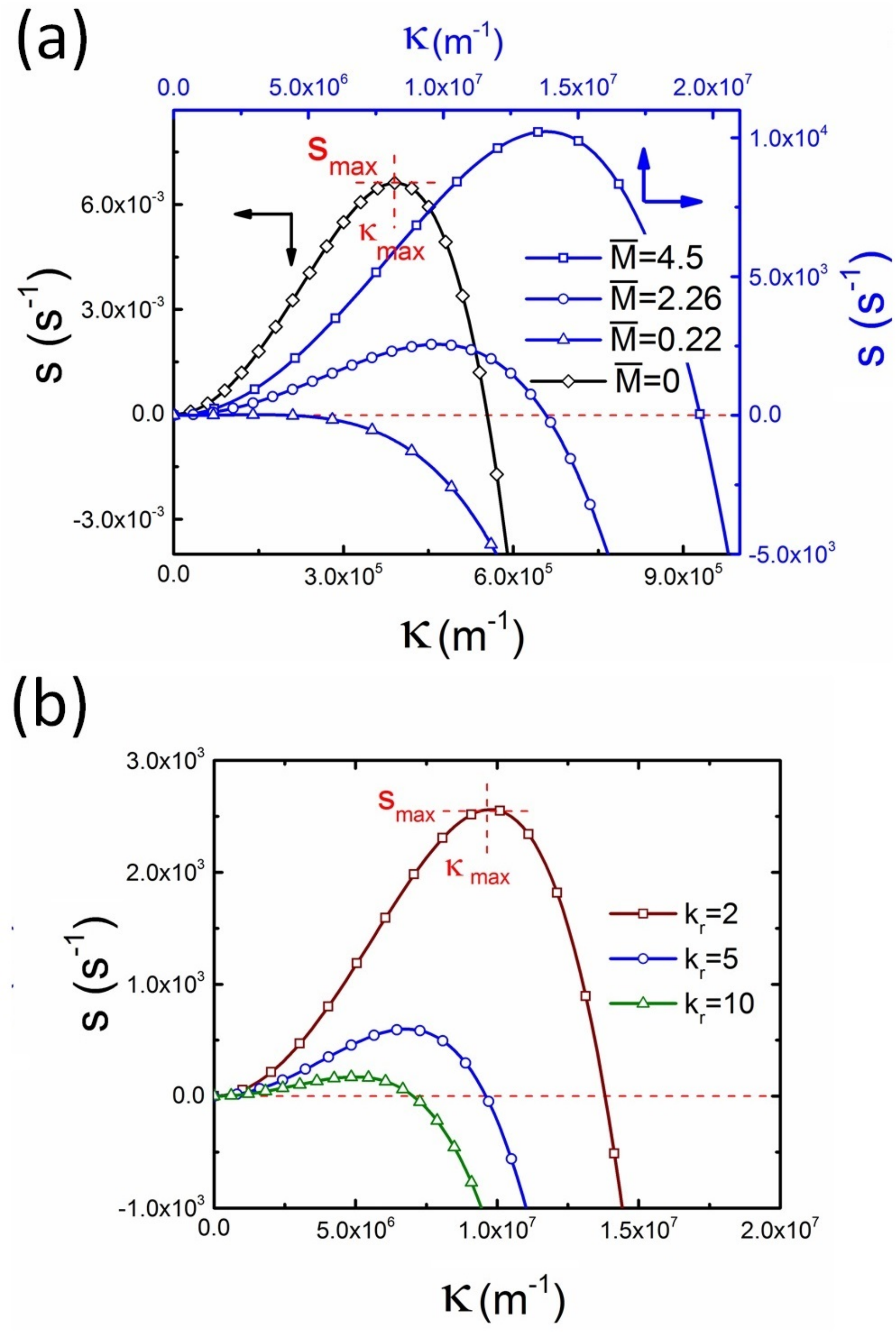

Figure 6.2: Growth rate distribution versus wave number (a) effect of modified Marangoni number, (b) thermal conductivity ratio. ψ_{up} =5 V, (a) k$_r$ = 2, (b) $\bar{M}$ = 4.5.

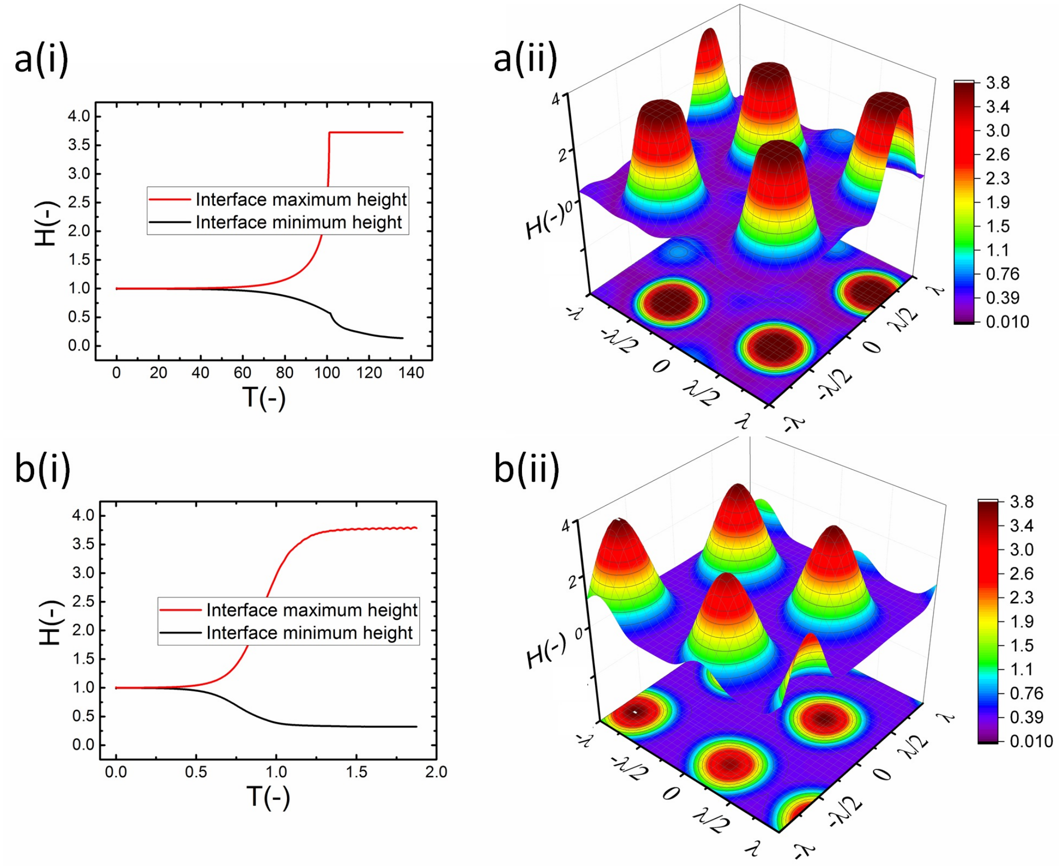

Figure 6.3: Base-case EHD and thermocapillary instabilities, Interface height change versus time and 3-D snapshot of the film interface for a(ii) EHD and b(ii) thermocapillary base-cases at their quasi-steady stage. In EHD base-case: ψ_{up} =5 V and $\lambda = 5.34\ \mu$m. In thermocapillary base-case (using scalings 3.39-3.36): ψ_{up} =0 V, $\bar{M} = 4.05$, $A_L = -1.51 \times 10^{-17}$J and $\lambda = 0.6\ \mu$m.

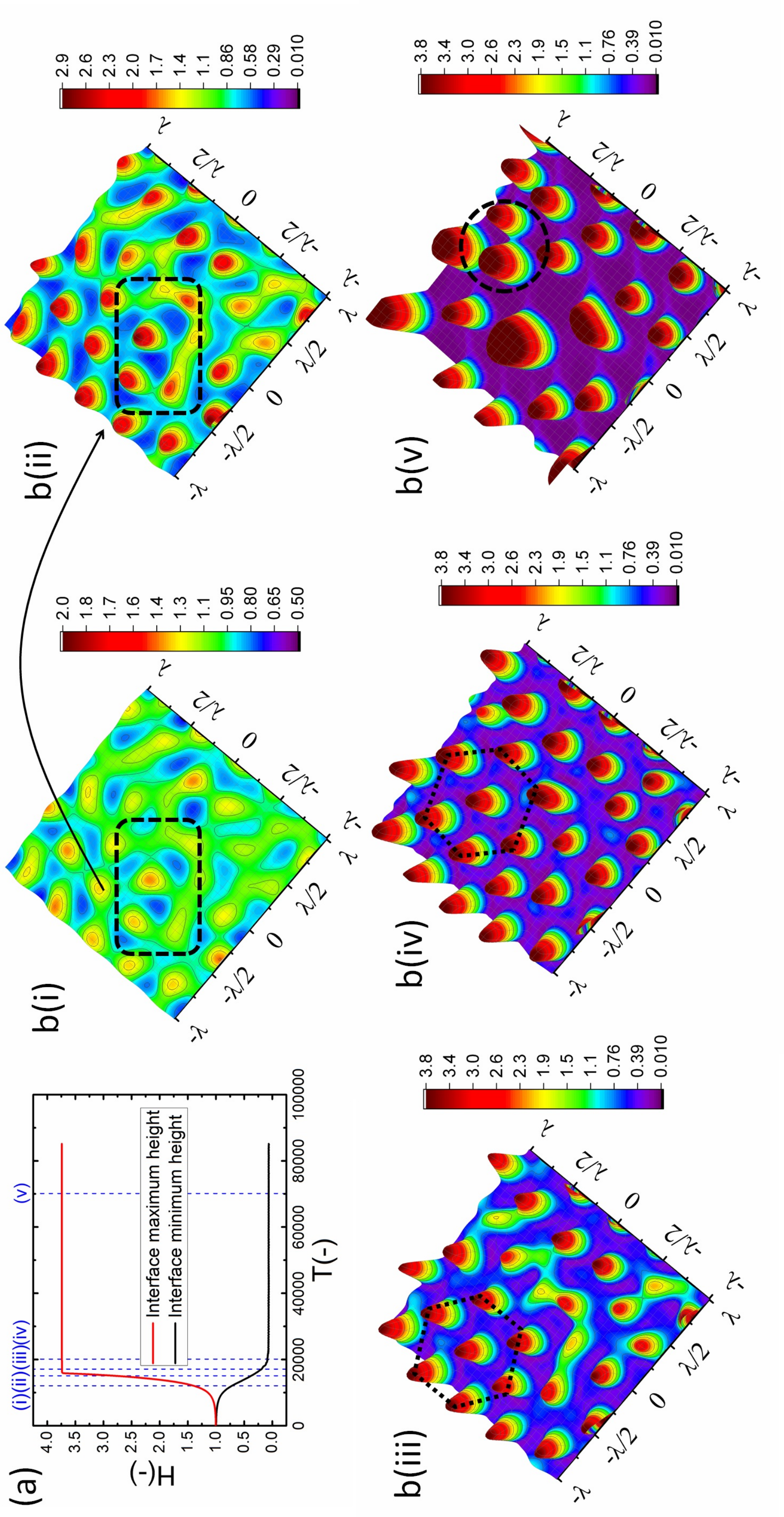

Figure 6.4: Interface height change versus time (a) and spatiotemporal evolution of interface b(i-iv) in combined EHD-Marangoni instabilities. Applied voltage, ψ_{up} =5 V, initial film thickness, $h_0 = 26$ nm, relative thermal conductivity, k$_r$ = 2 and modified Marangoni number, $\bar{M} = 0.22$. Nondimensional times, T = (i)1.2×10^4, (ii)1.5×10^4, (iii)1.7×10^4 (iv)2.0×10^4 and (v)7.0×10^4. $\lambda = 5.34$ μm.

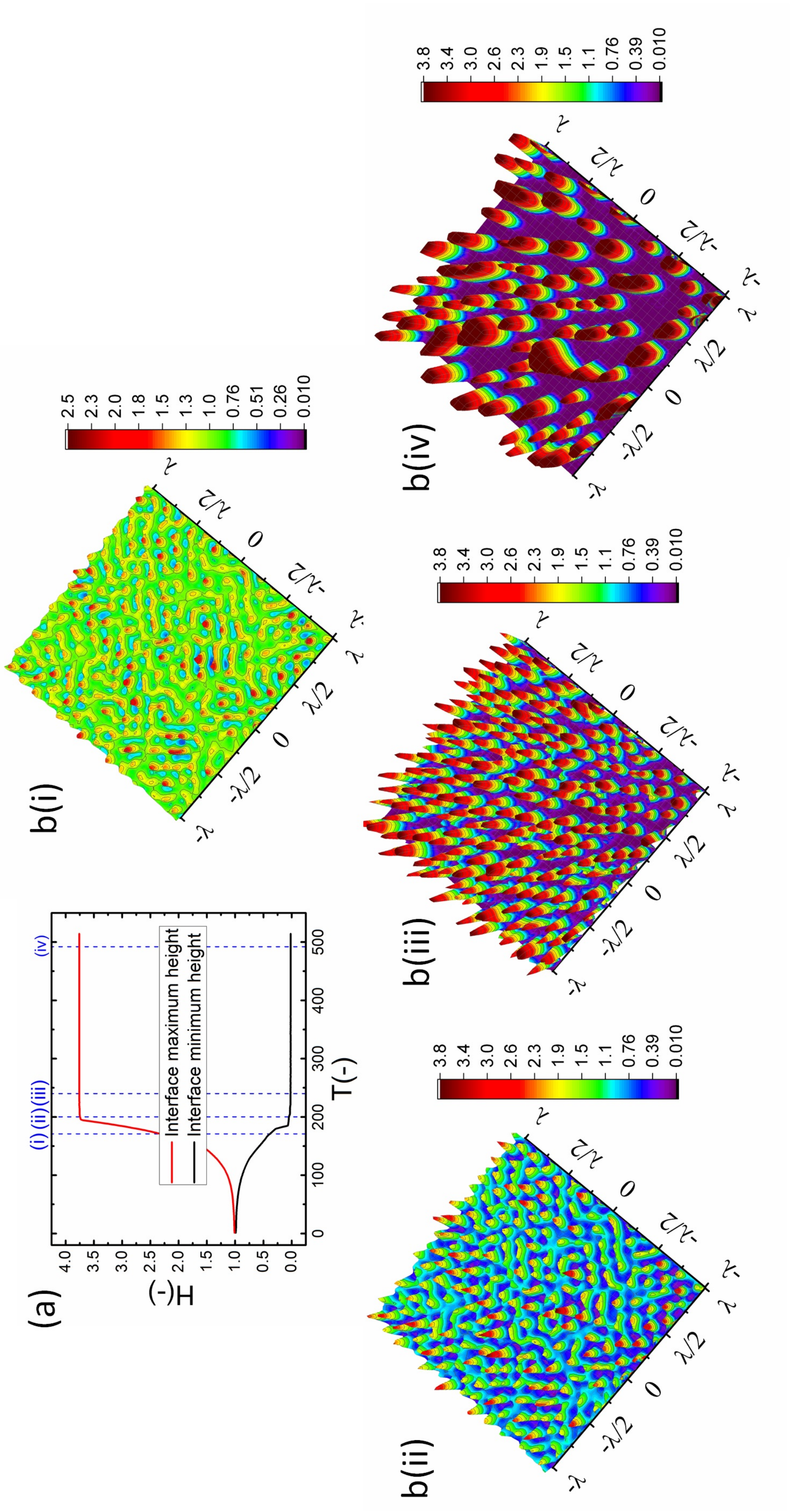

Figure 6.5: Interface height change versus time (a) and spatiotemporal evolution of interface b(i-iv) in combined EHD-Marangoni instabilities. Applied voltage, ψ_{up} =5 V, initial film thickness, $h_0 = 26$ nm, relative thermal conductivity, k$_r$ = 2 and modified Marangoni number, $\bar{M} = 2.26$. Nondimensional times, T = (i)171, (ii)200 (iii)240 and (iv)494×10^4. Domain size, $(2\lambda \times 2\lambda) = 10.7\ \mu\text{m}^2$.

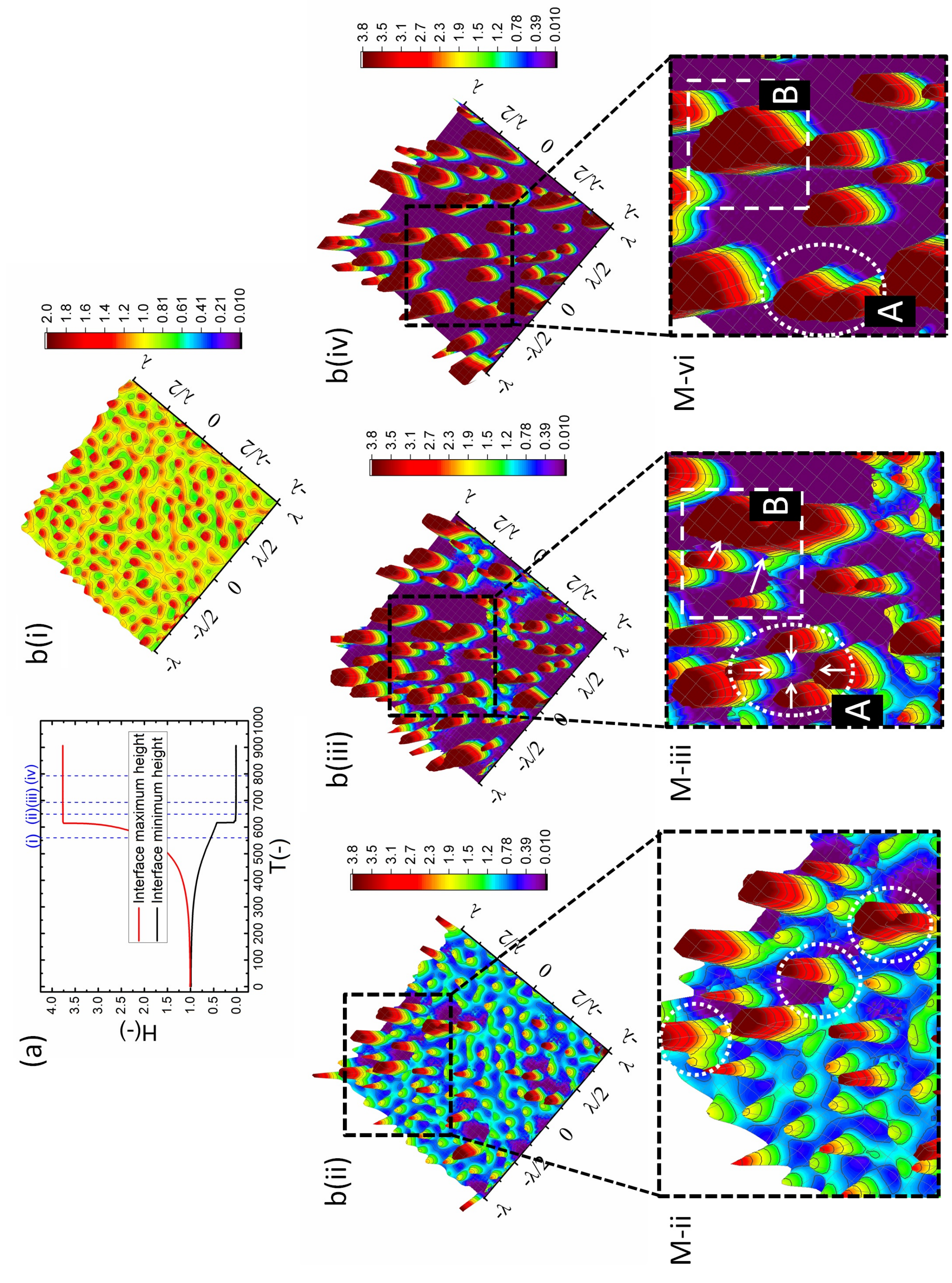

Figure 6.6: Interface height change versus time (a) and spatiotemporal evolution of interface b(i-iv) in combined EHD-Marangoni instabilities. Applied voltage, ψ_{up} =5 V, initial film thickness, $h_0 = 26$ nm, relative thermal conductivity, k$_r$ = 10, and modified Marangoni number, $\bar{M} = 4.5$. Nondimensional times, T = (i)560, (ii)649 (iii)693 and (iv)793. Domain size, $(2\lambda \times 2\lambda) = 10.7\ \mu\text{m}^2$.

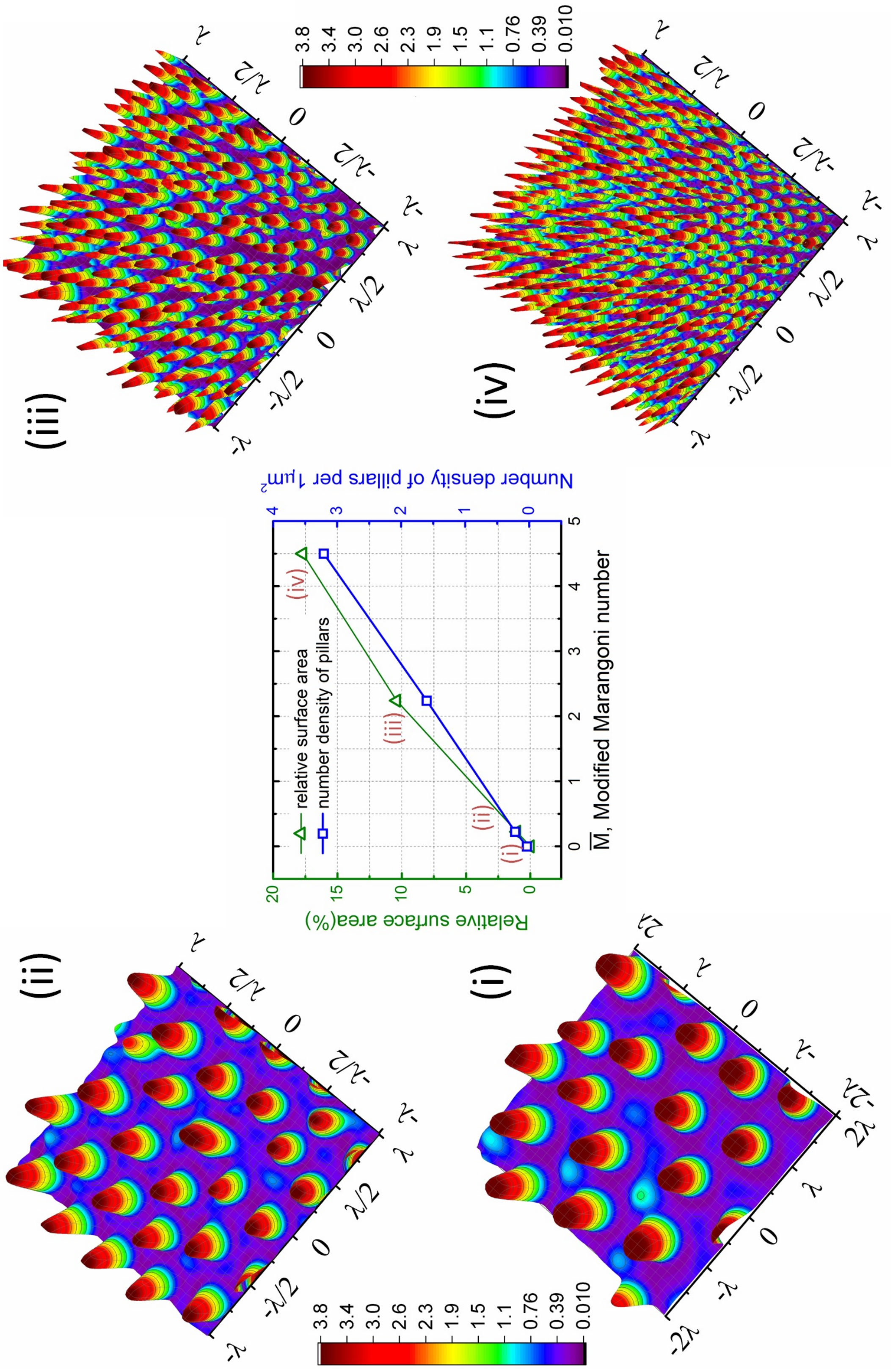

Figure 6.7: 3-D snapshots of the interface at quasi-steady state (i-iv). Variation of relative surface area and number density of pillars with modified Marangoni number. (i) EHD base-case, applied voltage, ψ_{up} =5 V. Modified Marangoni number, $\bar{M}$ = (ii)0.22, (iii)2.26 , (iv)4.5. Initial film thickness, $h_0 = 26$ nm, relative thermal conductivity, $\mathrm{k}_r = 2$ and $\lambda = 5.34\ \mu$m.

Chapter 7

Conclusions and future work

7.1 Conclusions

To enhance the electrohydrodynamic (EHD) patterning to achieve the smaller sized features which are uniformly distributed over the domain area is the main aim of this thesis. Investigating the literature, a lack of use of electrostatic models is found for the EHD patterning of nanofilms. When a transverse electric field is applied to the film with thickness of less than 100 nm, charges or free ions move and accumulate close to the charged surfaces. This results in the formation of diffuse layers, called double layers, which are absent in perfect dielectric (PD) and leaky dielectric (LD) models. In LD model the DL thickness is much smaller than the film thickness so this layer is not considered in derivation of electrostatic model. However, in nanofilms, the DL layer thickness is comparable to the film thickness. Therefore, dynamics and charges/ions distribution affects the electric field in the film and consequently the electrostatic force acting on the interface. In order to model the charges/ions distribution in the DL, the thin film is assumed to behave like electrolytes and is called ionic liquid (IL) film.

Initially, an electrostatic model is developed for confined IL films in contact with PD bounding media via a coupling of linearized Poission-Boltzmann and Laplace equations to obtain the electric potential distribution and consequently the net electrostatic pressure acting on the interface. The key insight our electrostatic model provides is that, the leaky dielectric model may not account for phenomena important for EHD patterning, namely the presence of finite ions in the conducting layers. Debye length is defined using ionic strengths, which provides a realistic range of free charge concentrations in the conducting fluid layer compared to previous work in the literature [116].

The developed IL model is not limited to the assumption of having very large or small electric diffuse layer as in the PD and LD models, respectively. This model is coupled to the nonlinear thin film equation and solved numerically to investigate the dynamics, instability and process of pattern formation in the EHD patterning process. Based on this model, ionic liquids are defined to be materials having properties between two limiting cases of PC and PD materials based on their ionic strength. IL films experience a much higher electrostatic pressure compared to similar PD films (with the same electric permittivity) and an increase in ionic strength results in higher electrostatic pressure. PD films are modeled first to investigate the accuracy of numerical scheme and to provide a well known baseline case to compare the results with IL thin films. Then IL films of various molarity are numerically simulated and the structure and number of pillars is compared to PD films.

Early stages of pillar formation process in IL films is found to be similar to PD films and electric induced instabilities grow is caused by negative diffusion. Pillars are initially formed on the random locations and enlarge in cross section over time as the contact line expands on the top electrode. The pillars formation process occurs faster in IL films and is further accelerated with increasing the ionic strength. Generally, smaller structures are found in IL film when compared to similar PD films and the trend is to even smaller structures with increased initial film height. For the case of increasing h_0 from 20 to $50nm$, the IL film with $M = 0.0001\ mol/L$ has 5 times more structures per $1\mu m^2$ compared to a PD film. This was described in detail in chapter 4.

It is also shown that addition of ionic conductivity to the polymer film leads to more compact but less ordered pillars. Similar to the PD films [91, 96] coarsening of the structure happens randomly over the domain resulting in non-uniform patterns. To overcome this limitation, a patterned mask is used to electrostatically control the structures size and fluid patterns.

The effects of protrusion and groove size (width and depth) in strip like and square block patterns and the film initial filling ratio on the size, shape and order of fluid patterns are investigated. When flat electrode is replaced with the patterned electrode, two characteristic spatial lengths are identified which are controlled by the width of strip/square block (W_2), the groove width (W_1) and the groove depth ($d_1 - d_2$). Results show that depending on the groove width and depth the EHD patterning process has either two or three main stages. In the two-stage process, patterns only form under the protrusions whereas in the three-stage process, pattern (either undulating or secondary pillars) also form under the grooves. The two-stage process can be used for the pattern replication of mask onto the film and the three-stage one is utilized when the multilevel structure formation is desired. Furthermore, more pillars are found to be created using an IL film rather than a PD film. By using electrodes with square protrusions $(\sqrt{n}+1)^2$ pillars are formed in IL film for every n pillars generated in PD film. In the PD film, electrode square block mask protrusions with width of $W_2 = 1.5 \times \lambda_m$ and groove width of $W_1 = 0.5 \times \lambda_m$ and in the IL film square block protrusions with width of $W_2 = \lambda_m$ and groove width of $W_1 = 0.25 \times \lambda_m$ result in compact and well ordered fluid pillars.

In the literature is shown that using bounding layer instead of air results in smaller sized features and PD and LD models have been used. More recently, it is experimentally shown that the use of ionic conductive bounding layer results in nano sized pillar formation [1]. To improve the introduced electrostatic model based on the nonlinear Poission-Boltzmann equation considered and it is analytically solved when it is coupled with the Laplace equation for the PD layer to find the electrostatic force acting on the interface over the course of evolution.

As base case, PD-PD bilayers considered first. In PD-PD bilayers with $\varepsilon_r < 1$, pillars, bicontinuous, holes and roll-like structures are formed, whereas the last two features are not observed in the bilayers with $\varepsilon_r > 1$. When the thin film is thicker than bounding media, the final pattern is more sensitive to electric permittivity ratio. Thicker films are found to drain faster in bilayers with $\varepsilon_r < 1$ similar to bilayers with $\varepsilon_r > 1$.

For IL-PD bilayers, to predict the electrostatic component of conjoining/disjoining pressure acting on the interface, an analytical model is developed based on the nonlinear Poission-Boltzmann equation. Perfect dielectrics and perfect conductors are found as limiting cases for ionic liquids with low and high ionic strength, respectively. The IL-PD interfaces is subject to a much higher electrostatic pressure compared with the PD-PD interface (in the order of 10^3 to 10^7 times higher for the $\psi_{up} = 10\ V$ case). It is found that the IL-PD bilayers with $\varepsilon_r > 1$ remain stable under the action of transverse electric field whereas the similar PD-PD bilayers are unstable.

The use of an IL layer is found to reduce the size of the structures by a factor of ten (λ_{PD-PD} is about ten times larger than λ_{IL-PD}) for the case studied.

This has important implication when the goal is to produce small structures. The IL-PD pillars tend to be polydispersed and more disordered over the domain compared to the PD-PD ones. The developed analytical models and resulting numerical simulation closely predicts the interface behavior for both PD-PD and IL-PD bilayers over the parameters range tested when compared to other numerical studies and experimental observations in the literature. This indicates the developed numerical simulation is of utility in predicting PD-PD and IL-PD bilayer response to an applied electric field.

Another common assumption in the EHD patterning is considering the isothermal condition for the film. Corbett and Kumar [127] showed, for the first time, the characteristic length scale in growth of instabilities decreases in the thermal-EHD patterning using both the LS and nonlinear analysis in 1D films. To extend that, the dynamics, morphological evolution and drainage time of liquid nanofilm (thickness$<$ 100 nm) subjected to a combined thermal-electrical field are studied considering a 2D lubrication-theory-based model. The thin film equation that includes thermal effects is re-derived in a long-wave limit and solved for both short time, linear stages, and long time, nonlinear stages. The LS analysis predicts a significant effect of the modified Marangoni number (relative strength of interfacial tension gradient force to the electrostatic force) and the thermal conductivity ratio of layers on the maximum wavelength on the growth of instabilities which, qualitatively matches the 1D film results [127].

Effects of Marangoni number and thermal conductivity ratio of layers on the shape and size of structures are investigated. Increasing the relative strength of thermocapillary force or, induced by the Marangoni effect, results in much smaller sized pillars while the mechanism of pattern formation remains unchanged. However, the thermal conductivity ratio is found to have an inverse effect on the pattern formation process. A coarsening mechanism is found to initiate at the early stages of pattern formation for high thermal conductivity ratios that prevents formation of uniform and hexagonal ordered pillars. This is attributed to a drastic increase in the thermocapillary force applied to thicker region of films at higher thermal conductivity ratios.

In general, the smaller structures are formed when the thermocapillary effects are combined with the EHD patterning mechanism. The number density of pillars formed in 1 μm^2 of domain area is increased from 0.03 to 3.2 (over one hundredfold) resulting in nano-sized pillar formation. The relative surface area of the patterned film (compared to initial flat stage) is increased up to 18% for combined TC-EHD, whereas this increase is about 1% in the EHD base-case which is of interest in the data storage applications in this nano-sized structures.

7.2 Future work

Further studies that can be done as a continuation of the current study are listed below:

- In derivation of the electrostatic model for the finite electric diffuse layer (DL) the dynamic of charges was negligible since the charge relaxation time was smaller than the process time. The model can be improved for the cases which the dynamic of charges are considerable and complete Nernst-Planck equation needed to be solve simultaneously. Charge relaxation time is small for high conductive materials like water based solutions and electrolytes, whereas for lower conductive materials like Polystyrene (PS) and para-Methoxymethamphetamine (PMMA) it is large and might be comparable to the process time.

- The combined thermo-electrohysrodynamic destabilization and patterning of bilayer systems can be investigated. The relative thickness and viscosity of film and bounding layers will have significant effects on both thermocapillary instability (long-wave or short range Marangoni instability) and electrohydrodynamic instability of the system and should be further investigated.

- In the case of combined thermo-electrohyrodynamic patterning, effect of non-uniform heating on the destabilization and pattern formation can now be investigated to see the sensitivity of the patterns to the heating non-uniformity..

- The effect of thermal evaporation can also be added to the TC-EHD system. This could be done by adding thermal evaporation term to the thin film equation and is of interest for heated polymer films when the solvent evaporation happens during the evolution process or EHD process of volatile materials.

7.3 List of contributions

The following is a list of contributions from this thesis in the form of conference and journal publications.

7.3.1 Journal papers

Ref. [2] -Hadi Nazaripoor, Charles R. Koch, and Subir Bhattacharjee. Electrical perturbations of ultrathin bilayers: Role of ionic conductive layer. Langmuir, 30(49):1473414744, 2014. PMID: 25419880.

Ref. [3] -Hadi Nazaripoor, Charles R. Koch, Mohtada Sadrzadeh, and Subir Bhattacharjee. Electrohydrodynamic patterning of ultra-thin ionic liquid films. Soft Matter, 11:21932202, 2015.

Ref. [4] -Hadi Nazaripoor, Charles R. Koch, Mohtada Sadrzadeh, and Subir Bhattacharjee. Compact micro/nano electrohydrodynamic patterning: Using a thin conductive film and a patterned template. Soft Matter, 12:10741084, 2016.

Ref. [5] -Hadi Nazaripoor, Charles R. Koch, Mohtada Sadrzadeh, and Subir Bhattacharjee. Thermo-electrohydrodynamic patterning in nanofilms. Langmuir, 32(23):57765786, 2016.

7.3.2 Conference papers and presentations

Ref. [6] -Hadi Nazaripoor, Charles R. Koch, and Subir Bhattacharjee. Dynamics of thin liquid bilayers subjected to an external electric field. In Proceedings of ASME. 46545, volume 7, pages 6269, November 2014. DOI:10.1115/IMECE2014-37302.

Ref. [152] -Hadi Nazaripoor, Charles R Koch, Mohtada Sadrzadeh. Electrostatic model for electric-field-induced instabilities of thin ionic liquid films. Presented in 64th Canadian Society of Chemical Engineering Conference, 19-22 October 2014, Niagara Falls, ON, Canada.

Ref. [153] -Hadi Nazaripoor, Behnam Khorshidi, Charles R. Koch, Mohtada Sadrzadeh, Interface morphology of thin films: electrohydrodynamic vs electrokinetic model, Accepted in 24th International Congress of Theoretical and Applied Mechanics ICTAM 2016, August 21-26, 2016

References

[1] Cindy Y. Lau and William B. Russel. Fundamental limitations on ordered electrohydrodynamic patterning. *Macromolecules*, 44(19):7746–7751, 2011.

[2] Hadi Nazaripoor, Charles R. Koch, and Subir Bhattacharjee. Electrical perturbations of ultrathin bilayers: Role of ionic conductive layer. *Langmuir*, 30(49):14734–14744, 2014. PMID: 25419880.

[3] Hadi Nazaripoor, Charles R. Koch, Mohtada Sadrzadeh, and Subir Bhattacharjee. Electrohydrodynamic patterning of ultra-thin ionic liquid films. *Soft Matter*, 11:2193–2202, 2015.

[4] Hadi Nazaripoor, Charles R. Koch, Mohtada Sadrzadeh, and Subir Bhattacharjee. Compact micro/nano electrohydrodynamic patterning: Using a thin conductive film and a patterned template. *Soft Matter*, 12:1074–1084, 2016.

[5] Hadi Nazaripoor, Charles R. Koch, Mohtada Sadrzadeh, and Subir Bhattacharjee. Thermo-electrohydrodynamic patterning in nanofilms. *Langmuir*, 32(23):5776–5786, 2016.

[6] Hadi Nazaripoor, Charles R. Koch, and Subir Bhattacharjee. Dynamics of thin liquid bilayers subjected to an external electric field. In *Proceedings of ASME. 46545*, volume 7, pages 62–69, November 2014. DOI:10.1115/IMECE2014-37302.

[7] D Quere. Fluid coating on a fiber. *Annual Review of Fluid Mechanics*, 31:347–384, 1999.

[8] John S. Eow, Mojtaba Ghadiri, Adel O. Sharif, and Trevor J. Williams. Electrostatic enhancement of coalescence of water droplets in oil: A

review of the current understanding. *Chemical Engineering Journal*, 84(3):173 – 192, 2001.

[9] Farshid Mostowfi, Khristo Khristov, Jan Czarnecki, Jacob Masliyah, and Subir Bhattacharjee. Electric field mediated breakdown of thin liquid films separating microscopic emulsion droplets. *Applied Physics Letters*, 90(18):184102, 2007.

[10] S.P Lin and Howard Brenner. Marangoni convection in a tear film. *Journal of Colloid and Interface Science*, 85(1):59 – 65, 1982.

[11] O. A. Kabov, E. Y. Gatapova, and D. V. Zaitsev. Cooling technique based on evaporation of thin and ultra thin liquid films. In *Thermal and Thermomechanical Phenomena in Electronic Systems, 2008. ITHERM 2008. 11th Intersociety Conference on*, pages 520–527, May 2008.

[12] A. Vrij. Possible mechanism for the spontaneous rupture of thin free liquid films. *Discussions of the Faraday Society*, 42:23–33, 1966.

[13] A. Sheludko. Thin liquid films. *Advances in Colloid and Interface Science*, 1:391–464, 1967.

[14] Eli Ruckenstein and Rakesh K. Jain. Spontaneous rupture of thin liquid films. *Journal of Chemical Society Faraday Transactions*, 70:132–147, 1974.

[15] Malcolm B Williams and Stephen H Davis. Nonlinear theory of film rupture. *Journal of Colloid and Interface Science*, 90(1):220 – 228, 1982.

[16] Ashutosh Sharma. Relation of thin film stability and morphology to macroscopic parameters of wetting in the apolar and polar systems. *Langmuir*, 9(2):861–869, 1993.

[17] Alexander Oron, Stephen H. Davis, and S. George Bankoff. Long-scale evolution of thin liquid films. *Review of Modern Physics*, 69:931–980, Jul 1997.

[18] R. Khanna A. Ghatak and A. Sharma. Dynamics and morphology of holes in dewetting of thin films. *Journal of Colloid and Interface Science*, 212(10):483–494, 1999.

[19] Ashutosh Sharma and Rajesh Khanna. Pattern formation in unstable thin liquid films under the influence of antagonistic short- and long-range forces. *Journal of Chemical Physics*, 110(10):4929–4936, 1999.

[20] Derek Y. C. Chan, Evert Klaseboer, and Rogerio Manica. Film drainage and coalescence between deformable drops and bubbles. *Soft Matter*, 7:2235–2264, 2011.

[21] Ashutosh Sharma and Eli Ruckenstein. An analytical nonlinear theory of thin film rupture and its application to wetting films. *Journal of Colloid and Interface Science*, 113(2):456–479, 1986.

[22] Vladimir S. Mitlin. Dewetting of solid surface: Analogy with spinodal decomposition. *Journal of Colloid and Interface Science*, 156(2):491 – 497, 1993.

[23] Erik Schaffer, Thomas Thurn-Albrecht, Thomas P. Russell, and Ullrich Steiner. Electrically induced structure formation and pattern transfer. *Nature*, 403:874–877, 2000.

[24] Bestehorn, M., Pototsky, A., and Thiele, U. 3d large scale marangoni convection in liquid films. *European Physical Journal B: Condensed Matter Physics*, 33(4):457–467, 2003.

[25] Erik Schaffer, Stephan Harkema, Monique Roerdink, Ralf Blossey, and Ullrich Steiner. Morphological instability of a confined polymer film in a thermal gradients. *Macromolecules*, 36(5):1645–1655, 2003.

[26] Qiming Wang, Lin Zhang, and Xuanhe Zhao. Creasing to cratering instability in polymers under ultrahigh electric fields. *Physical Review Letters*, 106:118301, Mar 2011.

[27] Andrew Corbett and Satish Kumar. Combined thermal and electrohydrodynamic patterning of thin liquid films. *Journal of Engineering Mathematics*, pages 1–16, 2013.

[28] Justin Trice, Christopher Favazza, Dennis Thomas, Hernando Garcia, Ramki Kalyanaraman, and Radhakrishna Sureshkumar. Novel self-organization mechanism in ultrathin liquid films: Theory and experiment. *Physical Review Letters*, 101:017802, Jul 2008.

[29] Hare Krishna, Nozomi Shirato, Sagar Yadavali, Ritesh Sachan, Jeremy Strader, and Ramki Kalyanaraman. Self-organization of nanoscale multilayer liquid metal films: Experiment and theory. *ACS Nano*, 5(1):470–476, 2011.

[30] Christian W. J. Berendsen, Jos C. H. Zeegers, and Anton A. Darhuber. Thinning and rupture of liquid films by moving slot jets. *Langmuir*, 29(51):15851–15858, 2013.

[31] Rajesh Khanna and Ashutosh Sharma. Pattern formation in spontaneous dewetting of thin apolar films. *Journal of Colloid and Interface Science*, 195(10):42–50, 1997.

[32] Jacob N. Israelachvili. *Intermolecular and Surface Forces*. Burlington, MA : Academic Press, 2011.

[33] Jacob H. Masliyah and Subir Bhattacharjee. *Electrokinetic and Colloid Transport Phenomena*. Wiley-Interscience: Hoboken, NJ, 2006.

[34] Uwe Thiele, Michael Mertig, and Wolfgang Pompe. Dewetting of an evaporating thin liquid film: Heterogeneous nucleation and surface instability. *Physical Review Letters*, 80:2869–2872, Mar 1998.

[35] Jayant Singh and Ashutosh Sharma. Self-organzation in unstable thin liquid films: dynamics and patterns in systems displaying a secondary minimum. *Journal of Adhesion Science and Technology*, 14(10):145–166, 2000.

[36] Daniel Bonn, Jens Eggers, Joseph Indekeu, Jacques Meunier, and Etienne Rolley. Wetting and spreading. *Review of Modern Physics*, 81:739–805, May 2009.

[37] Roland Keunings and DW Bousfield. Analysis of surface tension driven leveling in viscoelastic films. *Journal of non-newtonian fluid mechanics*, 22(2):219–233, 1987.

[38] Haroon S. Kheshgi and L.E. Scriven. The evolution of disturbances in horizontal films. *Chemical Engineering Science*, 43(4):793 – 801, 1988.

[39] DW Bousfield. A model to predict the leveling of coating defects. *Tappi journal*, 74(5):163–170, 1991.

[40] Rajan R. Iyer and Douglas W. Bousfield. The leveling of coating defects with shear thinning rheology. *Chemical Engineering Science*, 51(20):4611 – 4617, 1996.

[41] M. Wulf, P. Uhlmann, S. Michel, and K. Grundke. Surface tension studies of levelling additives in powder coatings. *Progress in Organic Coatings*, 38(2):59 – 66, 2000.

[42] Benson Tsai, Marcio S. Carvalho, and Satish Kumar. Leveling of thin films of colloidal suspensions. *Journal of Colloid and Interface Science*, 343(1):306 – 313, 2010.

[43] Aruna Ramkrishnan and Satish Kumar. Electrohydrodynamic effects in the leveling of coatings. *Chemical Engineering Science*, 101:785 – 799, 2013.

[44] D.T. Wasan, A.D. Nikolov, L.A. Lobo, K. Koczo, and D.A. Edwards. Foams, thin films and surface rheological properties. *Progress in Surface Science*, 39(2):119 – 154, 1992.

[45] Anilkumar G. Gaonkar. *Characterization of food. [electronic resource] : emerging methods.* Amsterdam ; New York : Elsevier, 1995., 1995.

[46] Derek Y. C. Chan, Evert Klaseboer, and Rogerio Manica. Film drainage and coalescence between deformable drops and bubbles. *Soft Matter*, 7:2235–2264, 2011.

[47] Cheng-Yuan Lin and J. C. Slattery. Thinning of a liquid film as a small drop or bubble approaches a fluidfluid interface. *AIChE Journal*, 28(5):786–792, 1982.

[48] Stoyan I. Karakashev and Dilyana S. Ivanova. Thin liquid film drainage: Ionic vs. non-ionic surfactants. *Journal of Colloid and Interface Science*, 343(2):584 – 593, 2010.

[49] Stoyan I. Karakashev and Emil D. Manev. Hydrodynamics of thin liquid films: Retrospective and perspectives. *Advances in Colloid and Interface Science*, 222:398 – 412, 2015. Reinhard Miller, Honorary Issue.

[50] Karl Ziemelis. The future of microelectronics. *Nature*, 406:1021, August 2000.

[51] Stephen Y Chou, Peter R Krauss, and Preston J Renstrom. Imprint of sub-25 nm vias and trenches in polymers. *Applied Physics Letters*, 67(21):3114–3116, 1995.

[52] Stephen Y Chou, Peter R Krauss, and Preston J Renstrom. Nanoimprint lithography. *Journal of Vacuum Science & Technology B*, 14(6):4129–4133, 1996.

[53] Younan Xia, , and George M. Whitesides. Soft lithography. *Annual Review of Materials Science*, 28(1):153–184, 1998.

[54] Ashutosh Sharma and Rajesh Khanna. Pattern formation in unstable thin liquid films. *Physical Review Letters*, 81(16)(10):3463–3466, 1998.

[55] Michael J Fasolka and Anne M Mayes. Block copolymer thin films: Physics and applications. *Annual Review of Materials Research*, 31(1):323–355, 2001.

[56] Rabibrata Mukherjee and Ashutosh Sharma. Instability, self-organization and pattern formation in thin soft films. *Soft matter*, 11(45):8717–8740, 2015.

[57] Nandini Bhandaru, Anuja Das, and Rabibrata Mukherjee. Confinement induced ordering in dewetting of ultra-thin polymer bilayers on nanopatterned substrates. *Nanoscale*, 8(2):1073–1087, 2016.

[58] Aranzazu del Campo, , and Eduard Arzt. Fabrication approaches for generating complex micro- and nanopatterns on polymeric surfaces. *Chemical Reviews*, 108(3):911–945, 2008. PMID: 18298098.

[59] Ning Wu and William B. Russel. Micro- and nano-patterns created via electrohydrodynamic instabilities. *Nano Today*, 4(2):180 – 192, 2009.

[60] E Schaffer, Stephan Harkema, Monique Roerdink, Ralf Blossey, and Ullrich Steiner. Thermomechanical lithography: pattern replication using a temperature gradient driven instability. *Advanced Materials*, 15(6):514–517, 2003.

[61] Mathias Dietzel and Sandra M. Troian. Formation of nanopillar arrays in ultrathin viscous films: The critical role of thermocapillary stresses. *Physical Review Letters*, 103:074501, Aug 2009.

[62] Euan McLeod, Yu Liu, and Sandra M Troian. Experimental verification of the formation mechanism for pillar arrays in nanofilms subject to large thermal gradients. *Physical Review Letters*, 106(17):175501, 2011.

[63] Amgad R. Rezk, Ofer Manor, James R. Friend, and Leslie Y. Yeo. Unique fingering instabilities and soliton-like wave propagation in thin acoustowetting films. *Nature communications*, 3(1167), 2012.

[64] Hong Hu, Hongmiao Tian, Jinyou Shao, Yucheng Ding, Chengbao Jiang, and Hongzhong Liu. Fabrication of bifocal microlens arrays based on controlled electrohydrodynamic reflowing of pre-patterned polymer. *Journal of Micromechanics and Microengineering*, 24(9):095027, 2014.

[65] H. Li, W. Yu, Y. Wang, H. Bu, Z. Liu, Eitan Abraham, and M. P. Y. Desmulliez. Simulation of the electrohydrodynamic instability process used in the fabrication of hierarchic and hollow micro/nanostructures. *RSC Advances*, 4:13774–13781, 2014.

[66] Hong Hu, Hongmiao Tian, Xiangming Li, Jinyou Shao, Yucheng Ding, Hongzhong Liu, and Ningli An. Biomimetic mushroom-shaped microfibers for dry adhesives by electrically induced polymer deformation. *ACS Applied Materials & Interfaces*, 6(16):14167–14173, 2014.

[67] Xiangming Li, Hongmiao Tian, Jinyou Shao, Yucheng Ding, and Hongzhong Liu. Electrically modulated microtransfer molding for fabrication of micropillar arrays with spatially varying heights. *Langmuir*, 29(5):1351–1355, 2013.

[68] N. Wu, L.F. Pease, and W.B. Russel. Toward large-scale alignment of electrohydrodynamic patterning of thin polymer films. *Advanced Functional Materials*, 16(15):1992–1999, 2006.

[69] William Gilbert. *de Magnete*, volume 2, chap. 2. Dover, New York, 1958.

[70] Lord Rayleigh. On the equilibrium of liquid conducting masses charged with electricity. *Philosophical Magazine Series 5*, 14 : 87:184–186, 1882.

[71] Geoffrey Taylor. Studies in electrohydrodynamics. i. the circulation produced in a drop by electrical field. *Proceedings of the Royal Society of London A*, 291:1425:159–166, 1966.

[72] R. S. Allan and S. G. Mason. Particle behaviour in shear and electric fields. i. deformation and burst of fluid drops. *Proceeding of Royal Society of London. Series A*, 267:1328:45–61, 1962.

[73] D.A. Saville. Electrokinetic effects with small particles. *Annual Review of Fluid Mechanics*, 9:321–337, 1977.

[74] W. B. Russel, D. A. Saville, and W. R. Schowalter. *Colloidal Dispersions*. Cambridge University Press, Cambridge, UK, 1989.

[75] H.A. Stone, A.D. Stroock, and A. Ajdari. Engineering flows in small devices. *Annual Review of Fluid Mechanics*, 36(1):381–411, 2004.

[76] Jun Zeng and Tom Korsmeyer. Principles of droplet electrohydrodynamics for lab-on-a-chip. *Lab on a Chip*, 4:265–277, 2004.

[77] Seong-Il Jeong and Jeffrey Didion. Performance characteristics of electrohydrodynamic conduction pump in two-phase loops. *Journal of Thermophysics and Heat Transfer*, 22:1:90–97, 2008.

[78] Stephen Y Chou and Lei Zhuang. Lithographically induced self-assembly of periodic polymer micropillar arrays. *Journal of Vacuum Science & Technology B*, 17(6):3197–3202, 1999.

[79] L. D. Landau and E. M. Lifshitz. *Electrodynamics of continuous media*. Pergamon Press, 1960.

[80] Pola Goldberg-Oppenheimer and Ullrich Steiner. Rapid electrohydrodynamic lithography using low-viscosity polymers. *Small*, 6(11):1248–1254, 2010.

[81] E schaffer, Thomas Thurn-Albrecht, Thomas P Russell, and Ullrich Steiner. Electrohydrodynamic instabilities in polymer films. *EPL (Europhysics Letters)*, 53(4):518, 2001.

[82] Ruhi Verma, Ashutosh Sharma, Kajari Kargupta, and Jaita Bhaumik. Electric field induced instability and pattern formation in thin liquid films. *Langmuir*, 21(8):3710–3721, 2005.

[83] Zhiqun Lin, Tobias Kerle, Thomas P. Russell, Erik Schffer, and Ullrich Steiner. Structure formation at the interface of liquid/liquid bilayer in electric field. *Macromolecules*, 35(10):3971–3976, 2002.

[84] Ning Wu and William B. Russel. Electrohydrodynamic instability of dielectric bilayers: Kinetics and thermodynamics. *Industrial and Engineering Chemistry Research*, 45(16):5455–5465, 2006.

[85] C.W Hirt and B.D Nichols. Volume of fluid (vof) method for the dynamics of free boundaries. *Journal of Computational Physics*, 39(1):201 – 225, 1981.

[86] Francis H. Harlow and J. Eddie Welch. Numerical calculation of time-dependent viscous incompressible flow of fluid with free surface. *Physics of Fluids*, 8:2182–2189, 1965.

[87] Hongmiao Tian, Jinyou Shao, Yucheng Ding, Xiangming Li, and Hongzhong Liu. Numerical characterization of electrohydrodynamic micro- or nanopatterning processes based on a phase-field formulation of liquid dielectrophoresis. *Langmuir*, 29(15):4703–4714, 2013.

[88] Qingzhen Yang, Ben Q. Li, and Yucheng Ding. A numerical study of nanoscale electrohydrodynamic patterning in a liquid film. *Soft Matter*, 9:3412–3423, 2013.

[89] Qingzhen Yang, Ben Q. Li, and Yucheng Ding. Dynamic modelling of micro/nano-patterning transfer by an electric field. *RSC Advances*, 3:24658–24663, 2013.

[90] S H Davis. Thermocapillary instabilities. *Annual Review of Fluid Mechanics*, 19(1):403–435, 1987.

[91] Hongqi Xiang, Yao Lin, and Thomas P. Russell. Electrically induced patterning in block copolymer films. *Macromolecules*, 37(14):5358–5363, 2004.

[92] Samanvaya Srivastava, P. Dinesh Sankar Reddy, Cindy Wang, Dipankar Bandyopadhyay, and Ashutosh Sharma. Electric field induced microstructures in thin films on physicochemically heterogeneous and patterned substrates. *Journal of Chemical Physics*, 132(17):174703, 2010.

[93] Arnab Atta, David G. Crawford, Charles R. Koch, and Subir Bhattacharjee. Influence of electrostatic and chemical heterogeneity on the electric-field-induced destabilization of thin liquid films. *Langmuir*, 27(20):12472–12485, 2011.

[94] Manoj Zope, Kajari Kargupta, and Ashutosh Sharma. Self-organized structures in thin liquid films on chemically heterogeneous substrates: Effect of antagonistic short and long range interactions. *The Journal of Chemical Physics*, 114(16):7211–7221, 2001.

[95] Leonard F. Pease and William B. Russel. Limitations on length scales for electrostatically induced submicrometer pillars and holes. *Langmuir*, 20(3):795–804, 2004. PMID: 15773107.

[96] N. Wu, M. E. Kavousanakis, and W. B. Russel. Coarsening in the electrohydrodynamic patterning of thin polymer films. *Physical Review E*, 81:26306, 2010.

[97] D. A. Saville. Electrohydrodynamics: The taylor-melcher leaky dielectric model. *Annual Review of Fluid Mechanics*, pages 27–64, 1997.

[98] R. V. Craster and O. K. Matar. Electrically induced pattern formation in thin leaky dielectric films. *Physics of Fluids (1994-present)*, 17(3):1131–1198, 2005.

[99] P. Gambhire and R. M. Thaokar. Role of conductivity in the electrohydrodynamic patterning of air-liquid interfaces. *Physical Review E*, 86:036301, Sep 2012.

[100] Kartick Mondal, Prashant Kumar, and Dipankar Bandyopadhyay. Electric field induced instabilities of thin leaky bilayers: Pathways to unique morphologies and miniaturization. *Journal of Chemical Physics*, 138(2):024705, 2013.

[101] Michael D. Dickey, Suresh Gupta, K. Amanda Leach, Elizabeth Collister, C. Grant Willson, and Thomas P. Russell. Novel 3-d structures in polymer films by coupling external and internal fields. *Langmuir*, 22(9):4315–4318, 2006.

[102] M. D. Morariu, N. E. Voicu, E. Schaffer, Z. Lin, T. P. Russell, and U. Steiner. Hierarchical structure formation and pattern replication induced by an electric field. *Nature Materials*, 2:48 – 52, 2003.

[103] Dipankar Bandyopadhyay, Ashutosh Sharma, Uwe Thiele, and P. Dinesh Sankar Reddy. Electric-field-induced interfacial instabilities and

morphologies of thin viscous and elastic bilayers. *Langmuir*, 25(16):9108–9118, 2009.

[104] V. Shankar and Ashutosh Sharma. Instability of the interface between thin fluid films subjected to electric fields. *Journal of Colloid and Interface Science*, 274(1):294 – 308, 2004.

[105] G. I. Taylor. Disintegration of water drops in an electric field. *Proceedings of the Royal Society of London A*, 280(1382):383–397, 1964.

[106] John Zeleny. Instability of electrified liquid surfaces. *Physical Review*, 10:1–6, 1917.

[107] Michael T. Harris Robert T. Collins, Jeremy J. Jones and Osman A. Basaran. Electrohydrodynamic tip streaming and emission of charged drops from liquid cones. *Nature Physics*, 4:149–154, 2008.

[108] Graeme Supeene, Charles R. Koch, and Subir Bhattacharjee. Deformation of a droplet in an electric field: Nonlinear transient response in perfect and leaky dielectric media. *Journal of Colloid and Interface Science*, 318(2):463–476, 2008.

[109] Chin Kai Meng Shek Fu Wong John B. Fenn, Matthias Mann and Carig M. Whitehouse. Electrospray ionization for mass spectrometry of large biomolecules. *Science*, 246(4926):64–71, 1989.

[110] Wang, Yunshan, Tan, Ming K., Go, David B., and Chang, Hsueh-Chia. Electrospray cone-jet breakup and droplet production for electrolyte solutions. *european physics letters*, 99(6):64003, 2012.

[111] Hong Hu, Hongmiao Tian, Jinyou Shao, Yucheng Ding, Chengbao Jiang, and Hongzhong Liu. Fabrication of bifocal microlens arrays based on controlled electrohydrodynamic reflowing of pre-patterned polymer. *Journal of Micromechanics and Microengineering*, 24(9):095027, 2014.

[112] Qingzhen Yang, Ben Q. Li, Yucheng Ding, and Jinyou Shao. Steady state of electrohydrodynamic patterning of micro/nanostructures on thin polymer films. *Industrial & Engineering Chemistry Research*, 53(32):12720–12728, 2014.

[113] Hiroyuki Ohno. Design of ion conductive polymers based on ionic liquids. *Macromolecular Symposia*, 249-250(1):551–556, 2007.

[114] Saptarshi Majumdar, Kajari Kargupta, and Saibal Ganguly. Mathematical modeling for the ionic inclusion process inside conducting polymer-based thin-films. *Polymer Engineering & Science*, 48(11):2229–2237, 2008.

[115] Matthew A. Gebbie, Markus Valtiner, Xavier Banquy, Eric T. Fox, Wesley A. Henderson, and Jacob N. Israelachvili. Ionic liquids behave as dilute electrolyte solutions. *Proceedings of the National Academy of Sciences*, 110(24):9674–9679, 2013.

[116] Priya Gambhire and Rochish Thaokar. Electrokinetic model for electric-field-induced interfacial instabilities. *Physical Review E*, 89:032409, Mar 2014.

[117] Emilij k. Zholkovskij, Jacob H. Masliyah, and Jan Czarnecki. An electrokinetic model of drop deformation in an electric field. *Journal of Fluid Mechanics*, 472:1–27, 12 2002.

[118] Emilij K. Zholkovskij, Jacob H. Masliyah, Vladimir N. Shilov, and Subir Bhattacharjee. Electrokinetic phenomena in concentrated disperse systems: General problem formulation and spherical cell approach. *Advances in Colloid and Interface Science*, 134135(0):279 – 321, 2007. Surface forces: wetting phenomena, membrane separation, rheology. Topical issue in honour of Victor Starov.

[119] Henri Bnard. tude exprimentale des courants de convection dans une nappe liquide. - rgime permanent : tourbillons cellulaires. *Journal of Physical Theory and Application*, 9(1):513–524, 1900.

[120] Tatiana Gambaryan-Roisman. Modulation of marangoni convection in liquid films. *Advances in Colloid and Interface Science*, 222:319 – 331, 2015. Reinhard Miller, Honorary Issue.

[121] Iman Nejati, Mathias Dietzel, and Steffen Hardt. Conjugated liquid layers driven by the short-wavelength bnardmarangoni instability: experiment and numerical simulation. *Journal of Fluid Mechanics*, 783:46–71, 11 2015.

[122] J. P. Burelbach, S. G. Bankoff, and S. H. Davis. Nonlinear stability of evaporating/condensing liquid films. *Journal of Fluid Mechanics*, 195:463–494, 10 1988.

[123] Alexander Oron and Philip Rosenau. On a nonlinear thermocapillary effect in thin liquid layers. *Journal of Fluid Mechanics*, 273:361–374, 8 1994.

[124] Alexander Oron. Nonlinear dynamics of three-dimensional long-wave marangoni instability in thin liquid films. *Physics of Fluids*, 12(7):1633–1645, 2000.

[125] Michael F Schatz and G Paul Neitzel. Experiments on thermocapillary instabilities. *Annual Review of Fluid Mechanics*, 33(1):93–127, 2001.

[126] A. E. Samoilova and N. I. Lobov. On the oscillatory marangoni instability in a thin film heated from below. *Physics of Fluids*, 26(6):064101, 2014.

[127] Andrew Corbett and Satish Kumar. Combined thermal and electrohydrodynamic patterning of thin liquid films. *Journal of Engineering Mathematics*, 94(1):81–96, 2015.

[128] R. W. Atherton and G. M. Homsy. On the derivation of evolution equations for interfacial waves. *Chemical Engineering Communications*, 2(2):57–77, 1976.

[129] Martin Z. Bazant, Brian D. Storey, and Alexei A. Kornyshev. Double layer in ionic liquids: Overscreening versus crowding. *Physical Review Letters*, 106:046102, Jan 2011.

[130] D. W. Lee, D. J. Im, and I. S. Kang. Electric double layer at the interface of ionic liquid-dielectric liquid under electric field. *Langmuir*, 29(6):1875–1884, 2013.

[131] E. J. W. Verwey and J. TH. G. Overbeek. *Theory and Stability of Lyophobic Colloids*. Elsevier, Amesterdam, 1948.

[132] M. Polat and H. Polat. Analytical solution of poissonboltzmann equation for interacting plates of arbitrary potentials and same sign. *Journal of Colloid and Interface Science*, 341(1):178 – 185, 2010.

[133] Kathryn E. Brenan and Linds R. Petzold. The numerical solution of higher index differential/algebraic equations by implicit methods. *SIAM Journal on Numerical Analysis*, 26(4):976–996, 1989.

[134] David G. Crawford. Numerical simulation of thin liquid film drainage under the influence of pressure and electrical forcing. Master's thesis, University of Alberta, 2008.

[135] Linda R Petzold. A description of dassl: A differential/algebraic system solver. *Proc. IMACS World Congress*, pages 430–432, 1982.

[136] W. H. Vandevender and K. H. Haskell. The slatec mathematical subroutine library. *signum newsletter*, 17(3):16–21, September 1982.

[137] K. E. Brenan, S. L. Campbell, and L. R. Petzold. *2. Theory of DAE's*, chapter 2, pages 15–39. 1996.

[138] R. S. Maier, L. R. Petzold, and W. Rath. Using daspk on the tmc cm5. experiences with two programming models. In *Scalable Parallel Libraries Conference, 1993., Proceedings of the*, pages 174–182, Oct 1993.

[139] C.W. Gear. The simultaneous numerical solution of differential- algebraic equations. *IEEE Transactions on Circuit Theory*, 18(1):89–95, 1971.

[140] Roy Leonard Brown and C. William Gear. Documentation for dfasub–a program for the solution of simultaneous implicit differential and nonlinear equations, by r. l. brown [and] c. w. gear. Technical report, Dept. of Computer Science, University of Illinois at Urbana-Champaign, 1973.

[141] Alan C. Hindmarsh. Ode solvers fr use with the method of lines. *Advances in Computer Methods for Partial Differential Equations*, pages 312–316, 1981.

[142] Leonardo Espin, Andrew Corbett, and Satish Kumar. Electrohydrodynamic instabilities in thin viscoelastic films - ac and dc fields. *Journal of Non-Newtonian Fluid Mechanics*, 196(0):102–111, 2013.

[143] Hongmiao Tian, Chunhui Wang, Jinyou Shao, Yucheng Ding, and Xiangming Li. Electrohydrodynamic pressure enhanced by free space charge for electrically induced structure formation with high aspect ratio. *Langmuir*, 30(42):12654–12663, 2014. PMID: 25268463.

[144] Ruhi Verma, Ashutosh Sharma, Indrani Banerjee, and Kajari Kargupta. Spinodal instability and pattern formation in thin liquid films confined between two plates. *Journal of Colloid and Interface Science*, 296(1):220 – 232, 2006.

[145] Nicoleta E. Voicu, Stephan Harkema, and Ullrich Steiner. Electric-field-induced pattern morphologies in thin liquid films. *Advanced Functional Materials*, 16(2):926–934, 2006.

[146] Dongchoul Kim and Wei Lu. Three-dimensional model of electrostatically induced pattern formation in thin polymer films. *physical Review E*, 73(10):35206, 2006.

[147] Joonwon Bae, Elizabeth Glogowski, Suresh Gupta, Wei Chen, Todd Emrick, and Thomas P. Russell. Effect of nanoparticles on the electrohydrodynamic instabilities of polymer/nanoparticle thin films. *Macromolecules*, 41(7):2722–2726, 2008.

[148] P. Dinesh Sankar Reddy, Dipankar Bandyopadhyay, and Ashutosh Sharma. Self-organized ordered arrays of core-shell columns in viscous bilayers formed by spatially varying electric fields. *Journal of Physical Chemistry C*, 114(49):21020–21028, 2010.

[149] David Salac, Lu Wei, Wang Chia-Wei, and Ann Marie Sastry. Pattern formation in a polymer thin film induced by an in-plane electric field. *Applied Physics Letters*, 85(7):1161 – 1163, 2004.

[150] Scott A. Roberts and Satish Kumar. Ac electrohydrodynamic instabilities in thin liquid films. *Journal of Fluid Mechanics*, 631:255–279, 7 2009.

[151] Scott A. Roberts and Satish Kumar. Electrohydrodynamic instabilities in thin liquid trilayer films. *Physics of Fluids*, 22(12):122102, 2010.

[152] Hadi Nazaripoor, Charles R. Koch, and Mohtada Sadrzadeh. Electrostatic model for electric-field-induced instabilities of thin ionic liquid films. In *Proceeding of 64th Canadian Society of Chemical Engineering Conference*, October 2014.

[153] Hadi Nazaripoor, Behnam Khorshid, Charles R. Koch, and Mohtada Sadrzadeh. Interface morphology of thin films: electrohydrodynamic vs

electrokinetic model. In *24th International Congress of Theoretical and Applied Mechanics (ICTAM)*, August 2016.

Appendix

A-1 Differential algebraic solver-DASSL

Subroutine DASSL solves a system of differential algebraic equations which have the form of $F(t, y, y^{'}) = 0$. This solver has been written by Dr. Linda R. Petzold at Computing and Mathematics Research Division in Lawrence Livermore National Laboratory, CA. USA [135]. This subroutine uses the backward differentiation formula (BDF) to approximate the derivative (here for time) and it employs the predictor-corrector method [140] combined with Newton's method to solve the system. On every step, the value for time step and the order of BDF may vary from one to five depending the behavior of solution.

Note: In this work the DASSL is called in a time loop which could have it is own time step (called user time step). DASSL itself uses adaptive time steps to get the results for the time span provided by user.

The DASSL is routine is generally defined as:

$$SUBROUTINE\ DDASSL(RES, NEQ, T, Y, YPRIME, TOUT, INFO, RTOL, ATOL, IDID, RWORK, LRW, IWORK, LIW, RPAR, IPAR, JAC)$$

In order to use DASSL solver following information should be provided by user:

- RES; is an external subroutine which contains the DAE system and in our study all the FD descritized equations and the boundary condition are defined in RES.
- NEQ; is the total number of equations should be solved. In this study it is equal to $N_x \times N_y$
- T; is the current value of the independent variable, here is time T
- Y; is the array of size NEQ which contains the current value of the dependent variable, here is interface height, H. At initial stage this array is given by user, but at later stages (next time steps) it can be a solution of DASSL for the previous step.
- YPRIME; is the array of size NEQ which contains the derivatives of the dependent variable, here is interface height, H. At initial stage this array

is given by user, but at later stages (next time steps) it can be a solution of DASSL for the previous step.

- TOUT; is the point which user desired to get the solution of Y, here it is the time which user defined as an input
- INFO; is an integer array with size of 15 or larger which is defined in DASSL that user could communicate with solver regarding the options available for solving the DAE such as initialization, accuracy and etc. (See [136] for details.)
- RTOL and ATOL; are the relative and absolute error tolerances, respectively. They are defined to specify the solution accuracy.
- IDID; is the parameter which DASSL use to identify the warnings and errors caused.
- RWORK and IWORK; are working arrays and contain information about the solution procedure such as RWORK(7) provides the last successful stepsize used in solver, IWORK(8) provides the order of k^{th} used on the last step and etc. (See [136] for details.)
- LIW and LRW; are specified inputs that should be set up based on the DAASL manuals. (See [136] for details.)
- RPAR and IPAR; are real and integer parameter arrays respectively which can be used for communication between your main program and the external subroutines of RES and JAC.
- JAC; if the user does not provide a matrix of partial derivatives of the system to evaluate it analytically in DASSL (info(5)=1), DASSL evaluates them automatically by using numerical differences and JAC should be provided by user.

B-1 Effect of viscose and van der Waals forces on drainage time

The stabilizing effects of lower layer viscosity and interfacial tension and the destabilizing effect of the Hamaker constant are investigated. Film drainage is presented to track the dewetting of liquid-liquid bilayer in response to short range van der Waals forces. These simulations are done for an initially unstable film under no external electric disturbance. Next, for an applied electric field, the effects of variations in the electric permittivity ratio of bilayers (ϵ_r) on the pattern formation, as well as the feature shape and size are studied. Finally the effect of using a bounding fluid which is IC instead of being PD is tested to understand it's effects on the dynamics and pattern formation process. These results will be discussed in this section.

Nondimensional minimum film thickness variations versus time by changing (a) interfacial tension and (b) film viscosity is shown in Fig. B-1. The lowest value for the interface height is the equilibrium distance defined for the Born repulsive force on the lower electrode. This is used to avoid a contact line singularity and is shown with dotted line in $h_{min}/d = 0.01$. The time when the interface reaches the Born equilibrium height is defined as the drainage time and it gives an indication as to how fast instabilities are growing over the domain. In Fig. B-1a surface tension is varied at $\mu = 1(Pa.s)$ while in Fig. B-1b viscosity is varied at $\gamma = 0.02(N/m)$. Drainage time increases by several orders of magnitude for both increasing surface tension and viscosity. Presenting the results in dimensional time assists in better understanding of these considerable effects in the real time experiments. The use of low viscosity polymers degrade damping of fluctuations and leads to fast dewetting and pattern formations in films which is of interest in fast EHD patterning.

Attractive van der Waals forces (effective Hamaker constant greater than zero) tend to enhance fluctuation growth. Systems with higher effective Hamaker constant are more unstable and film rupture occurs sooner in these systems as shown in Fig. B-2. The film drainage time is more sensitive to Hamaker constant when no electrostatic force ($\psi_{up} = 0$) is applied. This is illustrated by the $\psi_{up} = 0$ lines in Fig. B-2. By applying electric field, electrostatic stress forms on the interface due to inequality of electric permittivity ratio of layers ($\varepsilon_r = 2.5$) and this force is considered as a long range and dominant force compared with van der Waals forces. Drainage time significantly decreases when applying a voltage but still depends on the Hamaker constant value. However the drainage time is not sensitive to the Hamaker constant in presence of electrostatic force.

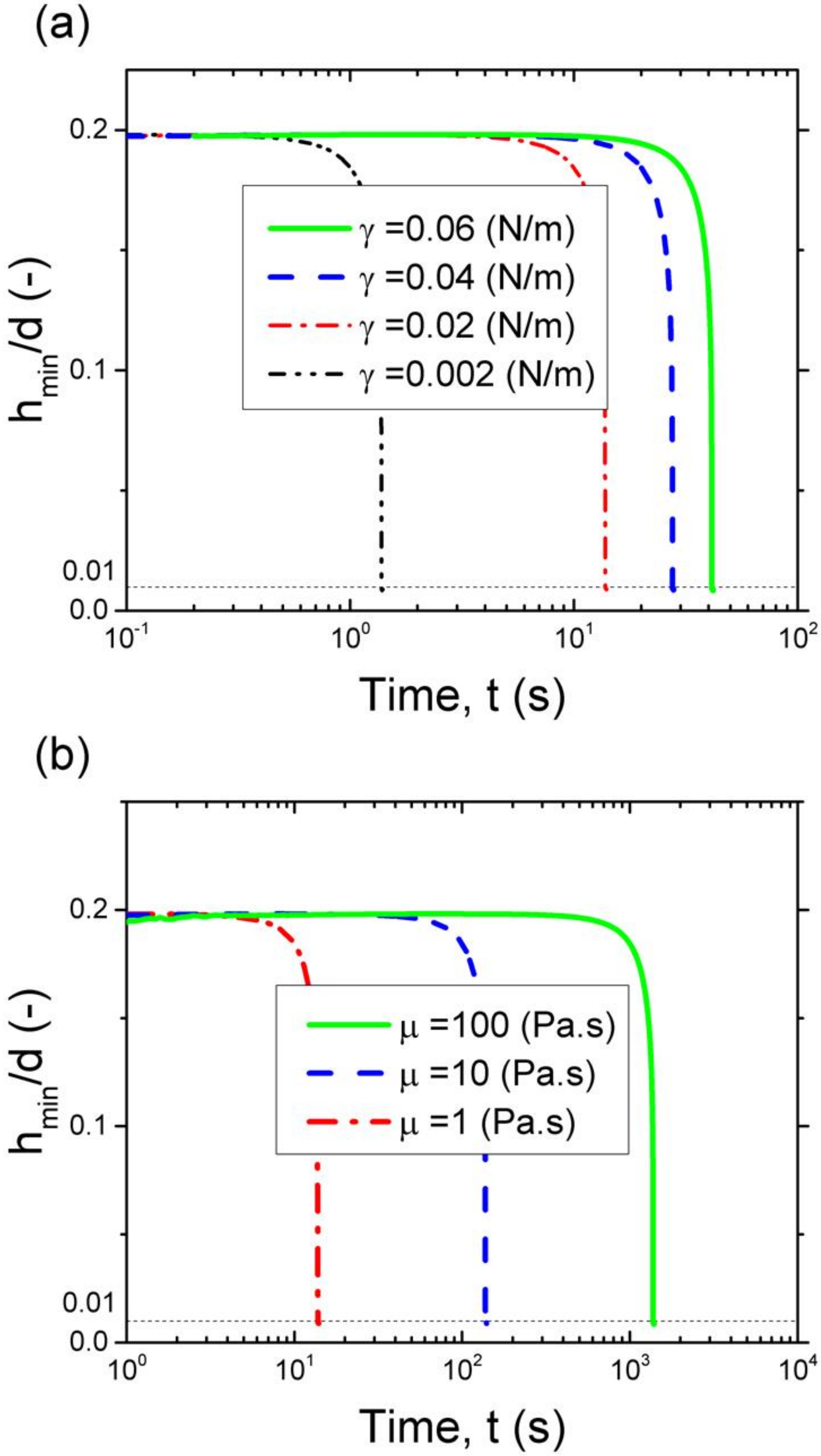

Figure B-1: Nondimensional minimum film thickness variations on an initially unstable bilayer under no applied electric field versus time for: (a) interfacial tension, γ and (b) viscosity, μ. $A = 10^{-19}(J)$

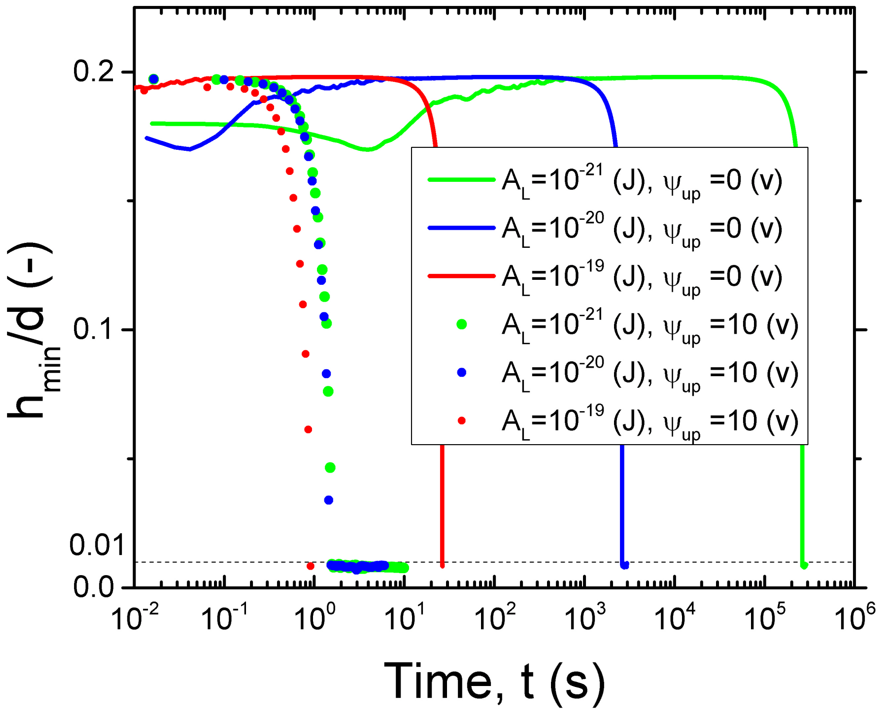

Figure B-2: Nondimensional minimum film thickness variations on an initially unstable bilayer versus time: Effects of hamaker constant, A, and applied voltage, V_{up}.

C-1 Copyrights and permissions

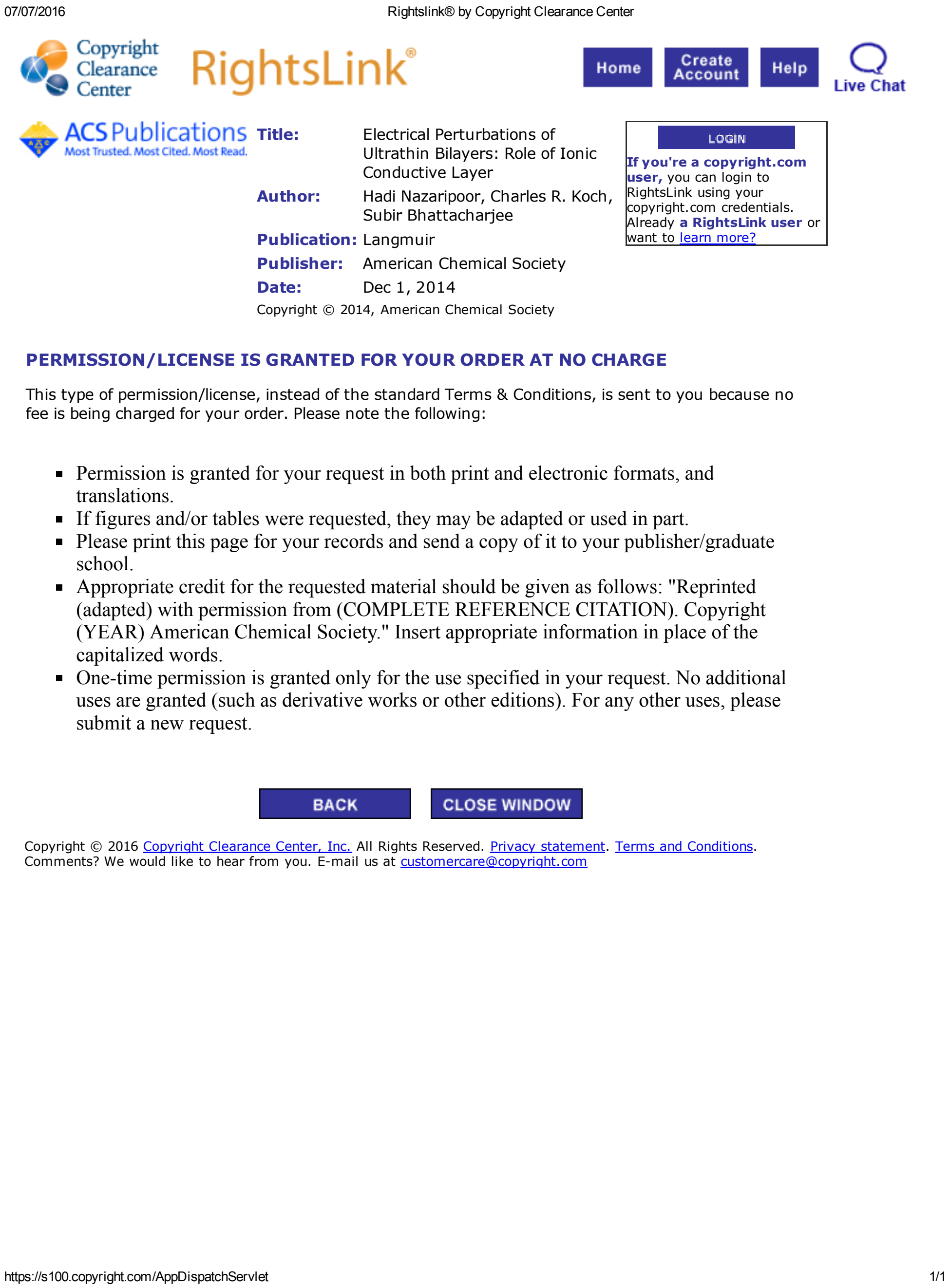

07/07/2016 Rightslink® by Copyright Clearance Center

Title:	Electrical Perturbations of Ultrathin Bilayers: Role of Ionic Conductive Layer
Author:	Hadi Nazaripoor, Charles R. Koch, Subir Bhattacharjee
Publication:	Langmuir
Publisher:	American Chemical Society
Date:	Dec 1, 2014

Copyright © 2014, American Chemical Society

If you're a copyright.com user, you can login to RightsLink using your copyright.com credentials. Already **a RightsLink user** or want to learn more?

PERMISSION/LICENSE IS GRANTED FOR YOUR ORDER AT NO CHARGE

This type of permission/license, instead of the standard Terms & Conditions, is sent to you because no fee is being charged for your order. Please note the following:

- Permission is granted for your request in both print and electronic formats, and translations.
- If figures and/or tables were requested, they may be adapted or used in part.
- Please print this page for your records and send a copy of it to your publisher/graduate school.
- Appropriate credit for the requested material should be given as follows: "Reprinted (adapted) with permission from (COMPLETE REFERENCE CITATION). Copyright (YEAR) American Chemical Society." Insert appropriate information in place of the capitalized words.
- One-time permission is granted only for the use specified in your request. No additional uses are granted (such as derivative works or other editions). For any other uses, please submit a new request.

Copyright © 2016 Copyright Clearance Center, Inc. All Rights Reserved. Privacy statement. Terms and Conditions.
Comments? We would like to hear from you. E-mail us at customercare@copyright.com

https://s100.copyright.com/AppDispatchServlet 1/1

Figure C-3: Copyrights (2014) American Chemical Society permission for Ref.[2]

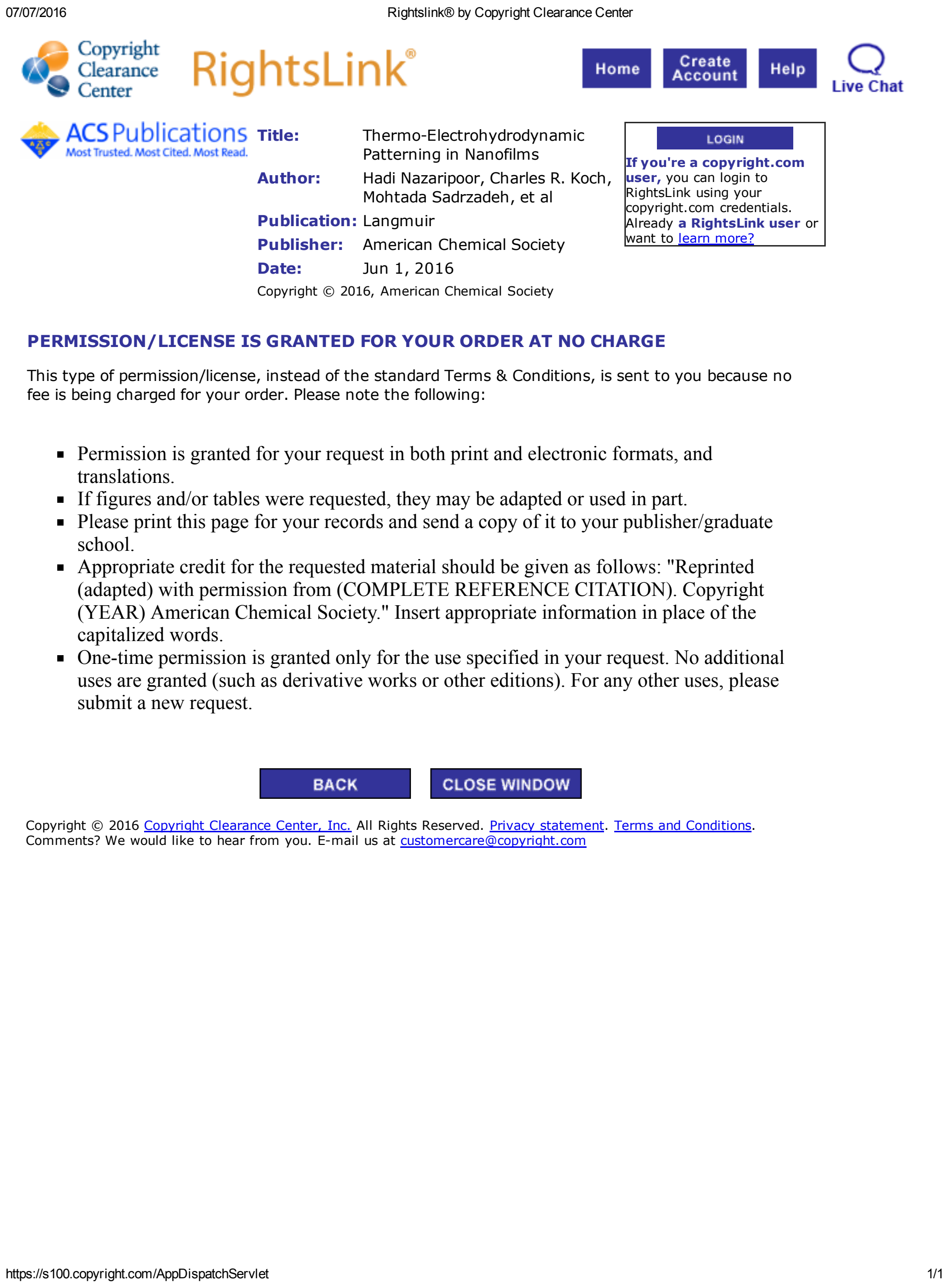

07/07/2016 Rightslink® by Copyright Clearance Center

Title:	Thermo-Electrohydrodynamic Patterning in Nanofilms
Author:	Hadi Nazaripoor, Charles R. Koch, Mohtada Sadrzadeh, et al
Publication:	Langmuir
Publisher:	American Chemical Society
Date:	Jun 1, 2016

Copyright © 2016, American Chemical Society

If you're a copyright.com user, you can login to RightsLink using your copyright.com credentials. Already **a RightsLink user** or want to learn more?

PERMISSION/LICENSE IS GRANTED FOR YOUR ORDER AT NO CHARGE

This type of permission/license, instead of the standard Terms & Conditions, is sent to you because no fee is being charged for your order. Please note the following:

- Permission is granted for your request in both print and electronic formats, and translations.
- If figures and/or tables were requested, they may be adapted or used in part.
- Please print this page for your records and send a copy of it to your publisher/graduate school.
- Appropriate credit for the requested material should be given as follows: "Reprinted (adapted) with permission from (COMPLETE REFERENCE CITATION). Copyright (YEAR) American Chemical Society." Insert appropriate information in place of the capitalized words.
- One-time permission is granted only for the use specified in your request. No additional uses are granted (such as derivative works or other editions). For any other uses, please submit a new request.

Copyright © 2016 Copyright Clearance Center, Inc. All Rights Reserved. Privacy statement. Terms and Conditions.
Comments? We would like to hear from you. E-mail us at customercare@copyright.com

https://s100.copyright.com/AppDispatchServlet 1/1

Figure C-4: Copyrights (2014) American Chemical Society permission for Ref. [5]